GEOPHYSICAL CHARACTERIZATION & MACHINE LEARNING-BASED QUANTITATIVE INTERPRETATION OF LOWER-GORU FORMATION OF KADANWARI BLOCK, MIDDLE INDUS BASIN PAKISTAN

AMBER LATIF

01-262212-012

Department of Earth and Environmental Sciences

Bahria University, Islamabad

2023

GEOPHYSICAL CHARACTERIZATION & MACHINE LEARNING-BASED QUANTITATIVE INTERPRETATION OF LOWER-GORU FORMATION OF KADANWARI BLOCK, MIDDLE INDUS BASIN PAKISTAN

AMBER LATIF

01-262212-012

A thesis submitted in Fulfilment of the Requirements for the award

of the degree of Master's in Science (Geophysics)

Department of Earth and Environmental Sciences

Bahria University, Islamabad

2023

APPROVAL FOR EXAMINATION

Scholar's Name: AMBER LATIF

Registration No. 75590

Programme of Study: MS GEOPHYSICS

Thesis Title: Geophysical Characterization & Machine Learning-Based Quantitative Interpretation of Lower-Guru Formation of Kadanwari Block, Middle Indus Basin Pakistan

It is to certify that the above scholar's thesis has been completed to my satisfaction and, to my belief, its standard is appropriate for submission for examination. I have also conducted a plagiarism test of this thesis using HEC prescribed software and found similarity index **6%** that is within the permissible limit set by the HEC for the MS degree thesis. I have also found the thesis in a format recognized by the BU for the MS thesis.

Principal Supervisor's Signature: _____

Date: _____

Name: _____

AUTHOR'S DECLARATION

I, **"Amber Latif"** hereby state that my MS thesis titled **"Geophysical Characterization & Machine Learning-Based Quantitative Interpretation of Lower-Goru Formation of Kadanwari Block, Middle Indus Basin Pakistan"** is my own work and has not been submitted previously by me for taking any degree from this university **Bahria University Islamabad** or anywhere else in the country/world.

At any time if my statement is found to be incorrect even after my graduation, the University has the right to withdraw/cancel my MS degree.

Name of scholar: Amber Latif

Date: 24- September - 2023

.

PLAGIARISM UNDERTAKING

I solemnly declare that the research work presented in the thesis titled **"**titled **"Geophysical Characterization & Machine Learning-Based Quantitative Interpretation of Lower-Goru Formation of Kadanwari Block, Middle Indus Basin Pakistan"** is solely my research work with no significant contribution from any other person. Small contribution/help wherever taken has been duly acknowledged and that complete thesis has been written by me.

I understand the zero-tolerance policy of the HEC and Bahria University towards plagiarism. Therefore, I as an Author of the above titled thesis declare that no portion of my thesis has been plagiarized and any material used as reference is properly referred to / cited.

I undertake that if I am found guilty of any formal plagiarism in the above-titled thesis even after the award of the MS degree, the university reserves the right to withdraw/revoke my MS degree and that HEC and the University have the right to publish my name on the HEC / University website on which names of scholars are placed who submitted plagiarized thesis.

Scholar / Author's Sign: _____

Name of the Scholar: Amber Latif

DEDICATION

With profound appreciation, I dedicate this research to my parents and teachers, whose belief in my potential has been unwavering. Your encouragement has been the wind beneath my wings, propelling me towards academic success. Your support and guidance have been my compass, leading me towards this milestone. I am forever thankful for your belief in me.

ACKNOWLEGEMENTS

All praise and reverence belong to Allah, the Almighty (S.W.T.), and I humbly submit before His divine presence. He is the sole bestower of wisdom and knowledge. I deeply thank Allah SWT, the Supreme Creator, for His blessings and guidance in completing this thesis. Through His grace, I found the patience and determination to write it. My blessings and salutations go to the Holy Prophet Muhammad (S.A.W.W), who illuminated our path from ignorance to enlightenment.

I extend my sincere appreciation to my supervisor, Dr. Muhsan Ehsan, and my Co-supervisor, Dr. Khalid Amin Khan, for their invaluable guidance, unwavering support, and profound wisdom during this research endeavour. Their dedication to my academic growth and their commitment to nurturing my research skills have been instrumental in shaping this work. I consider myself fortunate to have had them as my mentors, and their expertise has left an indelible mark on my educational journey. Their encouragement, constructive feedback, and mentorship have played a pivotal role in the successful completion of this research.

I would like to extend my heartfelt gratitude to Dr. Said Akbar Khan, the Head of the Department of Earth and Environmental Sciences at Bahria University, Islamabad, for his invaluable support and guidance. I also wish to express my appreciation to my teachers, fellow researchers, and friends who have been a tremendous source of encouragement, assistance, and motivation throughout my research journey. Lastly, I am deeply thankful to my parents for their unwavering belief in me and constant inspiration.

ABSTRACT

Seismic reflection is a key geophysical method for hydrocarbon prospecting, mapping geological features, primarily focusing on assessing reservoirs and their physical properties. Research was conducted on the Kadanwari Gas Field, situated in the Middle Indus Basin, characterized by an extensional regime dominated by horst and graben structures. The study involves a comprehensive approach, beginning with a 3D seismic structural interpretation aimed at mapping the designated block's geological structure and reservoir quality. Subsequently, a petrophysical interpretation is executed to pinpoint zones of interest within the target formations, specifically focusing on the G, F, and E sand intervals within the Lower Goru Formation. A model-based post-stack inversion algorithm was utilized to characterize the reservoir, and various attributes such as instantaneous phase, trace envelope, and spectral decomposition were applied to identify thin beds. Shear sonic velocity (Vs) is determined using both the Castagna equation and machine learning. Upon comparison and validation using synthetic AVA gathers, it was evident that the machine learning-driven multi-regression approach significantly improved the predictive accuracy of shear sonic velocity (Vs), yielding results that are 80% to 90% superior to an alternative method. Additionally, machine learning was employed to perform facies modeling aimed at categorizing the challenging-to-distinguish thin sand and shale layers within the Lower Goru Formation into three distinct groups: sand, shale, and shaly sand. Finally, the research focused on computing geomechanical parameters, with a particular emphasis on automating the pre-conditioning of petrophysical logs using machine learning. This automation greatly facilitated the automatic detection of layer boundaries of sand and shale of Lower Goru Formation. The comprehensive geophysical analysis of the Kadanwari area, empowered by advanced methodologies and machine learning, revealed the G and E sands of the Lower Goru Formation as promising reservoirs with significant hydrocarbon potential. Incorporating machine learning techniques, the study successfully deduced essential geomechanical parameters.

TABLE OF CONTENT

LIST OF TABLES

LIST OF FIGURES

CHAPTER 1

INTRODUCTION

1.1 General Introduction

Geophysical interpreters construct simplified representations of what lies beneath the Earth's surface to better understand its geological characteristics. Various geophysical techniques are employed for subsurface investigations, each serving specific needs. However, seismic methods are adaptable and widely applied in fields such as engineering, mining, groundwater and salt dome exploration, environmental assessments, and most notably, the search for hydrocarbons (Kearey, 2002). Seismic reflection techniques have historically been a primary tool for identifying possible oil and gas deposits and gathering data regarding reservoir rocks' physical properties. Variations in rock properties, like density, can alter the seismic acoustic impedance. This shift has a noticeable impact that can be discerned in high-resolution seismic data. The estimation of the petrophysical properties of the reservoir is a crucial parameter in borehole interpretation (Kadri, 1995).

3D seismic is a geophysical technique employed to analyze subsurface geology and serves as a valuable resource for pinpointing potential drilling locations. These surveys, often conducted on densely sampled grids, yield high-resolution 3D images that unveil intricate geological structures, particularly useful in complex exploration scenarios. The recording of 3D seismic data enables us to discern variations in the reservoir environment, such as fluid saturation and pore pressure (Yilmaz, 2001). Additionally, it aids in mapping reflections and faults, contributing to the interpretation of geological features and hydrocarbon potential (Badely, 1985).

Seismic inversion techniques are employed to create models that describe the characteristics of underground rocks and fluids, utilizing data from seismic surveys and well logs. Its primary objective is to transform the entire seismic dataset into various quantitative rock properties, typically focusing on impedance values (Barclay, 2008).

Seismic attributes play a crucial role in offering qualitative insights for understanding both structural and stratigraphic features, such as channels, meanders, pinch-outs, thin bed turning, etc (Barens, 2001).

Geomechanics is the field that explores how subsurface rock formations deform or undergo structural changes in response to changes in stress, pressure, and temperature. It has gained increasing significance in the oil and gas exploration industry (Busetti, 2019).

With the advancements in computer science algorithms, machine learning (ML) has emerged as a recent and powerful tool in the field of geosciences. It possesses the capability to unveil relationships within provided data, facilitating the prediction of desired outcomes (Gupta et al., 2021). In recent times, machine learning (ML) has advanced as a robust and highly efficient approach for accurately predicting shear sonic logs (DTS) while minimizing the need for extensive input datasets (Ahmed et al., 2022).

1.2 Introduction to Study Area

The study area encompasses a portion of the Kadanwari Gas Field situated in the Khairpur district of Sindh, within the Middle Indus Basin of Pakistan (Figure 1.1). Kadanwari is a productive conventional gas field situated onshore in Pakistan, and it is operated by Eni Pakistan. The Kadanwari Gas Field is located near the Thar Desert, to the southeast of Sukkur, approximately 75 kilometres away, situated within the Middle Indus Basin of Pakistan. The coordinates for the study area are between approximately 27°30'10" N latitude to 27°10'00" N latitude and 69°28'20" E longitude to 69°19'00" E longitude (Ahmed et al., 2007).

Kadanwari mainly consists of a series of small structural traps, specifically fault-bounded horst blocks. The presence of numerous gas-producing wells in the study area confirms it as a gas-prone region. The producing reservoirs in the Kadanwari Gas Field are the Lower Goru sands, which are of Cretaceous age. Topographically, the study area comprises sand dunes and is situated in a region with low rainfall. In terms of climate, the

area falls within a region that experiences extremely hot summers and very cold winters. The overall temperature range in this area varies between 46°C and 20°C.

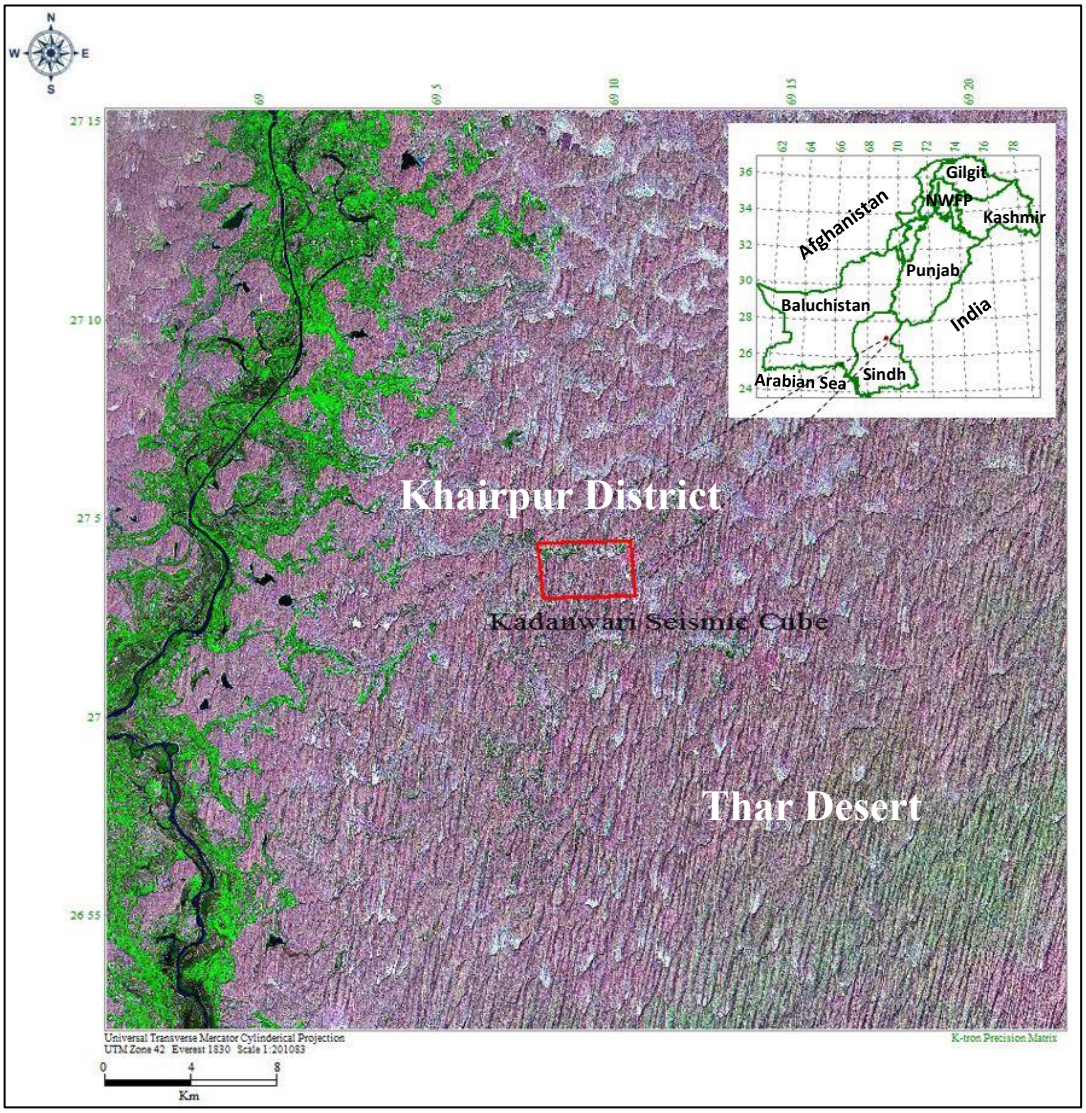

Figure 1.1 Geographical Location of Kadanwari cube

1.3 Exploration History of Kadanwari Gas field

The Kadanwari Gas Field, which is currently in production, was initially explored in 1989 and commenced production in May 1995 (Ahmed et al. 2007). In September 1989, the Kadanwari-01 well was drilled, and it encountered dry gas in the sandstone of

the Lower Goru Formation, which belongs to the Lower Cretaceous age, at a depth of around 3,325 meters. The well yielded a gas rate of 29.6 million standard cubic feet per day (MMscfd). Two additional wells, Gorwar 01 and K 03, were drilled to delineate the extent of the reservoir pool. The Kadanwari-03 well was successful in producing gas at rates ranging from 29 to 38 million standard cubic feet per day (MMscfd). However, Gorwar 01 initially produced gas along with a percentage of water, but over time, the amount of water increased rapidly, leading to the abandonment of the well. The reservoir within this gas field exhibits characteristics of a shoreline-estuarine system that endured the influence of longshore currents and tidal effects for an extended period (Ahmad & Chaudhry, 2002).

The reservoir in the Kadanwari Gas field is situated within the Lower Goru Formation sandstone, with a shaly sequence from the Upper Goru Formation acting as a sealing layer above it. All significant gas findings in the Middle Indus Basin come from the Lower Goru sands. As a result, various companies have extensively studied these sands. Every company has established its own classification for the sand packages within the Lower Goru Formation. ENI company categorized the Lower Goru sands into divisions ranging from A to H. To date, a total of 15 wells have been drilled in the Kadanwari Gas field , targeting various sand layers within the Lower Goru Formation. The majority of these wells have been primarily productive in the E and G sand divisions of the Lower Goru Formation. Currently, only six of these 15 wells remain in active production (Ahmad & Chaudhry, 2002).

1.4 Literature review

In the study by Ali et al. (2023), unsupervised machine learning and cluster analysis were used to categorize reservoir quality at the Kadanwari gas field in SE Pakistan. Using well-log data from four wells, the self-organizing map (SOM) was employed to identify three main lithofacies: sandstone, shaly sand, and shale. Additional techniques like sonic-neutron and M-N cross plots helped pinpoint the sandstone matrix, and cluster analysis grouped the reservoirs into four quality categories, rating sandstone as excellent and shale as poor (Ali et al., 2023).

The 2022 research article by Ahmed et al. focuses on predicting shear sonic log (DTS) and various petrophysical and elastic attributes in the Kadanwari Gas Field in Pakistan. Utilizing wireline logs and well tops from four wells, the study employs rock physics modeling and supervised machine learning algorithms—specifically Random Forest (RF), Decision Tree Regression (DTR), and Support Vector Regression (SVR)—to fill in missing DTS log curves. Among the tested algorithms, Random Forest was found to be the most accurate for this application (Ahmed et al., 2022).

Another research conducted by Austin et al. in 2018, a model-based inversion technique was applied to a field in the coastal swamp depobelt of the Niger Delta. Utilizing well log data and 3D full stack seismic data, the team employed model-based deconvolution to invert the stacked sections into pseudo-velocity sections. The study highlighted the efficacy of model-based inversion in characterizing thin sand intervals in heteroliths found in the Niger Delta, particularly when there's good well control in study (Austin et al., 2018).

Ahmed et al.'s 2015 research investigated the application of Amplitude Versus Offset (AVO) forward modeling and attribute analysis in distinguishing fluids in geological formations. Using 3D seismic data and wireline logs, the study determined that AVO attributes, especially the fluid factor and intercept attributes, effectively differentiate hydrocarbon formations from background sands, highlighting clear contrasts between oil and gas sands versus water sands (Ahmed et al., 2015).

In the 2017 research article by Tayyab & Asim, the application of spectral decomposition techniques, specifically continuous wavelet transforms (CWT) were applied to 3D post stack seismic data from the Indus Basin in SW Pakistan to detect fluvial sand reservoirs. The research revealed that CWT effectively pinpointed potential hydrocarbon-rich sands at various depths. When integrated with standard seismic attributes and 3D visualization, CWT improves reservoir characterization and aids in determining the best well placements, as evidenced in the Miano gas field. (Tayyab & Asim, 2017).

1.5 Research Gap

The research findings from numerous scientists indicate that the primary focus has predominantly been on interpretation, petrophysics and seismic inversion. Over recent years, the industrial application of machine learning, particularly in seismic interpretation and inversion, has gained significant attention. Based on the thorough examination of the literature mentioned earlier, it becomes evident that there is a compelling requirement for conducting research focused on detecting thin beds and automating the classification and modelling of facies within the Lower Goru Formation of Kadanwari Gas Field. This research will utilize the most efficient machine learning algorithms currently available.

1.6.1 Objectives of Research Work

The study aimed to accomplish the following goals:

1. The identification of different horizons and subsurface faults through seismic structural interpretation.
2. The reservoir characterization of Lower Goru Sand intervals by petrophysical analysis and model-based seismic Inversion.
3. Evaluation of the most optimized seismic attributes applied on seismic data to confirm structural and stratigraphic interpretation specifically in the context of thin bed detection.
4. Machine Learning-Based Vs Computation, AVO Validation, and Facies Modelling.
5. Geomechanics with Automated Pre-Conditioning of Petrophysical Logs Using Machine Learning.

1.7 Methodology of Research

The comprehensive workflow for the entire work procedure can be found in Figure 1.2 provided below.

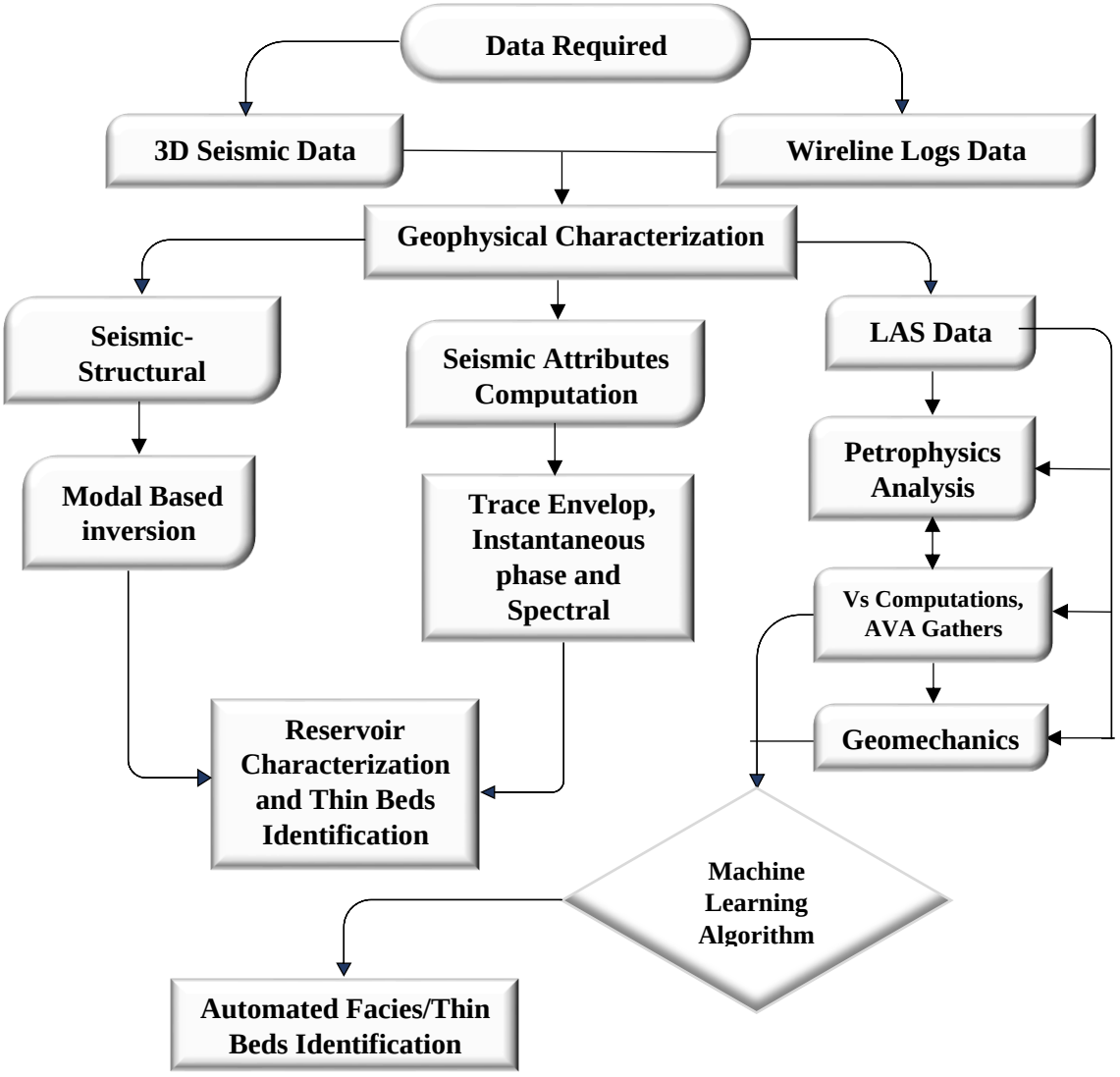

Figure 1.2 Methodology adopted for research work.

The work procedure begins by assessing the reservoir quality within the Kadanwari cube using conventional 3D seismic interpretation methods and structural analysis. Next, conduct a petrophysical interpretation to highlight zones of interest within target formations, specifically the G, F, and E sand intervals of the Lower Goru Formation. A model-based post-stack inversion algorithm is then employed to characterize the reservoir. To identify thin beds, attributes such as instantaneous phase, trace envelope, and spectral decomposition are applied. In addition, ML techniques are used to compute sonic shear (Vs) values, which are also derived from the Castagna equation. The sonic shear (Vs) outcomes are then validated using AVO/AVA (Amplitude Versus Offset/Angle) gathers. Conclusively, geomechanics are conducted with an

emphasis on automating the pre-conditioning of petrophysical logs via machine learning, which facilitates the automatic detection of layer boundaries in the Lower Indus Basin.

1.8 Data Availability

Upon receiving approval from the Directorate General of Petroleum Concessions (DGPC) for the purposes of the MS thesis, data was sourced from LMKR. Two types of data have been acquired.

1. **Seismic data**

   The seismic dataset comprises 12 square kilometres of 3D seismic data cube of Kadanwari area.

2. **Well data**

   The well data includes a full suite of well logs and well tops for three exploratory wells:

   a) Kadanwari-03
   b) Kadanwari-10
   c) Kadanwari-11

1.9 Required Software

1. Kingdom suite/Interpretation suite for Seismic interpretation and Attributes.
2. K-tron Wavelets Software for Machine learning work.
3. Hampson-Russell Software for Inversion.
4. G-Verse Geographics for Petrophysical analysis.
5. K-tron Precision Matrix for location map generation

CHAPTER 2

REGIONAL GEOLOGY, TECTONICS, AND STRATIGRAPHY

2.1 Geological Configuration of the Middle Indus Basin

There are essentially two types of faults: normal faults, which result from an extensional regime, and reverse faults, which are generated due to compressional forces or a compressional regime. The Middle Indus Basin is situated within an extensional regime, exhibiting a horst and graben structure that covers a substantial portion of the basin (Kemal et al., 1991).

Near the Kirthar Fold Belt, the Middle Indus Basin comprises a passive roof and a passive back thrust. The passive roof thrust forms a frontal culmination wall at the Kirthar Fold Belt's margin and extends beyond the syncline intra-molasses detachment fault, which is located in the Kirthar Fore-deep (Zaigham and Mallick 2000).

2.2 Structural Setting of the Kadanwari area

The Kadanwari area is situated within an extensional regime and exhibits a horst and graben structure. This geological structure spans from strata beneath the Paleocene era to the Cretaceous era. The sands found in the Lower Goru Formation, marked as Intervals A, B, C, D, E, F, and G, hold particular importance for exploration in this region. The Lower Goru Formation has a westward dip and follows a NW-SE trending orientation (Kazmi and Abbasi, 2008). The Kadanwari Gas field is situated within the Panno-Aqil graben, flanked by the Mari–Kandhkot and Jacobabad–Khairpur Highs in the Middle Indus Basin of Pakistan, depicted in Figure 2.1 (Rehman et al., 2016).

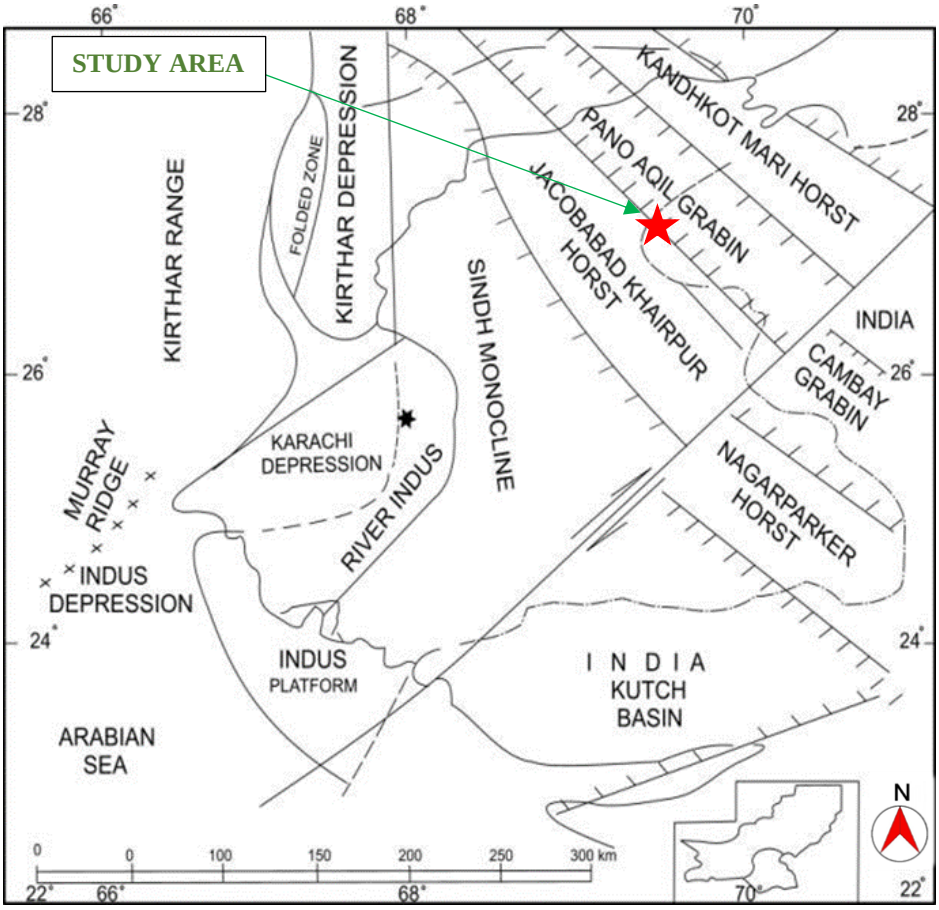

Figure 2.1 Tectonic map of the Kadanwari region, illustrating major tectonic features in the vicinity (Modiefied after Jadoon et al., 2020)

Hydrocarbon migration from the Sembar Formation occurs through fault planes towards the reservoir. It's worth noting that due to the absence of outcrops in the study area, structural interpretation relies solely on seismic data interpretation.

2.3 Regional Geological Setting of study area

The Kadanwari Gas field is situated on the southeastern flank of the regional Khairpur-Jacobabad High, making it one of the most southern gas fields of the Middle Indus Basin (MIB). This elevation plays a crucial role in creating traps within the Kadanwari Gas Field (Ahmad et al. 2007). The formation of this high was accompanied

by vigorous tectonic activity, resulting in numerous hydrocarbon-bearing structural traps in its surrounding regions, including the area being studied. During this period, several stratigraphic and combined structure-stratigraphic traps also emerged (Kazmi and Jan, 1997). Gas fields like Kadanwari, Miano, and Sawan serve as examples of these stratigraphic and structure-cum-stratigraphic traps.

The Indus Basin stretches across the Pakistan's northwestern regions and the western parts of India, encompassing an approximate area of 873,000 km². It is flanked by the MMT in the north, the offshore Indus to its south, and the Indian Shield on its eastern side. The Indus Basin's western edge is delineated from the Baluchistan Basin by the Bela – Muslim bagh - Waziristan Ophiolitic belt (Wandrey et al., 2004). The Indus Basin can be categorized into two main regions: the upper section and the lower section, which is itself further divided into central and southern basins. In the platform area, certain basement highs serve as boundaries. The Sargodha High demarcates the Upper Indus Basin from the Middle Indus Basin. On the other hand, the Jacobabad High differentiates the Middle Indus Basin from the Lower Indus Basin. Kadanwari region has been divided into horst and graben structures because of wrench faulting. The Lower Goru Formation (LGF), predominantly made up of alternating layers of sand and shale, accounts for most of the production in this area (Ehsan et al. 2018).

The area is geologically separated into two distinct zones: the foldbelt and the foreland areas. The foldbelt encompasses the Kirthar Range, which forms the western edge of the Indo-Pakistan Plate. On the other hand, the foreland, known as the Kirthar Foreland, is characterized by a continental shelf that slopes gently to the west. This foreland stretches eastward to the Indian Shield and extends southward, reaching the Indus offshore fan (Wandrey et al., 2004).

2.4 Regional Tectonic Setting of Study Area

In terms of tectonics, the Kadanwari Gas field is positioned between two significant regional high areas, namely the Mari-Kandhkot High and the Jacobabad-Khairpur High (as illustrated in Figure 2.2). To the east, it is demarcated by the Indian Shield, while its northern boundary is defined by the Sargodha High. In the west, it is

bounded by the fold and thrust belt of the Kirthar and Sulaiman Ranges, and to the south, it is bordered by the Jacobabad-Khairpur High (Zhang et al., 2022).

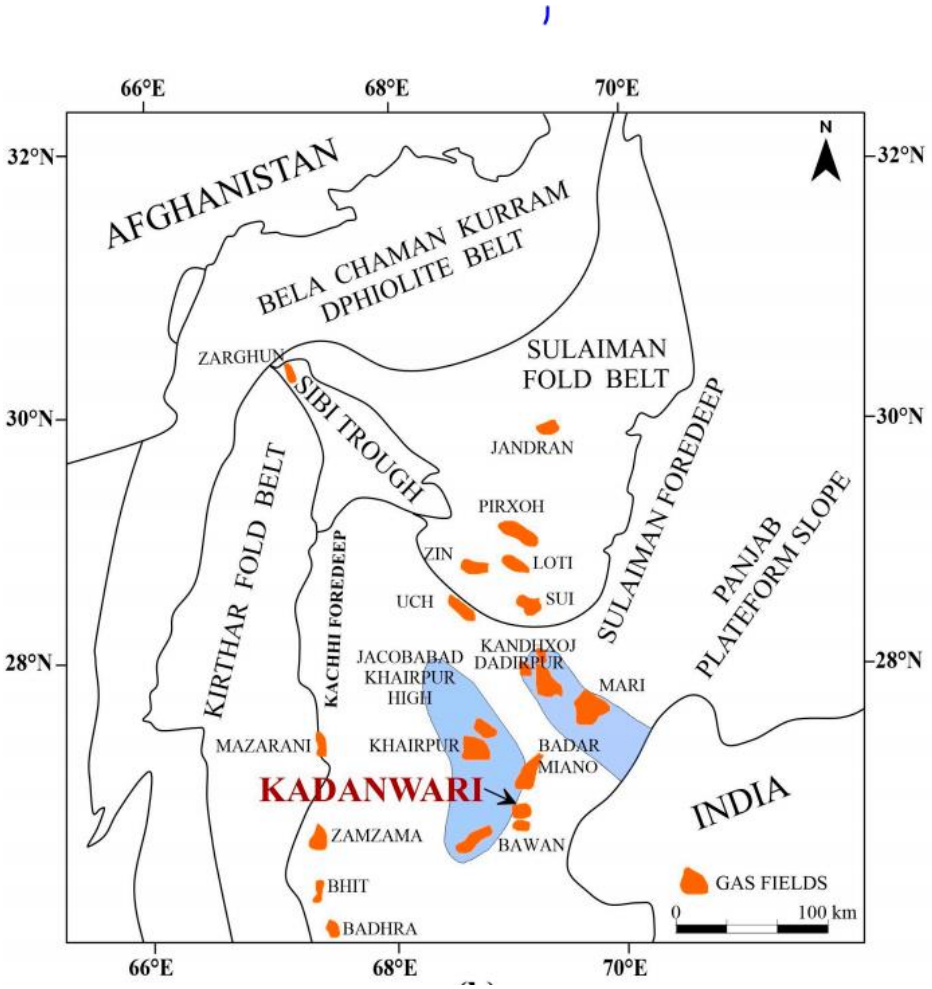

Figure 2.2 Tectonic Map of the study area, surrounded by adjacent gas fields (Zhang et al., 2022)

The Kadanwari Gas field comprises numerous low-relief faults, creating dip closures beneath the surface. These faults play a crucial role in creating stratigraphic trapping elements. Of particular importance are the dip closures formed by these faults and the wrench faults, as they partition the Kadanwari Gas field into distinct reservoir sections (Ali et al., 2019).

The structural features in the Kadanwari Gas field and neighbouring fields within the Central Indus Basin have been influenced and shaped by three primary tectonic events (Kazmi & Jan, 1997), as outlined below:

a) The first tectonic event occurred towards the end of the Cretaceous period. During this time, there was an uplift of the Kadanwari Gas field in the northern and western directions.
b) The second phase of this tectonic activity in the region involved extensive deep-seated strike-slip faulting with an NW-SE orientation. These faults traversed through the entire Mesozoic section, penetrating deep into the formations, including the Chiltan Formation, and extending into younger Mesozoic rocks.
c) The third tectonic event involved a significant basin inversion that occurred during the Late Tertiary period. This inversion led to the formation of the Jacobabad High (Figure 2.2).

2.4.1 Uplifting Phase of the Major Tectonic Event (Late Cretaceous)

Seismic investigations in the region have revealed the truncation of the Upper Cretaceous sedimentary layers by the base of the Tertiary unconformity. Determining the extent of uplift is challenging due to the loss of several hundred meters of geological section to the west of the Kadanwari Gas field. The orientation of this Late Cretaceous feature aligns with the present-day Jacobabad High, following a NNE/SSW trend (Ahmad and Chaudhry, 2002).

2.4.2 Wrench Faulting Phase of the Major Tectonic Event (Late Paleocene/Early Eocene)

Structural features in both Cretaceous and Tertiary strata were influenced by basement-related wrench faults, with these faults originating during the Late Paleocene to Early Eocene period. Four primary sets of wrench faults are identified in the studied

area, cutting across the entire Mesozoic sequence, from deeper rocks to younger formations. These faults exhibit predominantly vertical to sub-vertical orientations, aligning in a NNE to SSW direction in the field. As these deep-seated faults intersect with younger Mesozoic rocks, they interact with smaller faults within those formations. This interaction results in the creation of negative flower structures in the region, indicative of strike-slip deformation (Khan et al., 2022).

2.4.3 Inversion Phase of the Major Tectonic Event (Late Tertiary)

During the Late Tertiary period, a substantial inversion process significantly impacted the Kadanwari Gas field. The axis of this inversion is believed to be the Jacobabad High, located approximately 20 kilometres west of the field. The high exhibits a NNW-SSE orientation. On the eastern side of the Kadanwari Gas Field, the rate of uplift associated with this high begins to decrease.

Simultaneously, while the larger-scale inversion was occurring and the Jacobabad High was forming, a smaller-scale inversion process commenced due to the tectonic conditions in the Kadanwari Gas field area. This smaller-scale inversion resulted in the formation of a low-relief anticline observed in the upper E Sand, sharing the same orientation as the Jacobabad High (Nasir et al., 2011).

2.5 Stratigraphy of the Study Area

In the Cretaceous period, sedimentary rocks were deposited, with the major source rocks being the Sembar Formation and the major reservoir rocks being the Goru Formation. In the early Cretaceous period, following the initiation of the northward rift of the Indian plate, the Lower Indus Basin began to experience a significant influx of clastic sediments (Zaigham and Mallick, 2000). This influx led to the deposition of the clastic Sembar and Goru Formations. The Sembar Formation primarily consists of black shale, siltstone, and argillaceous limestone. It is found to unconformably overlie the top of the Jurassic Chiltan Limestone (Wandrey et al., 2004). Situated above the Sembar

shales, the Goru Formation lies conformably and is further subdivided into the Upper and Lower Goru Formations. While the Formations of Lower Goru features a mix of sand and shale layers, the Upper Goru Formation is mainly made up of shale and marl. These early Cretaceous Sembar and Goru formations play a pivotal role in defining the primary petroleum prospects within the area (Zaigham and Mallick, 2000). Figure 2.3 presents the stratigraphic column specific to the study area, while Figure 2.4 illustrates the generalized stratigraphic column for the Middle Indus Basin. In both figures, the source rock, reservoir rock, and seal rock are depicted as rectangular boxes within the stratigraphic columns.

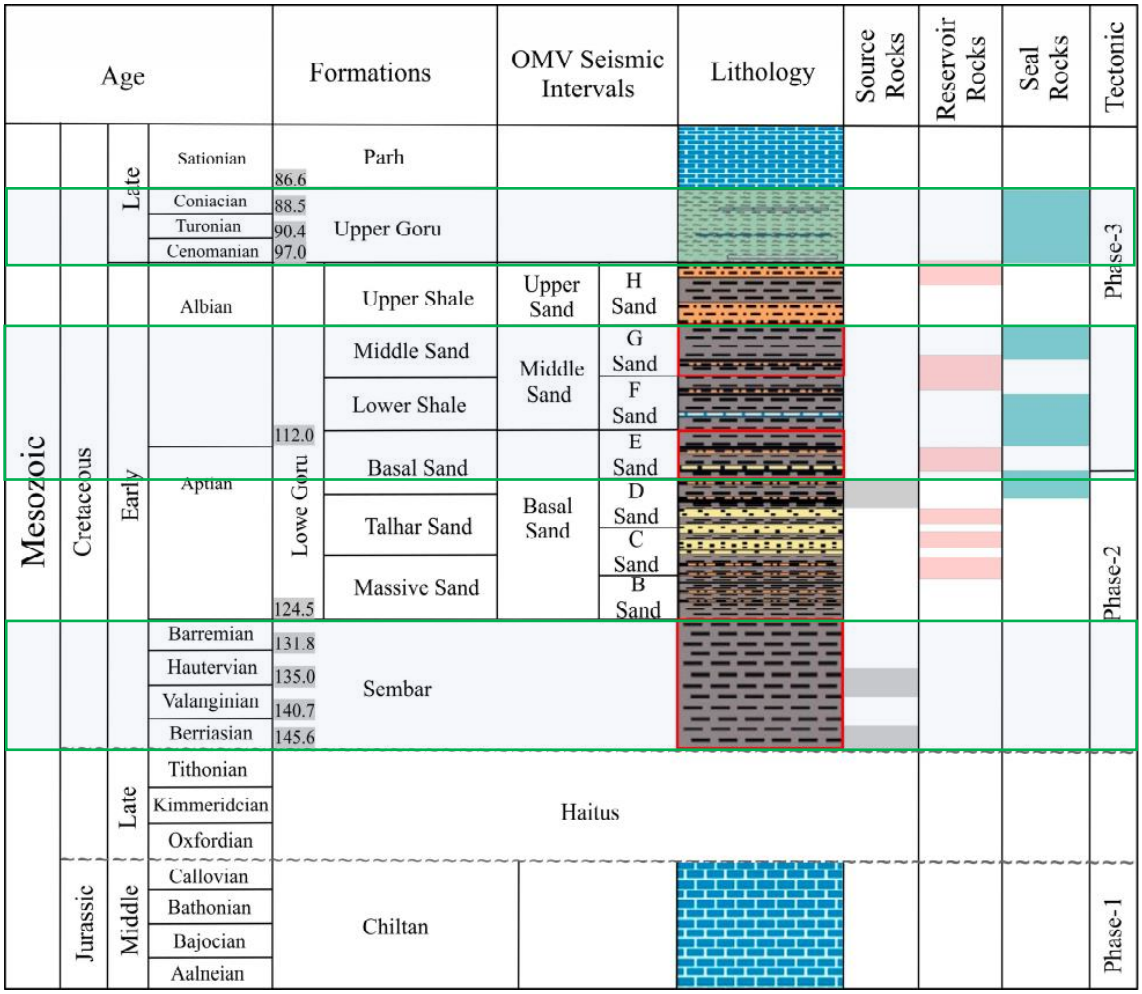

Figure 2.3 Stratigraphic chart of study area, highlighted formations of interests in rectangular box (Modified after Khan et al., 2022; Ahmed et al., 2004)

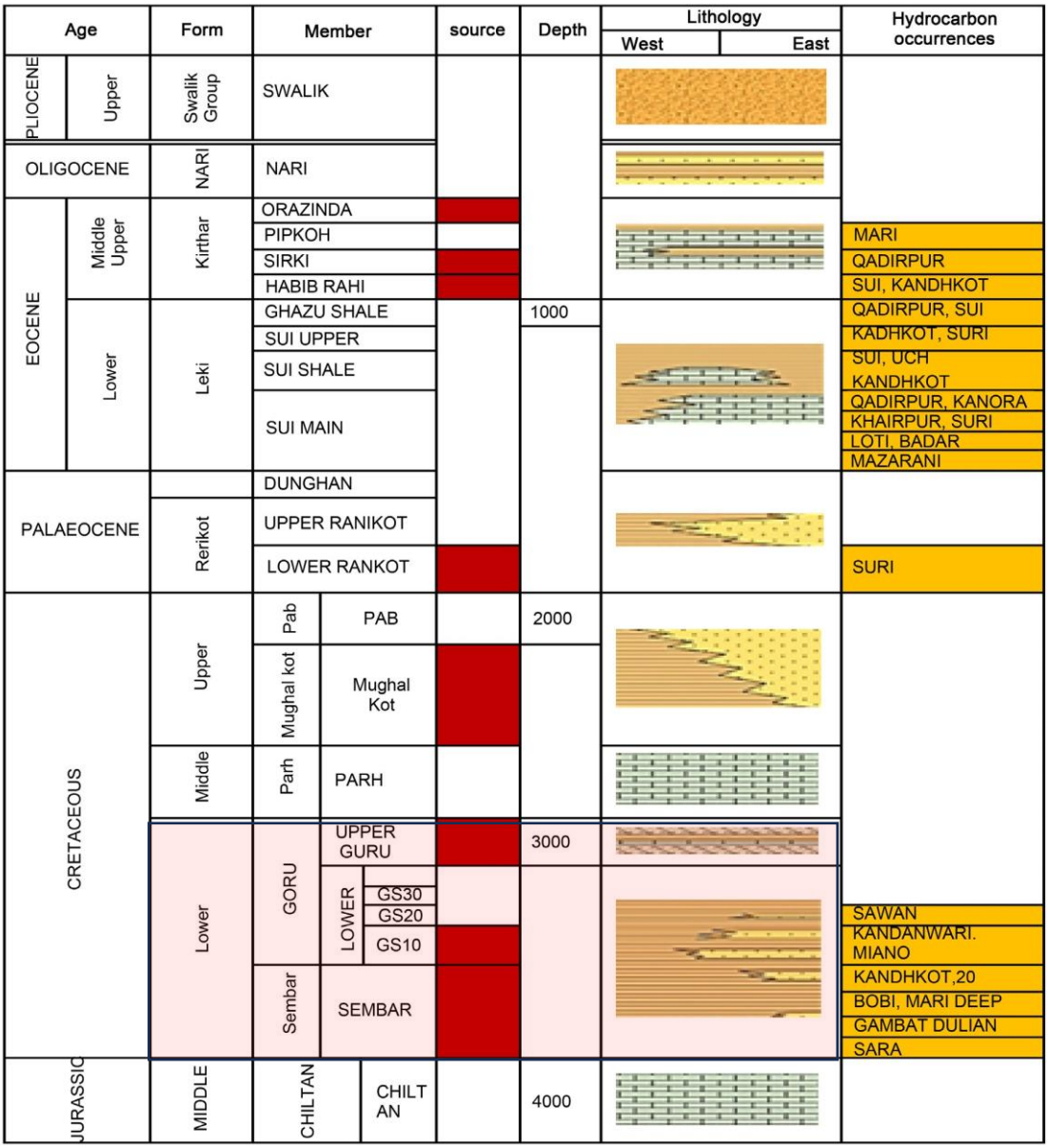

Figure 2.4 Generalized stratigraphic profile of the Middle Indus Basin (Shakir et al., 2021).

2.6 Paleo Depositional Environments of Reservoirs of the study area

The Lower Goru Formation (LGF), which dates back to the Cretaceous period, was formed in a shallow marine deltaic setting during a period of low sea levels. The

formation consists of detached medium-to-coarse-grained sediments that are layered on top of the more distal sediments (shale and siltstone) from the preceding high stand system tract (Berger et al., 2009).

The Lower Goru sands, which have been identified as reservoirs in the Kadanwari Gas field, originated from a coastal estuarine system. This system was consistently influenced by longshore currents and tides over an extended period. The volume of sand being deposited at that time, in conjunction with these two processes, significantly determined the quality of these sand reservoirs. During the C sand deposition phase, there was a limited influx of sand. Major shifts were noted both in alignment with the shoreline (longshore bars) and perpendicular to it (estuarine/tidal channel bars). However, during the D and E sand deposition stages, there was a substantial increase in sand influx. The deposition pattern became predominantly aligned with the shoreline as the shallow sands underwent modifications due to longshore activities. Throughout the sedimentation periods for C, D, and E sands, the ancient coastline was oriented in the northeast-to-southwest direction. In the Kadanwari well, the C sand's average thickness ranges from 8 to 10 meters. In contrast, the vertical thickness of D and E sands can reach up to 26 meters. The D and E sand facies originated from a rich shore-parallel depositional sequence, making them consistent throughout the Kadanwari Gas field and easy to correlate. Meanwhile, the C sand facies are derived from a sand-deficient depositional sequence and can be matched in areas where estuarine and tidal channels are present (Ahmad et al. 2007).

G-sand is a component of the Lower Goru Formation. These G sands are characterized as clastic deltaic deposits that were laid down in a fluvial-to-shallow water environment during the Early Cretaceous period. Both G and E-sands receive their hydrocarbon charge from the shales found in the Lower Goru and Sembar formations. The seal for these hydrocarbons is created by transgressive marine shales originating from the Upper Goru Formation. F-sand is a component of the Lower Goru Formation, primarily consisting of delta-front sediments. The reservoir's formation results from a combination of high-discharge events that create mouth bars containing high-quality sand. During low-discharge periods, smaller mouth bars form, characterized by shale/silt-dominated delta fronts. The resulting reservoir is relatively thin, approximately 5-10 meters thick, with a gradual change in sediment characteristics. In later stages, mud-prone interlopes develop, serving as lateral seals within the reservoir (Ali et al., 2022).

2.7 Petroleum Play of the Study Area

The Kadanwari Gas Field is renowned for possessing a well-established petroleum play system, encompassing confirmed reservoir rocks. Some of the significant components that collectively characterize the petroleum system in the area and are collectively referred to as the Sembar/Goru petroleum system (Wandrey et al., 2004) include:

2.7.1 Source rock

The Lower Cretaceous Shale within the Sembar Formation has been confirmed as a reliable source of both oil and gas in the region, largely attributed to its high organic content and optimal thermal maturity. The Sembar Formation is predominantly composed of type-III kerogen, which has the capacity to generate natural gas. In terms of reservoirs, the primary ones consist of deltaic and sandstones from a shallow-marine environment situated in within the region's Lower Goru Formation (Kadri, 1995).

The shales found in the Lower Goru sands & Sembar have been identified as the primary source rocks in the MIB and LIB (Raza et al., 1990). These shales are regarded as the primary source of dry gas in the study area. Nevertheless, it's worth noting that carbonates and shales from deeper horizons may also play a role as potential sources of hydrocarbons.

2.7.2 Reservoir rock

Within the Kadanwari Gas Field , the primary reservoirs are comprised of Eocene carbonates and Cretaceous Lower Goru sands (Kadri, 1995). Notably, recent significant discoveries have been made in the Lower Goru sands. Eni, a company involved in the field, has undertaken a detailed categorization of the Lower Goru sands, dividing them into subgroups, spanning from A to H-Sand intervals. Within these subgroup classifications, G-Sand and E-Sand are significant contributors as reservoirs. They exhibit

distinct behavior due to the presence of a shale member that acts as a barrier, effectively separating them (Ahmad and Chaudhry, 2002).

2.7.3 Cap or seal Rock

To confine hydrocarbons within the reservoir, the presence of a barrier is essential, and such barriers are referred to as cap rocks. In the study area, the Upper Goru Formation functions as a cap rock, characterized by a stratigraphic sequence primarily composed of marl and silt (Kazmi and Abbasi, 2008).

The petroleum system predominantly relies on shale as its primary sealing mechanism. These shales are typically interspersed with sand layers and are positioned above the reservoirs. In producing fields, thin shale beds of varying thicknesses effectively serve as sealing layers. Additionally, other sealing mechanisms come into play, including impermeable seals situated above truncation traps, along fault lines, and as a result of facies changes in up-dip areas (Ahmad and Chaudhry, 2002). In the area under study, the Upper Goru shale and the interbedded shales within the Sui Main Limestone formation play a vital role as impermeable barriers, functioning as effective seals for the hydrocarbon reservoirs (Ali et al., 2022).

2.7.4 Trapping Mechanism

The Kadanwari Gas Field is positioned on the eastern and southeastern flanks of the Khairpur High, which extends in a north-south direction. This high is of considerable importance in the creation of hydrocarbon traps within the Kadanwari region. Within the study area, the traps primarily showcase structural features that have emerged from a combination of extensional and trans-tensional events. These events have led to the development of a notable trapping system, especially along tilted fault blocks and negative flower structures. Nevertheless, the most prominent traps are linked to trans-tensional outcomes, particularly negative flower structures (Ali et al., 2022).

CHAPTER 3

3D SEISMIC INTERPRETATION

3.1 Introduction

The primary aim of conducting seismic interpretation is to identify and map all potential subsurface information and geological features using 2-D or 3-D seismic data processing techniques. The interpretation of seismic surveys focuses on locating structures, faults, and zones of horizons that are conducive to the accumulation of hydrocarbons (Badley, 1988). The geology of the region where the seismic reflection data was collected is crucial to accurately interpreting the data. A geological model is constructed through the process of interpretation, which provides a reasonably accurate subsurface representation of the area (Yilmaz, 2001)

Seismic reflection data, which provides acoustic images of the subsurface, holds significant importance in enhancing our comprehension of sedimentary, tectonic, and magmatic systems (Wrona et al., 2021). Conventional seismic interpretation involves the identification and monitoring of seismic reflectors that exhibit lateral consistency. This process is done with the objective of mapping geological structures, stratigraphy, and reservoir architecture. The ultimate goal is to identify the presence of hydrocarbon accumulations, define their boundaries, and quantify their volumes (Coffeen, 1986). Stratigraphic analysis and structural analysis are the two main approaches used to interpret seismic data.

3.1.1 Stratigraphical & Structural Analysis

Stratigraphic analysis involves the interpretation of sedimentary sequences that are genetically related, and which exhibit variations in the depositional environments of

sediments. Stratigraphic traps can arise from various geological features, such as erosional truncation, pinch-outs, reefs, etc. The extensional regime is the most common setting for stratigraphic investigation (Bashir et al., 2021).

Structural analysis of the seismic section is conducted to identify any probable structures that might store and accumulate hydrocarbons. Numerous structural interpretations make use of two-way seismic reflection time rather than depth. Structural analysis searches for hydrocarbon-hosting structural traps such anticline, dome, horst, graben, pop-up structures, growth faults, flower structures, imbricate, and duplex structures (Kearey, 1996).

3.2 Work Procedure of Seismic Interpretation

The workflow of seismic interpretation steps that are taken to interpret the 3D seismic data is shown in Figure 3.1.

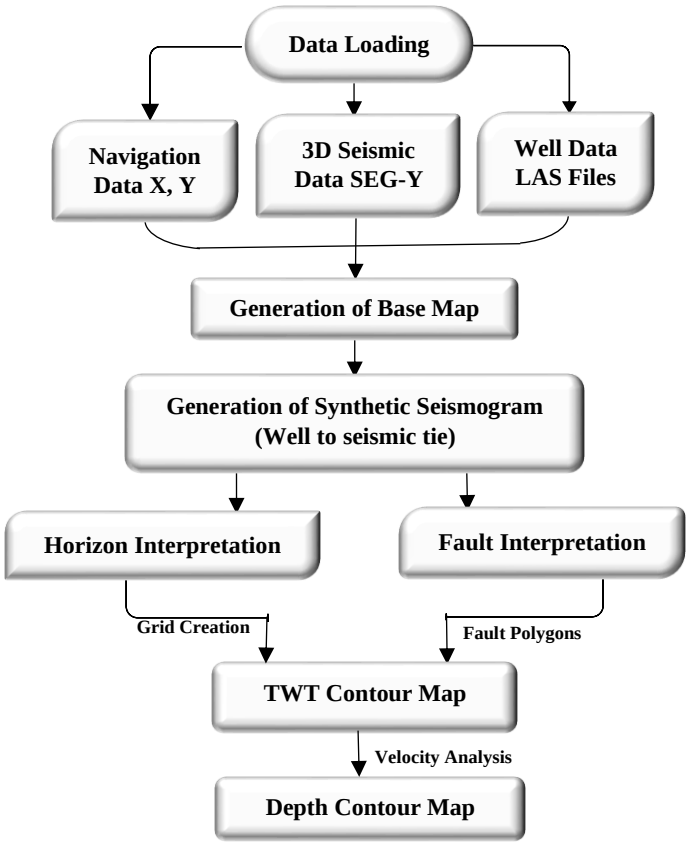

Figure 3.1 Workflow adopted for seismic data interpretation.

The seismic interpretation methodology employed for data analysis was conducted using the Kingdom SMT 8.6 software. The initial step involves loading the seismic & well data into the interpretation software. The second step involves conducting a quality assurance assessment of the seismic data to determine its suitability for utilization purposes. During the third step, a correlation is established between the well data and seismic data. There are two methods that can be employed to achieve this objective. The first method involves generating a Well Correlation, while the second method involves generating a Synthetic Seismogram. The Well Correlation method is utilized for fault interpretation, whereas the Synthetic Seismogram method is employed for horizon interpretation. Based on these interpretations, a TWT (Two-Way Travel Time) map is generated and subsequently converted into a depth map using the Depth Conversion process. The created depth map is used for prospect identification since it shows how promising the region is or provides insights into the potential of a given area.

3.3 Seismic data loading

The provided dataset comprises a 3D seismic data cube covering 12 * 12 km^2 of the Kadanwari block, which is accessible in the SEG Y format. The data is imported into the Kingdom SMT 8.6 software by utilizing SEG Y headers for the purpose of inline and crossline loading. Furthermore, the well data, comprising LAS files of Kadanwari 3, 10, and 11, were also imported into the software. A lot of attention is required throughout the process of data loading, since even minor inaccuracies could have severe consequences, potentially leading to critical outcomes. The integration of 3D seismic data and well data in the Kadanwari region enables a comprehensive analysis.

3.3.1 Base Map

Once the seismic data loading procedure is complete, a base map is generated to depict the orientation of the overall grid for the Kadanwari block. The base map is composed of two distinct categories of lines: inline, which extend from 1911 to 2111, and crosslines, span from 1730 to 2132, as illustrated in Figure 3.2. The inline direction is

oriented from northeast to southwest, while the crossline direction spans from northwest to southeast. Kadanwari 11 is located at the intersection of inline 1972 and crossline 1995. Kadanwari 10 is positioned at the intersection of inline 2013 and crossline 1969. Kadanwari 03 is found at the intersection of inline 2004 and crossline 1798.

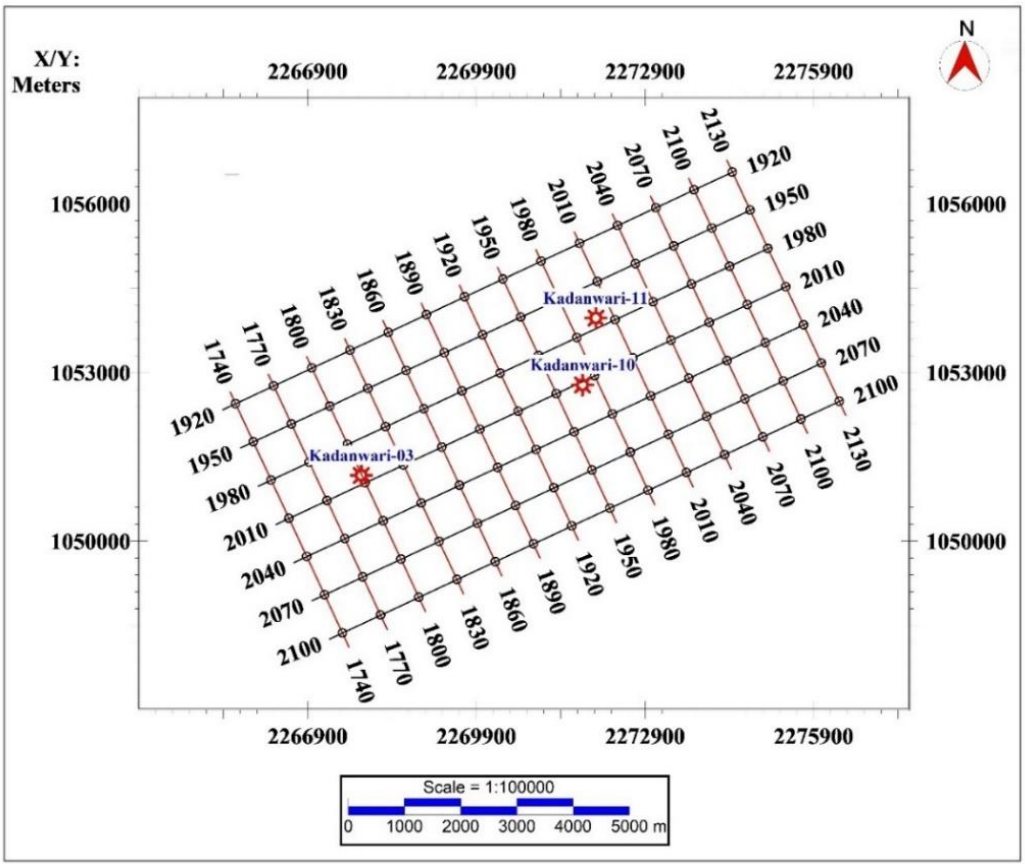

Figure 3.2 Base Map of Kadanwari Block

3.3.2 Synthetic Seismogram Generation

A synthetic seismogram refers to a seismic response that is derived from well data. The Synthetic seismogram was generated by utilizing the Time-Depth chart and well logs data (specifically sonic and density logs) acquired from well Kadanwari 11. Figure 3.3 depicts the workflow of synthetic seismogram generation.

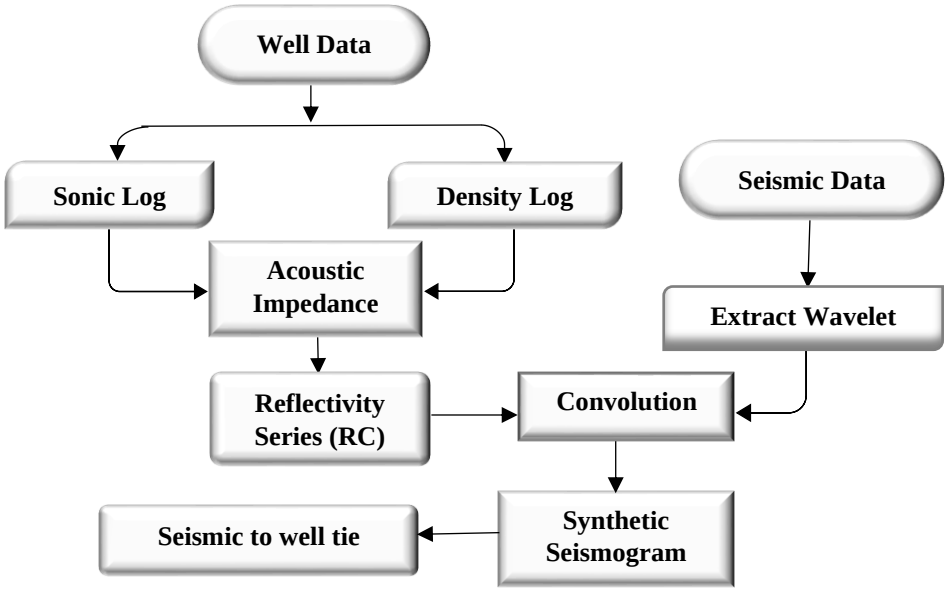

Figure 3.3 Workflow adopted for synthetic seismogram generation.

The seismic interpretation methodology employed for data analysis was conducted using the Kingdom. The acoustic impedance (AI) log is derived from well logs, namely the bulk density and sonic log. The statistical wavelet was derived from the control line, which was located directly under SP 1981, where the well was located. The reflection coefficient series (RC) was obtained by convolving this wavelet with AI contrast. Subsequently, this RC is then convolved with the source wavelet (Theoretical or Extracted) to produce the synthetic seismogram. The primary purpose of a synthetic seismogram is to calibrate seismic reflections by aligning them with formation markers derived from the well logs. Utilizing the generated seismogram to validate the horizon. The horizons that were selected are as follows:

i. G Sand

ii. F Sand

iii. E Sand

Figure 3.4 displays the synthetic seismogram.

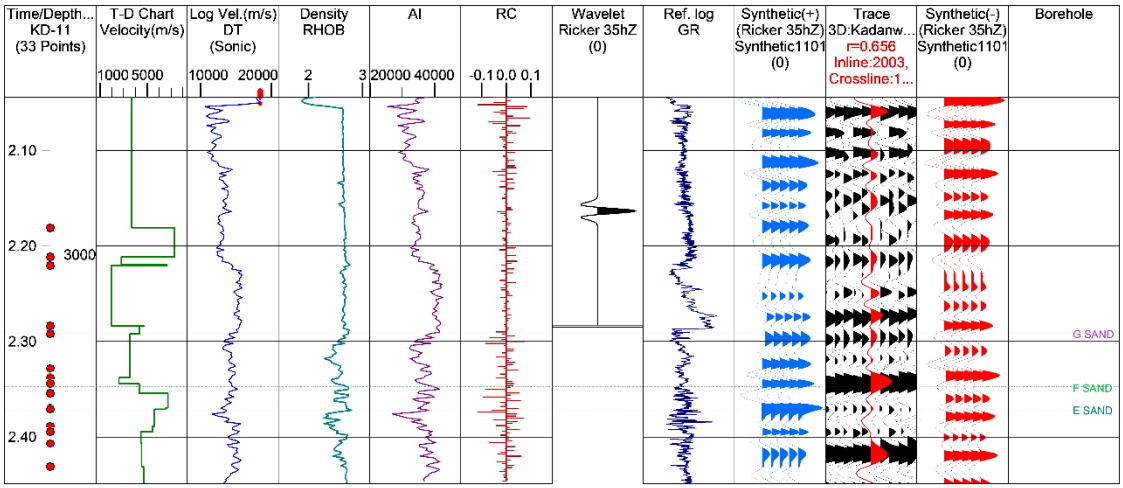

Figure 3.4 Synthetic seismogram generated from Kadanwari-11 well.

3.3.3 Seismic to Well Tie

The seismic data is represented in the time domain and possesses a low-frequency content. In contrast, well-log data is presented in the depth domain and exhibits relatively higher frequencies. So, to create a correct time-depth relationship, the process of seismic-to-well tie is employed to establish a correlation between well log data and seismic volume in the proximity of the well. The establishment of time-depth relationships is typically based on check shots or the assignment of sonic log calibration to the well. If any mismatches are observed, various processes can be employed. Sometimes, a simple time shift is sufficient. Otherwise, the synthetic trace may be stretched and squeezed to get the best match with the seismic trace. This method allowed for the identification of horizons by getting the most precise match at reservoir levels. Once the well to seismic tie correlation was established, synthetic seismogram was then shown on control lines for the purpose of horizon picking as shown in Figure 3.6 given in next sections below.

3.3.4 Horizon Interpretation

The fundamental responsibility of a seismic data interpreter is to analyze and interpret various horizons present in a seismic section. The interpreter must possess

comprehensive knowledge regarding the various structures that exist within the designated area, as well as a thorough understanding of the stratigraphy. The correlation between the well tops and the seismic data is utilized to precisely identify the positions of the horizons on the seismic section (Stewart, 2012).

To interpret the horizon, activate the seismic interpretation under processes in the input window. The synthetic and well tops were then presented on the seismic section. This was done to identify the event that required interpretation. Figure 3.5 depicts three horizons interpreted on seismic section using the well-seismic tie information from the synthetic seismogram, with TWTs ranging from 2.3 to 2.4. The selected horizons represent sand intervals of Lower Goru Formation, which are as follows:

i. G Sand
ii. F Sand
iii. E Sand

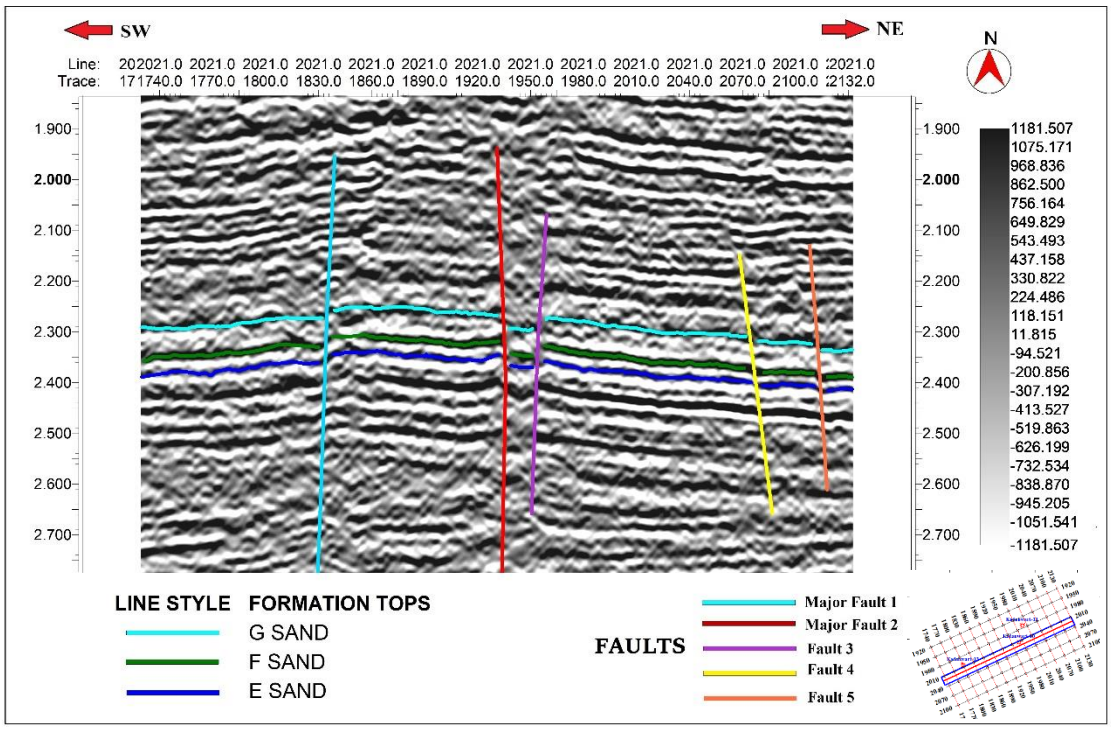

Figure 3.5: Seismic section along with horizons of interest and faults at inline 2021.

3.3.5 Fault Picking

Faults are identified and analyzed on seismic sections when there is a discernible discontinuity or fracture in the layers of rock. To accurately identify faults, it is imperative to have a comprehensive understanding of their behavior in response to regional stresses (Sheriff, 1995). Fault correlation refers to the development of a network of faults that traverse through various geological strata/formations. These faults serve as a conduit or passageway for hydrocarbon in oil and gas exploration. They also act as a geologic seal, preventing additional hydrocarbon migration from the reservoir. The faults are more obvious on the seismic inline, which is the seismic line that runs parallel to the strike (Munir et al., 2014). In my research field, I have identified five faults, and these are visually depicted in the interpreted figures, which are illustrated below in the following sections. The hunting tool was used to interpolate the data throughout the whole cube as each line was interpreted, enabling the software to automatically choose the proper horizons based on the identified interpretation Similarly, faults were highlighted on every single inline across the whole cube, and fault surfaces were produced for the entire cube.

3.3.6 Fault Polygons

The creation of fault polygons holds significant importance in the context of contouring a specific horizon in terms of both time and depth. In any mapping software, it is essential to convert all faults into polygons before initiating the contouring process. This is necessary because if a fault is not transformed into a polygon, the software won't identify it as a barrier or a disruption in contour lines. Consequently, this oversight could obscure potential closures influenced by faults, leading to an inaccurate portrayal of the subsurface.

3.4 Seismic Section Interpretation

The three horizons in the 3D volume cube were interpreted on the seismic i.e., G-sand, F-sand, E-sand, based on well to seismic correlation of synthetic seismogram. The

color scheme is utilized to distinguish the horizon. The trends of horizons and the style of structures were marked on the time-based seismic sections. In-line profiles have been chosen for interpretation as they run parallel to the structural dip. The orientation of inlines is NE to SW so horizons are also dipping in the same direction. Both G and E-sands receive their hydrocarbon charge from the shales found in the Lower Goru and Sembar formations. The seal for these hydrocarbons is created by transgressive marine shales originating from the Upper Goru Formation.

Kadanwari is situated in an extensional regime dominated by normal faults, the structures associated with it include horsts and grabens. The detection of the faults was made more difficult by low data quality. A total of five faults are interpreted from F1 to F5 with MF1 and MF2 being the major ones. Several faults, including MF1, MF2, and F3, persist throughout the section, spanning the whole survey area. However, the other two faults terminate within the center of the survey after interpretation on a limited number of lines. Major faults are identified by their depth of penetration, and they are all connected in the lower Indus at the level of Chiltan. All faults intersect the horizons of the Lower Goru sands, namely the G, F, and E sands. The faults identified within this formation are of a regional nature. Additionally, it was observed from the section that there was little or no horizontal displacement (fault heave) between the layers of strata. The trend of Major Fault F1 is from NE-SW and dipping toward the southwest SW. The trend of Major Fault F2 is from NW-SE and dipping toward southeast SE. Fault F3 trends generally in an NE-SW direction and is inclined or dipping towards the SW. Fault F4 trends generally in an NW-SE direction and is inclined or dipping towards the NE. Fault F5 trends generally in an NW-SE direction and is inclined or dipping towards the East.

The major faults, MF1 and MF2, are dipping away from each other, creating a horst-like structure in this region. On the other hand, MF2 and F3 faults dip towards each other, forming a graben. F3 and F4 are once again dipping away from each other, creating another horst-like structure, and F4 and F5 dip in the same direction towards the southeast, indicating normal faults. So, the identification of normal faults forming horst and graben structures on the seismic sections provides evidence that the Kadanwari Block is underlain by extensional tectonics. The Interpreted sections along with horizons and faults are shown in Figures 3.6 to Figure 3.9.

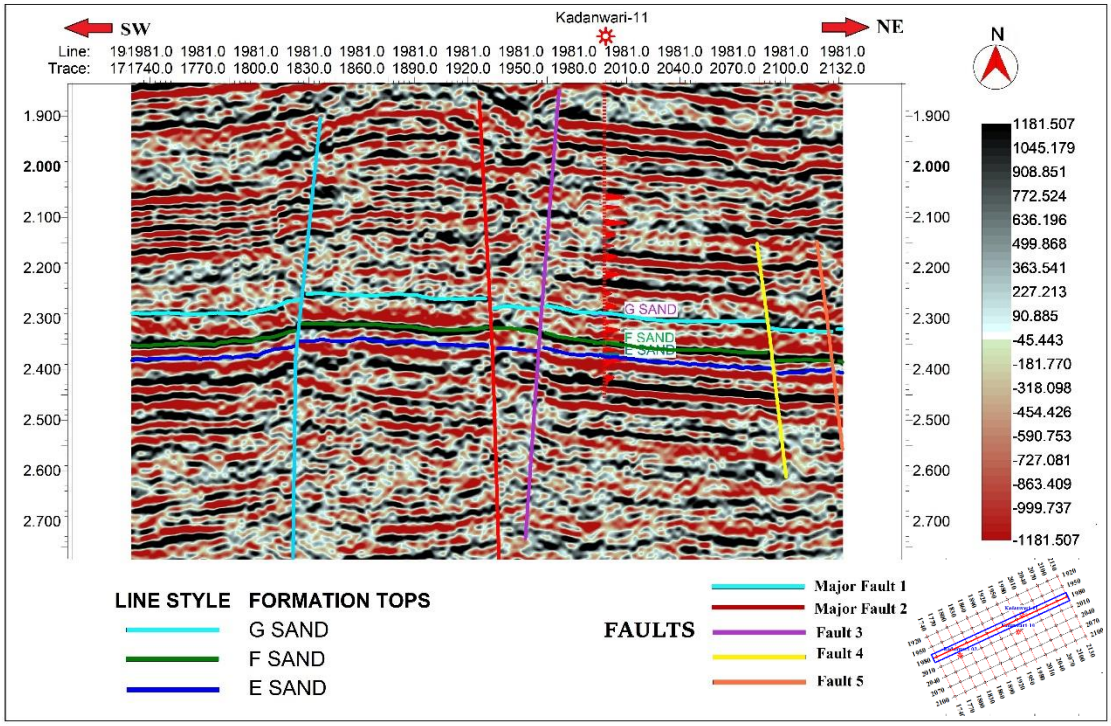

Figure 3.6 Interpreted seismic section depicting horizons and faults at Kadanwari-11 Well, Inline 1981.

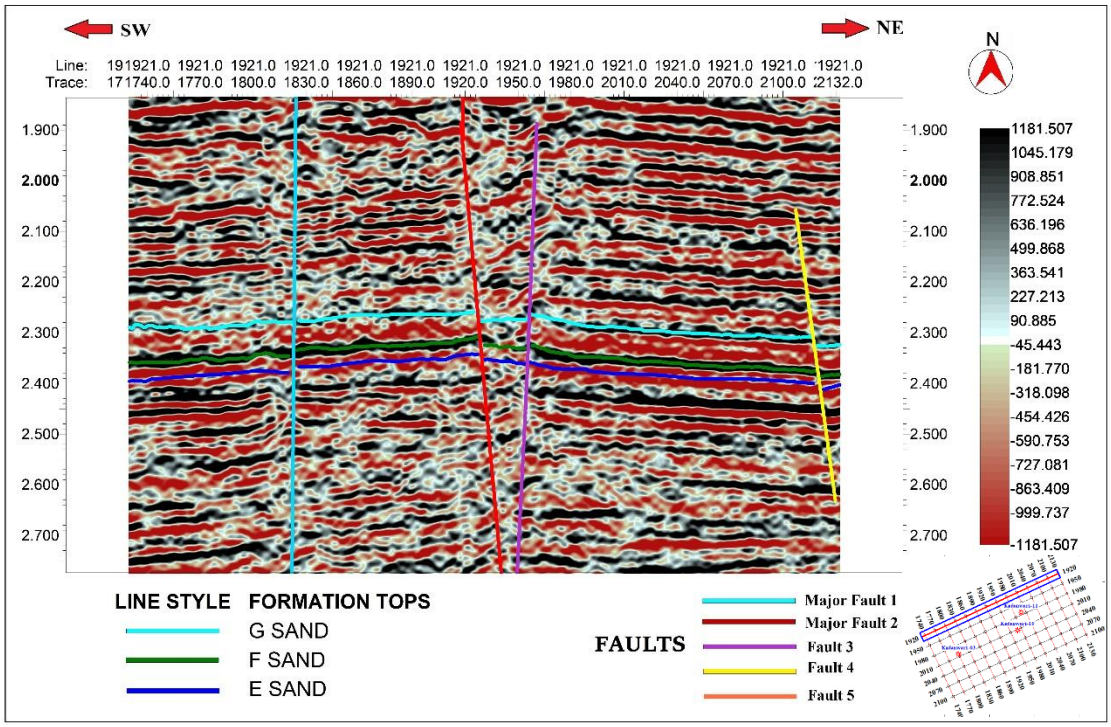

Figure 3.7 Interpreted seismic section depicting horizons and faults at Inline 1921.

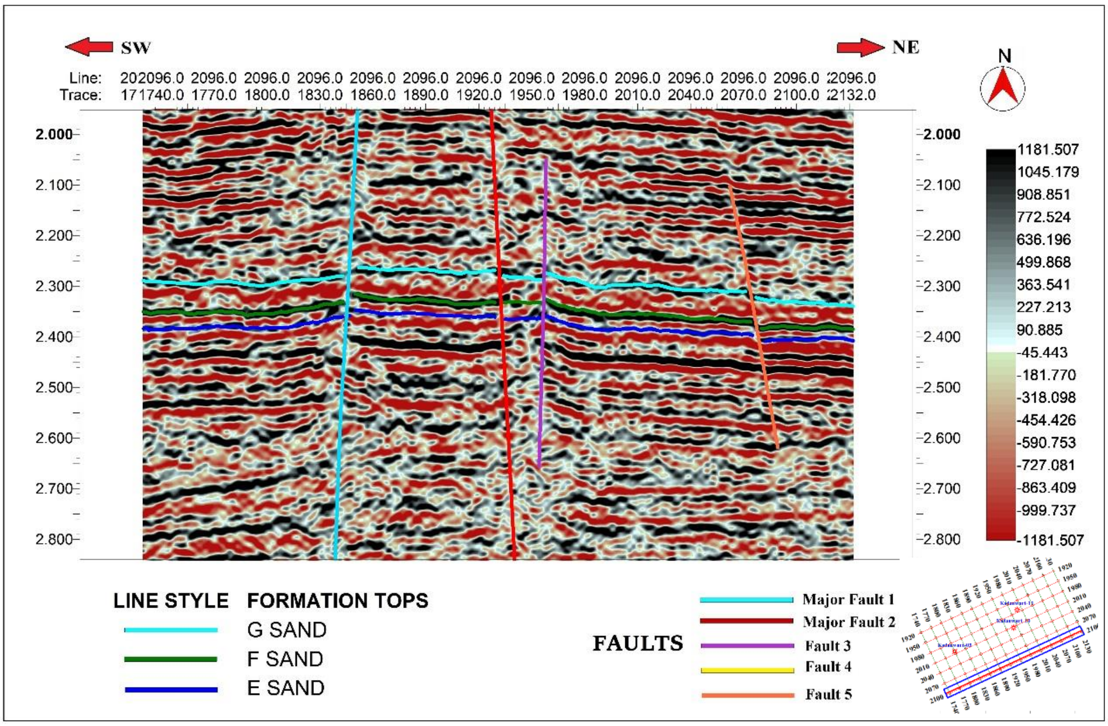

Figure 3.8 Interpreted seismic section depicting horizons and faults at Inline 2096.

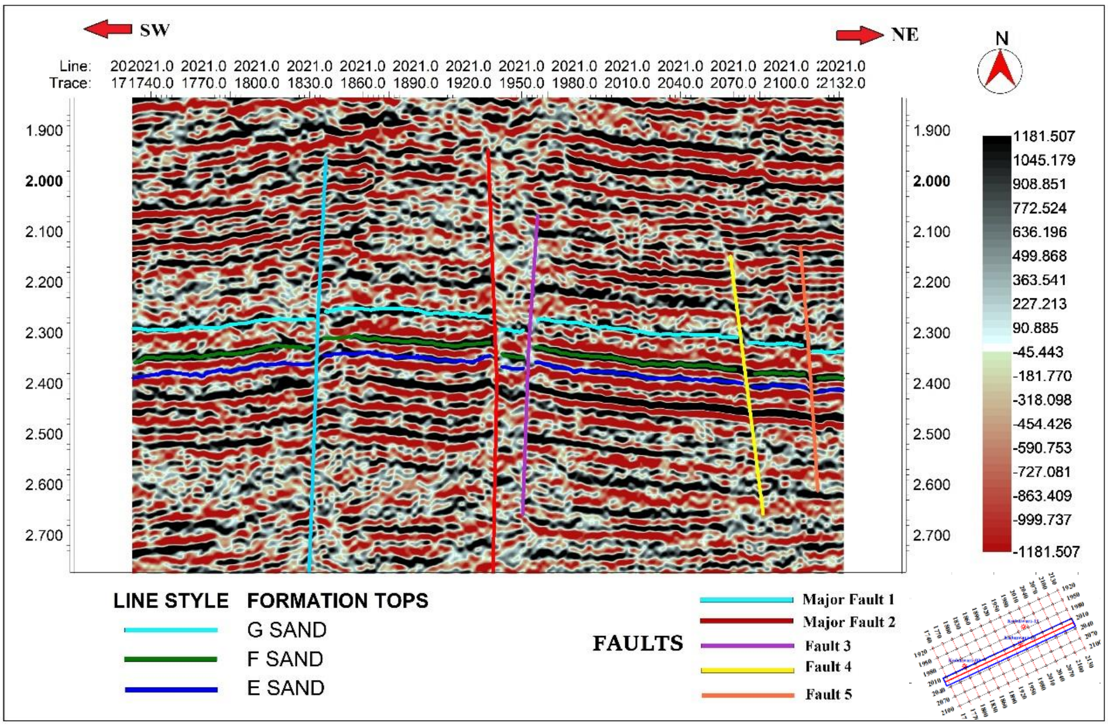

Figure 3.9 Interpreted seismic section depicting horizons and faults at Inline 2021.

3.5 Contour Maps

The Contour maps also referred to as topographic maps, represent variations of geological characteristics in the three-dimensional surface like thickness, depth, time, porosity, and others across a specific area by employing two-dimensional contour lines that denote consistent or same values (Ahmad et al., 2021). These contour maps portray the structural relief of the formation, indicating any faulting, folding, and dip of the strata. Seismic interpretation results are typically presented in the form of maps. Mapping constitutes an integral aspect of data interpretation, with the seismic or contour map often serving as the final output of seismic exploration (Coffeen, 1984).

Contours are lines that connect points with equal values of time, elevation, or depth. The first step in seismic interpretation is the generation of time contour maps using Two-Way Travel Time (TWT) because seismic data is in the time domain (Davarpanah & Akhlaghi, 2017). Subsequently, these time sections are converted into depth sections by the application of a velocity function, resulting in the construction of depth contour maps. To create a contour map, the process involves generating a horizon grid using the Grid and Contour tool, upon which the contour lines are subsequently generated (Khan et al., 2016)

The spacing of contour lines indicates the steepness of the terrain. Contour lines that are closely spaced indicate steep slopes, whereas lines that are widely spread indicate gentle slopes or terrain (Ahmad et al., 2021). Another crucial aspect of a contour map is its scale, which represents the ratio between the distances depicted on the map and their corresponding distances on the actual ground. The sudden interruption or displacement of contour lines can sometimes suggest the presence of a fault in the subsurface. Structural highs often serve as areas where hydrocarbons tend to accumulate. These are readily identifiable by observing a series of concentric closed contours with decreasing time values toward the center.

3.6 Time & Depth Contour Map Preparation

A time contour map is a graphical representation that includes specific lines representing time values. These time values on the map indicate the actual duration it takes for seismic waves to travel from the source, penetrate the subsurface, and finally reach the receiver. In the context of a two-way time (TWT) contour map, it primarily reveals the highs and lows in the geological structure. On a TWT contour map, areas with smaller time values are referred to as "highs" because they correspond to shallower locations, while larger time values indicate deeper areas and are termed as "lows" (Hossain et al., 2021).

Depth contour maps provide information through depth values, making it simpler to identify the location of subsurface horizons. These maps also offer preliminary estimates of reservoir size and reveal details about structural closures. To convert time measurements to depth, velocity data is essential. I created velocity grids for each horizon to acquire this necessary velocity information. The "Extended Math" feature in KINGDOM 8.4 software facilitated the time-to-depth conversion using the formula:

$$S = V \times t/2.$$

Velocity information is given in Table 3.1.

Table 3.1: Velocity data for each horizon, for conversion of time to depth values.

Formation	G Sand	F Sand	E Sand
Velocity	2752.975	2806.806	2778.834

The TWT contour maps for the three horizons were created to visually represent the structural layout of the research area. Out of these E-sand and G-sand are the major reservoirs. Time and depth contour maps have been created and analyzed for the horizons mentioned below.

1. G-sand
2. F-sand
3. E-sand

The Kingdom software was utilized to generate all contour maps, employing the "Flex Gridding" algorithm for their creation.

- **Major interpretation of all contours**

In all contour maps of time & depth, the light-yellow color represents the lowest time and depth values, indicating shallower regions, while the blue color signifies the highest time and depth values, representing the deepest parts. As previously mentioned, polygons have been used to delineate and highlight five distinct faults. The faults identified within this formation are of a regional nature. Additionally, it was observed from the map that there was little or no horizontal displacement (fault heave) between the layers of strata. The major faults, MF1 and MF2, are dipping away from each other, creating a horst-like structure in this region. On the other hand, MF2 and F3 faults dip towards each other, forming a graben. F3 and F4 are once again dipping away from each other, creating another horst-like structure, and F4 and F5 dip in the same direction towards the southeast, indicating normal faults. The closures observed within this field are primarily dependent on faults. These fault-dependent closures play a crucial role in preventing the further migration of hydrocarbons within the field. Therefore, the contour map reveals the presence of normal faults forming horst and graben structures.

A scale of 1:100000 meters was utilized to create contour maps, with a rainbow color gradient indicating time values in seconds and depth values in meters. The identification of normal faults forming horst and graben structures on the contour maps provides evidence that the Kadanwari Block is underlain by extensional tectonics.

3.6.1 TWT Contour Map G Sand

The TWT contour map for the G Sand horizon was generated by combining the base map with fault polygons, shown in Figure 3.10. The horizons exhibit a trend extending from the northeast to the southwest. The contour interval was defined at 5 milliseconds or 0.005 seconds, effectively displaying variations in time across the range of 2.25 seconds to 2.335 seconds.

Upon analyzing the time contour map for the G Sand, a clear trend becomes apparent. Specifically, the region extending from the southwestern side towards the central area exhibits a shallowing pattern, with contour values decreasing gradually as one moves toward the central region. This shift in colors, ranging from red to yellow, signifies a transition from deeper to shallower regions. Conversely, on the northeastern side, the contour values are notably higher, indicating deeper areas. In the middle region, situated between Major Faults MF1 and MF2, the contour values significantly decrease, suggesting that this central region is the shallowest portion of the map. This area holds potential promise for hydrocarbon accumulation because hydrocarbons tend to accumulate in regions where contour values are low, signifying relatively shallower depths. This indicates that this promising region holds potential as a future prospect.

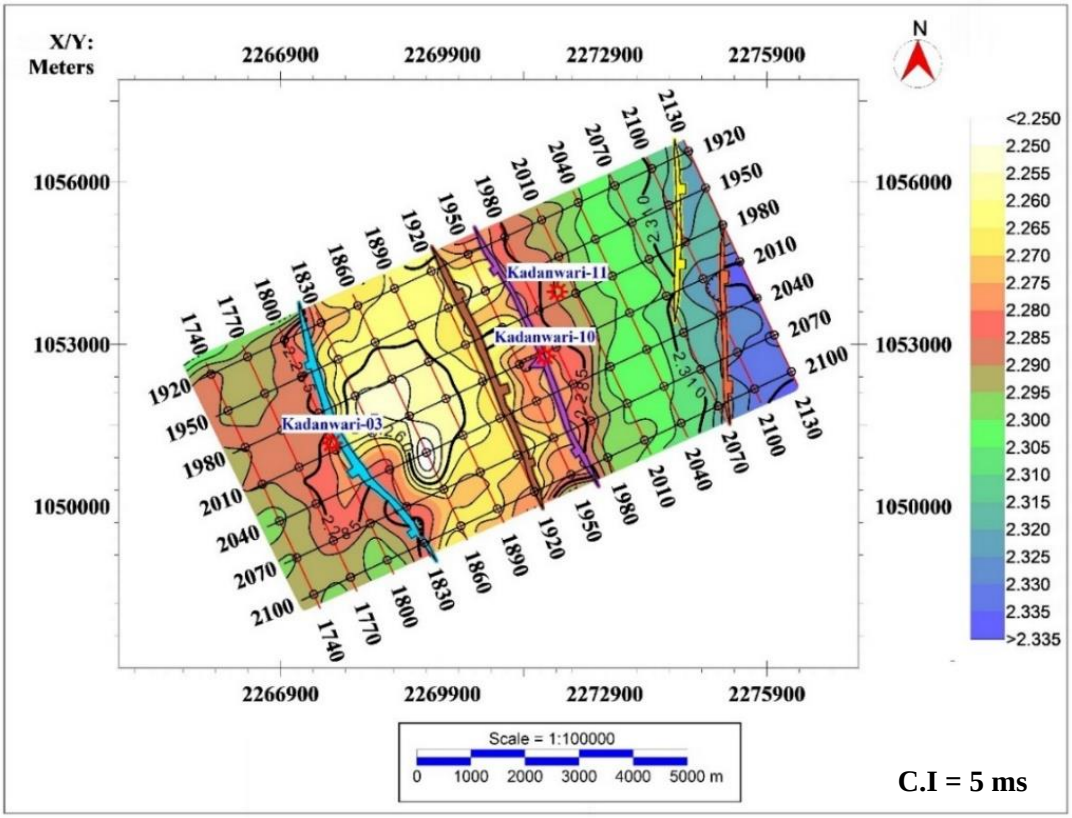

Figure 3.10 TWT contour map of G sand, exhibiting horst and graben structures.

3.6.2 Depth Contour Map G Sand

A depth structure contour map for G Sand was generated employing a velocity model, as depicted in Figure 3.11. This map broadly reflects the structural configuration observed in the Time-Depth-Structure (TWT) contour map of G Sand. The G horizon is dipping from the northeast to the southwest. The contour interval, set at 5 meters, effectively showcases fluctuations in depth within the range of 3045 to 3160 meters.

A strong correlation was observed between the structural time map and the structural depth map of this G Sand. In the depth contour map of G sand, the regions that indicate shallower time intervals in TWT time also correspond to shallow depth areas, and conversely, the areas with higher depth values in the contour map align with higher TWT time values. Therefore, the contour map reveals the presence of normal faults forming horst and graben structures.

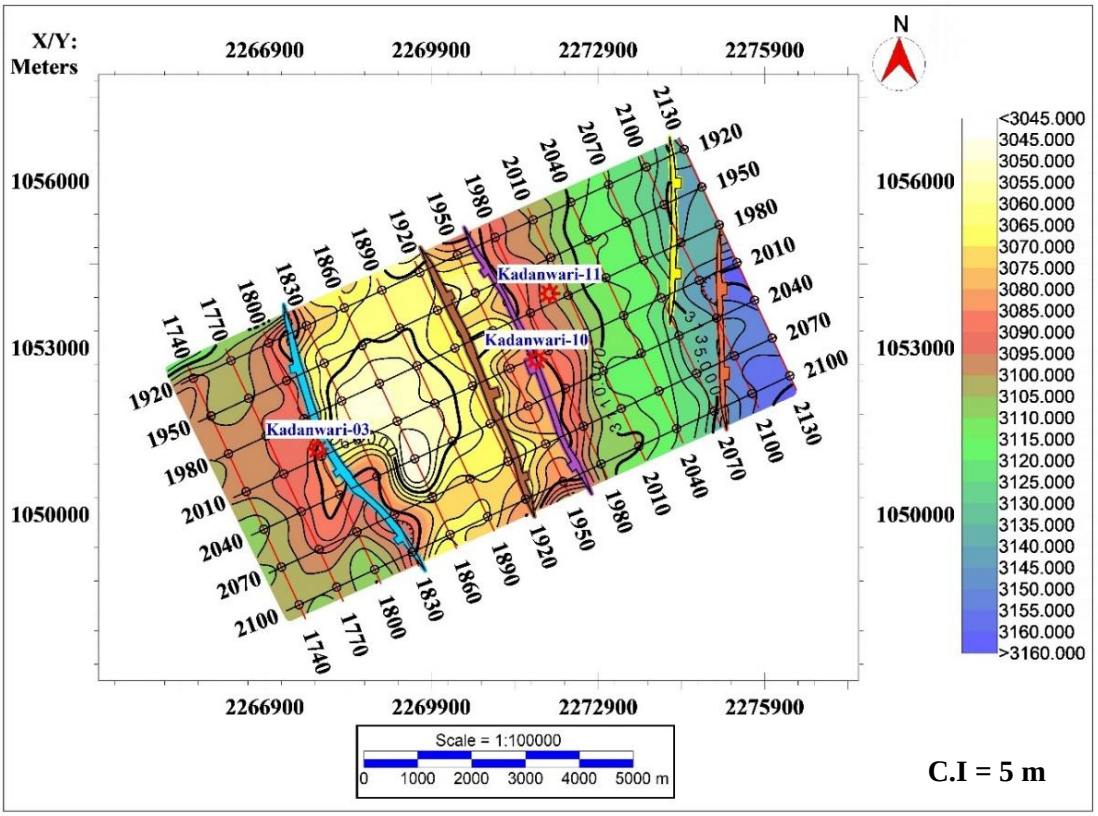

Figure 3.11 Depth contour map of G sand, exhibiting horst and graben structures.

3.6.3 TWT Contour Map F Sand

The contour map for the F Sand horizon was created by merging the base map with fault polygons, as illustrated in Figure 3.12. These horizons display a pattern that extends from the northeast to the southwest. The contour interval was set at 5 milliseconds, equivalent to 0.005 seconds, providing a clear representation of time variations ranging from 2.235 seconds to 2.39 seconds.

Upon analyzing the time contour map for the F Sand, a clear trend becomes apparent. Specifically, the region extending from the southwestern side towards the central area exhibits a shallowing pattern, with contour values decreasing gradually as one moves toward the central region. This shift in colors, ranging from red to yellow, signifies a transition from deeper to shallower regions. Conversely, on the northeastern side, the contour values are notably higher, indicating deeper areas. In the middle region, situated between Major Faults MF1 and MF2, the contour values significantly decrease, suggesting that this central region is the shallowest portion of the map. This area holds potential promise for hydrocarbon accumulation because hydrocarbons tend to accumulate in regions where contour values are low, signifying relatively shallower depths. This indicates that this promising region holds potential as a future prospect. The similarity in the trend of Fault F3 and the TWT (Two-Way Travel Time) F Sand contour indicates that there is a correlation between the fault trend and the contour. This correlation suggests that normal faults are likely present, forming horst and graben structures.

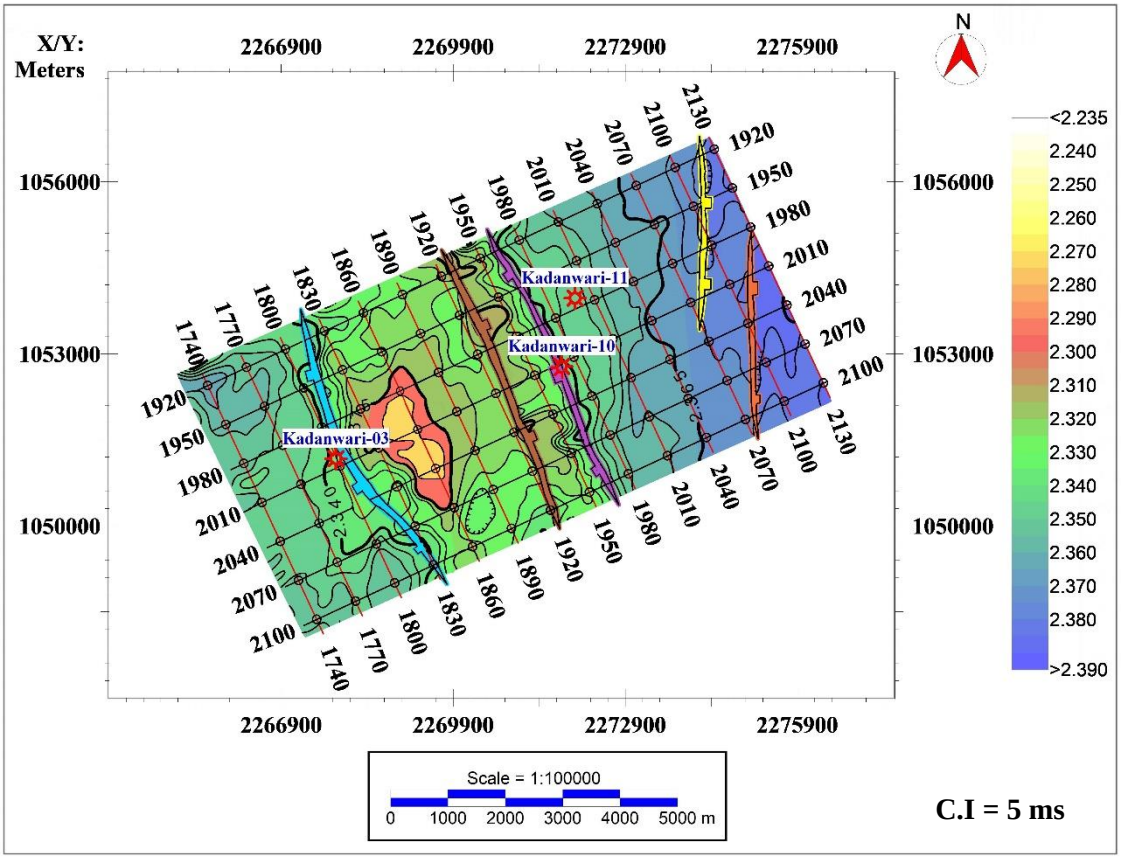

Figure 3.12 TWT contour map of F sand, exhibiting horst and graben structures.

3.6.4 Depth Contour Map F Sand

A contour map depicting the depth structure of F Sand was created using a velocity model, as illustrated in Figure 3.13. This map generally captures the structural pattern observed in the Time-Depth-Structure (TWT) contour map of F Sand. The horizon exhibits a consistent direction, stretching from the northeast to the southwest. With a contour interval of 5 meters, it effectively highlights variations in depth ranging from 3132 to 3316 meters.

A strong correlation was observed between the structural time map and the structural depth map of this F Sand. In the depth contour map of F sand, the regions that indicate shallower time intervals in TWT time also correspond to shallow depth areas, and conversely, the areas with higher depth values in the contour map align with higher

TWT time. Therefore, the contour map reveals the presence of normal faults forming horst and graben structures.

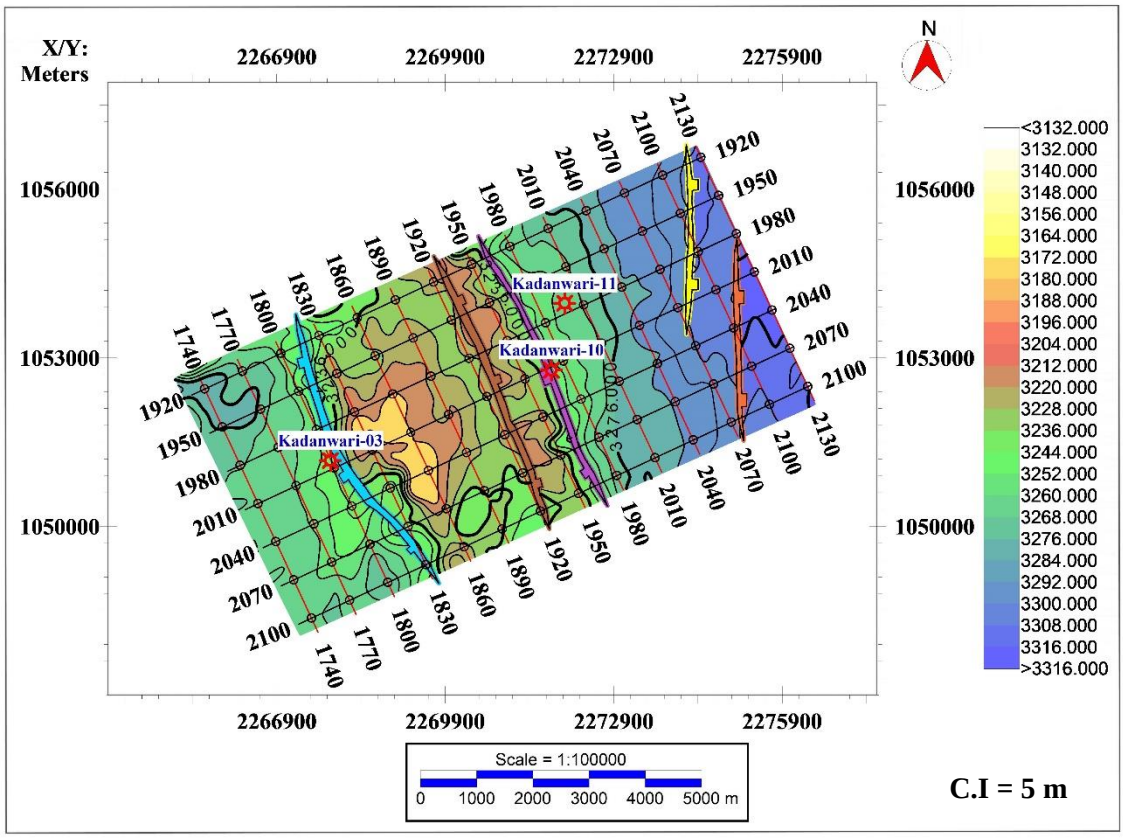

Figure 3.13 Depth contour map of F sand, exhibiting horst and graben structures.

3.6.5 TWT Contour Map of E Sand

The contour map for the E Sand horizon using TWT (Two-Way Travel Time) was created by merging the base map with fault polygons, as depicted in Figure 3.14. The E horizon exhibits a dip from the northeast to the southwest direction. The contour lines are spaced at intervals of 5 milliseconds or 0.005 seconds, effectively representing time variations within the range of 2.335 seconds to 2.415 seconds.

Upon analyzing the time contour map for the E Sand, a clear trend becomes apparent. Specifically, the region extending from the southwestern side towards the central area exhibits a shallowing pattern, with contour values decreasing gradually as

one moves toward the central region. This shift in colors, ranging from red to yellow, signifies a transition from deeper to shallower regions. Conversely, on the northeastern side, the contour values are notably higher, indicating deeper areas. In the middle region, situated between Major Faults MF1 and MF2, the contour values significantly decrease, suggesting that this central region is the shallowest portion of the map. This area holds potential promise for hydrocarbon accumulation because hydrocarbons tend to accumulate in regions where contour values are low, signifying relatively shallower depths. This indicates that this promising region holds potential as a future prospect. The similarity in the trend of Fault F3 and the TWT (Two-Way Travel Time) E Sand contour indicates that there is a correlation between the fault trend and the contour. This correlation suggests that normal faults are likely present, forming horst and graben structures.

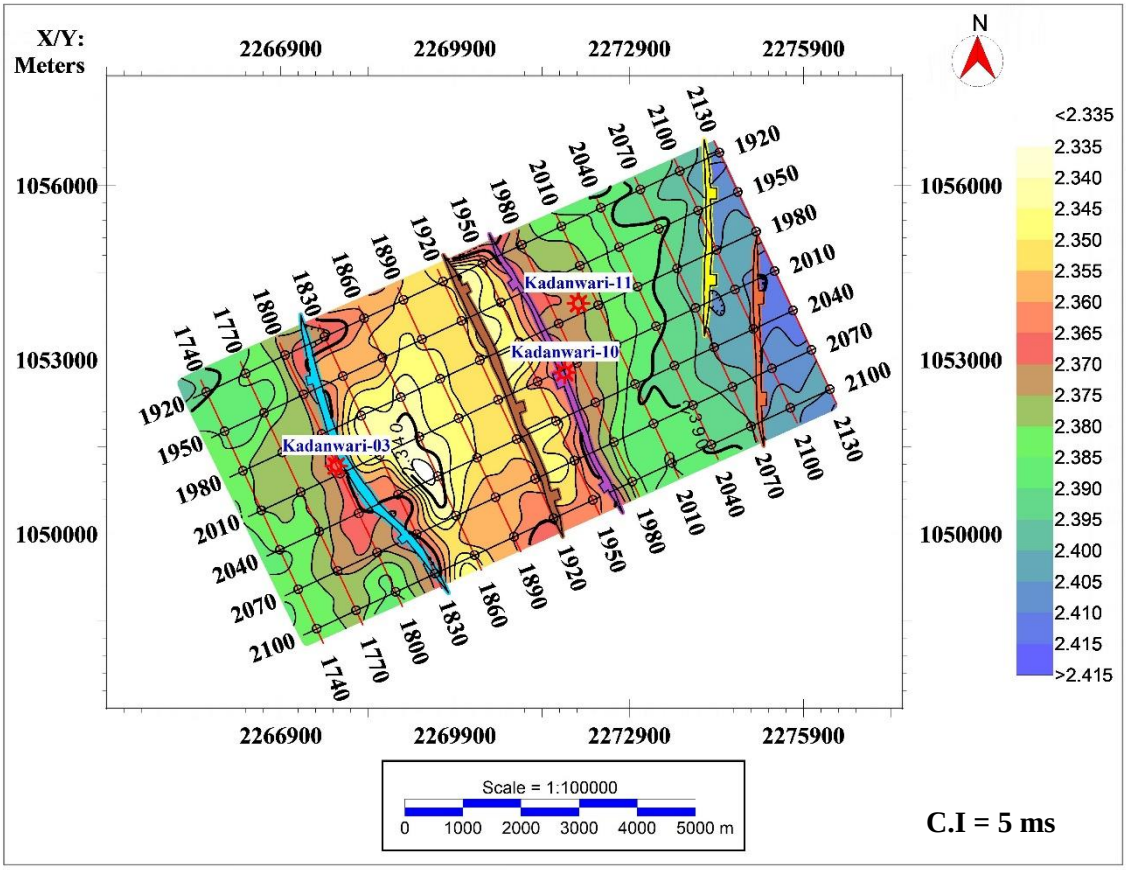

Figure 3.14 TWT contour map of E sand, exhibiting horst and graben structures.

3.6.6 Depth Contour Map of E Sand

A depth contour map for the E Sand formation was created using a velocity model, as shown in Figure 3.15. This map closely mirrors the structural pattern seen in the Time-Depth-Structure (TWT) contour map for the E Sand. The horizon exhibits a consistent pattern extending from the northeast to the southwest. By using a contour interval of 5 meters, it effectively highlights variations in depth ranging from 3295 to 3405 meters.

A strong correlation was observed between the structural time map and the structural depth map of this E Sand. In the depth contour map of E sand, the regions that indicate shallower time intervals in TWT time also correspond to shallow depth areas, and conversely, the areas with higher depth values in the contour map align with higher TWT time. Therefore, the contour map reveals the presence of normal faults forming horst and graben structures.

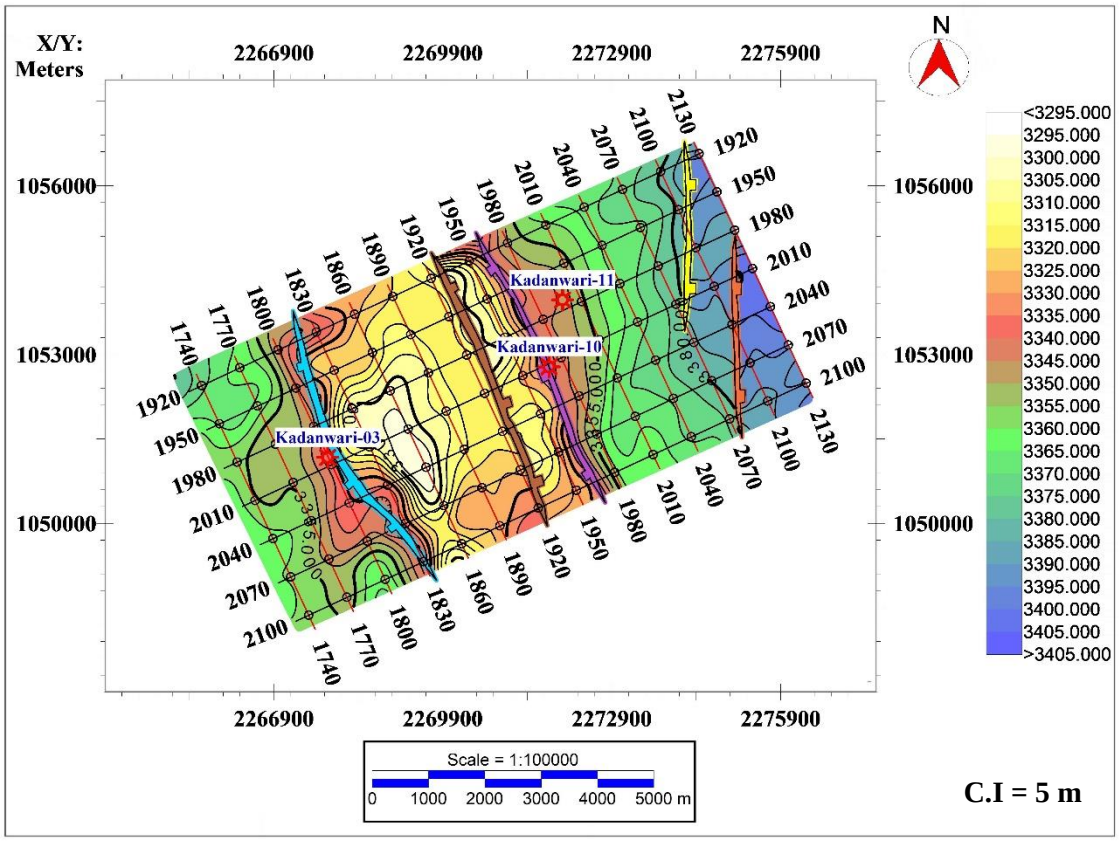

Figure 3.15 Depth contour map of E sand, exhibiting horst and graben structures.

CHAPTER 4

PETROPHYSICAL ANALYSIS

4.1 General Introduction

Petrophysical analysis examines reservoir rocks' physical and chemical properties and their interactions with fluids (Tiab and Donaldson, 2004). Petrophysical logs help in determining factors like rock type, porosity, pore structure, permeability, saturation of hydrocarbons, water saturation, etc. This data assists in the identification of productive zones, confirming the dimensions of hydrocarbon-rich layers in terms of depth and thickness, distinguishing between oil, gas, and water within a reservoir, and calculating reserve estimates (Rider, 2002).

Petro physicists utilize various well logs including resistivity, caliper, gamma ray (GR), sonic log (DT), neutron logs, and many others, to gather insights about the subsurface. Each well log holds its distinct significance and provides accurate and quantitative data regarding reservoir properties like permeability, porosity, net pay zone, shale volume, and fluid content (Senosy et al., 2020).

4.2 Methodological Framework

This chapter contains a petrophysical interpretation of the Kadanwari-10 and Kadanwari-11 wells, situated in the Kadanwari Gas Field. The interpretation of these wells was carried out using Gverse Geographix software. The workflow diagram for petrophysical analysis is presented in Figure 4.1 below.

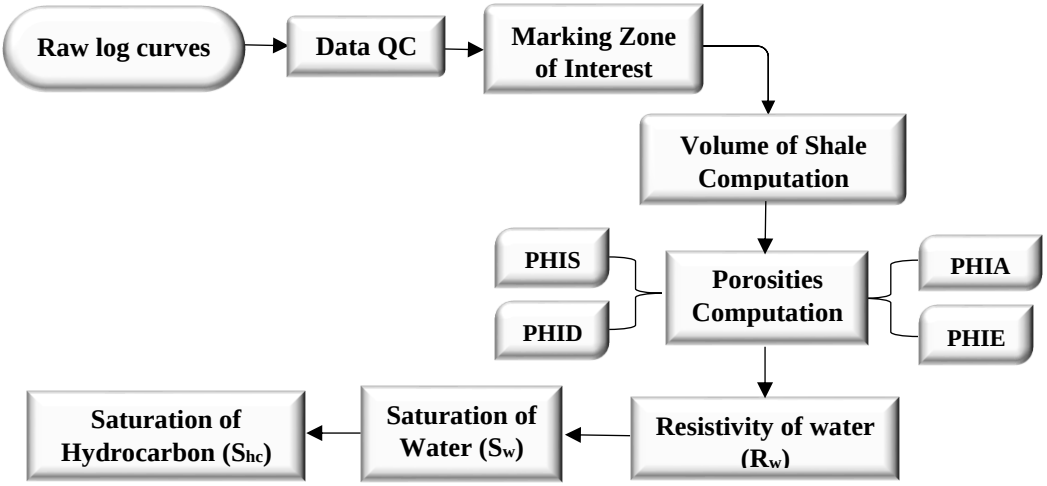

Figure 4.3 Workflow for evaluating petrophysical properties

Each step of the analysis is described in the following sub-sections.

4.3 Raw Log Curves

Raw log curves describe the underlying rock formations directly, indicating variations in lithology, fluid content, and other reservoir features. These curves form the basis for petrophysical analysis and interpretation. To extract important insights about the reservoir's potential for hydrocarbon exploration and production, raw log data is converted into relevant petrophysical parameters via a series of statistical transformations and quality control steps. The full set of wireline log data for wells Kadanwari-10 and Kadanwari-11 is available in LAS format. This dataset contains SP, Calliper, GR, Resistivity (Complete suite), Sonic, Neutron, Density, and PEF log raw curves.

4.4 Log Data Quality Check

In practical application, Well Logs often experience intrinsic issues such as noise, gaps, and spikes. A comprehensive quality assessment was performed on the logs at various depth levels to ensure the accuracy of the data they contain. To confirm the

reliability of all other logs, the diameter of the borehole was validated using a caliper log, since the values of these logs cannot be trusted in washout zones, requiring alternate procedures. If the logs fail to provide accurate information, subsequent calculations will yield errors, resulting in an inaccurate formation evaluation. This inaccuracy can lead to improper drilling and production plans, ultimately causing financial losses and wasted productive time. The quality control of these logs is of utmost importance because the precision of the logs directly impacts the accuracy of petrophysical analyses.

4.5 Marking Zone of Interest

After completing a quality check, log curves have been adjusted to standard scales and units. The process of formation evaluation involved identifying and marking the significant zones of interest that have the potential to produce hydrocarbons based on the interpretation of multiple log responses. In my research, the targeted formations are G, F, and E Sands of Lower Goru formations.

The criteria used to designate zones of interest are as follows:

1. Starting with an examination of gamma-ray response, which gives a clear indication of lithology. The gamma-ray log responds to naturally occurring radioactive minerals like Uranium, Thorium, and Potassium. Shales typically have higher concentrations of these radioactive materials compared to sandstones and limestone. If the gamma ray log curve shifts towards higher values on the log scale, it indicates the presence of shale beds. Conversely, lower gamma ray values signal clean lithology, which characterizes an outstanding reservoir (Ali et al., 2019).
2. Next, it is essential to assess the borehole conditions by plotting the bit size scale in the lithology track and examining the correlation with caliper readings. The caliper log measures the diameter of the borehole at various depths. If the calliper reading surpasses the bit size, it suggests the presence of rugosity caused by caving or washouts in the borehole. Conversely, if the caliper reading is less than the bit size, it indicates the presence of a mud cake. If the caliper reading is close to the drill bit size, the borehole is in-gauge. Borehole instability can significantly

impact other log readings, potentially leading to errors in accurately estimating the reservoir's characteristics (Ali et al., 2019).

3. The next step is to examine the resistivity values. When the MSF L (Micro Spherically Focused Log) displays higher resistivity than the LLD (Laterolog Deep), it often suggests that drilling mud filtrate has infiltrated the formation, displacing the native fluids (hydrocarbons or formation water). This is particularly relevant in more porous formations where mud filtrate can readily displace the formation fluids. Conversely, if the LLD exhibits significantly higher resistivity in comparison to the MFSL, it strongly indicates the presence of hydrocarbons in the uninvaded zone. This is because hydrocarbons possess a higher resistivity than water, and the LLD measures the resistivity of the native formation (Ali et al., 2019).
4. The density log provides insights into the porosity of the formation. In the Neutron Porosity (NPHI) log, we examine the hydrogen index. In areas with water-bearing formations, both the density and neutron logs often yield similar porosity values, causing them to be closely aligned or even overlapping on the log plot. In hydrocarbon-rich zones, especially those containing gas, the neutron log typically records a higher porosity compared to the density log. This leads to a distinct "crossover" effect where the neutron curve shifts to the right of the density curve. Gas zones exhibit the most pronounced crossover due to their very low density and hydrogen index. Oil zones may also display some degree of separation between the curves, although not as pronounced as in gas zones.

Following the identification of zones of interest based on the criteria mentioned earlier, the next step involves the calculation of petrophysical parameters, which include determining the volume of shale, porosities, and water saturation, among others.

4.5.1 Rugosity and mud-cake Assessment

Rugosity and mud cake is calculated using the caliper log to assess the condition of the borehole. The calculation involves utilizing both the bit size (BS) and caliper log (CAL) with the following formula (Rider, 1986):

$$\text{Rugosity} = \text{Calliper (CAL)} - \text{BS}$$

Mud-cake = BS - Calliper (CAL)

Rugosity can significantly impact the reliability of the density log. When rugosity is pronounced, it suggests that the density log might be calibrated incorrectly because padded tools measure readings inaccurately. To validate the data, density correction is applied, and the reliability of the readings is assessed. If the corrected values remain unreliable, in such cases, density porosity might not be used, and porosity calculations via sonic measurements (PHIS) become the preferred option. Conversely, when rugosity is absent, it typically signifies more reliable data. These computation helps in understanding the irregularities or variations in the borehole's diameter, which can be essential for drilling and reservoir evaluation.

4.6 Volume of Shale Computation (Vsh)

The estimation of shale volume was derived using the gamma-ray log, which captures the emission of natural radioactivity from geological formations. Shales are commonly enriched in radioactive elements, resulting in higher gamma-ray values, whereas sands and carbonates exhibit lower readings. Utilizing the shale volume estimation aids in lithology analysis by distinguishing between reservoir and non-reservoir sections within the interval (Asquith and Gibson in 2004).

Equation (Asquith and Gibson, 2004) to compute the volume of shale from the gamma-ray log:

$$V_{\text{shale}} = \frac{\left(GR_{log} - GR_{min} \right)}{\left(GR_{max} - GR_{min} \right)}$$

4.6.1 Stieber Correction

The Stieber Correction is employed when determining shale volume in shaly sand formations using Gamma Ray (GR) logs. This correction is necessary to adjust for the natural gamma radiation emitted by clean sand, thus enabling a more accurate assessment of shale content. Its use is crucial for achieving precise evaluations of reservoirs and supporting hydrocarbon exploration (GeolOil, n.d.). By distinguishing the radioactive

impact of shale, it improves the effectiveness of petrophysical analyses and refines reservoir characterization. The formula for this correction (Thomas & Stieber, 1975), is as follows:

$$Vsh_{Stieber} = \frac{IGR}{3 - 2 \times IGR}$$

Once the volume of shale (Vshale) is estimated, the remaining portion is considered the net reservoir, often referred to as the clean part. The primary purpose of estimating Vshale is to distinguish between the dirty and clean components within the zone of interest.

The equation (Rider, 1986) used for calculating Vclean is as follows:

$$V_{Clean} = 1 - V_{Shl}$$

This equation subtracts the estimated volume of shale from 1, resulting in the volume of the clean, net reservoir.

4.7 Porosities Calculation

Porosity arises from various sources, including intergranular spaces, voids resulting from grain dissolution, and rock fractures. The symbol denoting porosity is "ϕ," and it can be expressed either as a percentage or in decimal form. Primary porosity forms between grains during the deposition process, but secondary porosity emerges as pore spaces expand due to fracturing and dissolution. Secondary porosity is predominantly observed in limestone.

4.7.1 Calculation of Density Porosity (PHID)

Density porosity provides insights into the density of a lithology. When density porosity yields a high value, it suggests that the material under examination is not very dense, as it contains pore spaces that could potentially house hydrocarbons. Bulk density and density porosity share an inverse relationship. An increase in bulk density typically results in a decrease in density porosity, and conversely, a decrease in bulk density often

corresponds to an increase in density porosity. This relationship underscores how the density porosity log can help discern variations in lithology and fluid content within subsurface formations.

Density porosity is typically calculated using a density log (Schlumberger, 1974). The formula for density-derived porosity (φ den) is provided as:

$$\varphi \text{ den } = \frac{(\rho_{ma} - \rho_b)}{(\rho_{ma} - \rho_f)}$$

Here's what each of these terms represents:

φ den: Density-derived porosity.

ρma: Matrix density of relevant lithology,

ρb: Formation bulk density.

ρf: Fluid density.

The laboratory-computed matrix density (ρma) in g/cm³ for some important lithologies is as follows:

Sandstone: 2.65 g/cm³

Limestone: 2.71 g/cm³

Dolomite: 2.8 g/cm³

4.7.2 Calculation of Sonic Porosity (PHIS)

A sonic log device comprises a transmitter that emits sound waves and a receiver that captures and records the compressional waves as they reach the receiver. This log provides a recording of time (t) versus depth, representing the interval transient time (Δt), which is the time it takes for a compressional wave to traverse one foot of the formation. Δt is inversely proportional to the velocity of the sound wave and is influenced by the lithology and porosity of the formation (Asquith and Gibson, 2004).

The formula for determining porosity from a sonic log is expressed by the following equation (Wyllie et al., 1958):

$$\emptyset s = \frac{(\Delta t_{log} - \Delta t_m)}{(\Delta t_f - \Delta t_m)}$$

Here, in the equation:

∅s represents the sonic-derived porosity.

Δt_{log} is the interval transient time of the formation.

Δt_m is the interval transient time of the matrix.

Δt_f is the interval transient time of the fluid.

4.7.3 Calculation of Neutron Porosity (PHIN)

A neutron porosity log determines the concentration of hydrogen ions in the formation by measuring the interactions between high-energy neutrons and atomic nuclei in the rock. The neutron porosity value is directly obtained from the neutron log, and this log corresponds to the density log.

4.7.4 Calculation of Average Porosity (PHIA)

The average porosity (Φavg or PHIA) is calculated by averaging the porosity values obtained from either density (Φden) or sonic (Φsonic) logs with the neutron porosity (Φneutron) as follows:

$$\varphi_{avg} = \frac{(\varphi_{den} + \varphi_N)}{2}$$

OR

$$\varphi_{avg} = \frac{(\varphi_S + \varphi_N)}{2}$$

4.7.5 Calculation of Effective Porosity (PHIE)

Effective porosity provides a measure of the porosity within interconnected pores. This calculation excludes the contribution of shale since shale-prone zones typically exhibit little to no effective porosity. Effective porosity is a crucial parameter for calculating water saturation. The effective porosity can be calculated using the following formula, assuming no caving (Djebbar and Donaldson, 2004).

$$\varphi_{eff} = \varphi_{avg} \times (1 - V_{Shl})$$

Here,

$\emptyset_{avg}$ = Average Porosity, $\emptyset_{eff}$ = Effective porosity

In the presence of wellbore caving, the above formula can be adjusted as follows:

compare Here,

$\emptyset_S$ = Sonic porosity

4.8 Resistivity of Water (R_w)

The Pickett plot method is a technique used to calculate the resistivity of water. It involves plotting deep resistivity (LLD) on the X-axis and porosity log (PHIA or PHIS) on the Y-axis, using the logarithmic form of the Archie equation. On this plot, saturation points (Sw) are represented as dots arranged along a straight line with a negative slope, typically denoted as "m." The lowest line on the plot corresponds to water zones, and the water resistivity can be estimated from a point on this line where Sw = 1.

Once the water line is established, other parallel lines with different Sw values can be drawn, assuming a constant "n," often taken as 2. Subsequently, data related to Sw can be plotted and analyzed. The Pickett plot figures for estimating water resistivity in wells, Kadanwari-10 (with a resistivity of 0.033 ohms) and Kadanwari-11 (with a resistivity of 0.046 ohms) are shown in Figures 4.2 and 4.3, respectively.

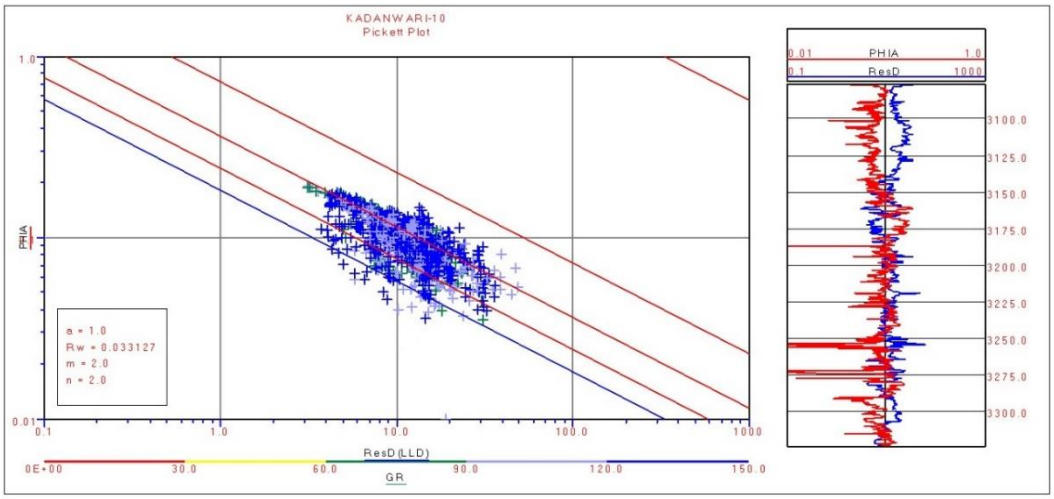

Figure 4.2 Pickett Plot of Kadanwari -10

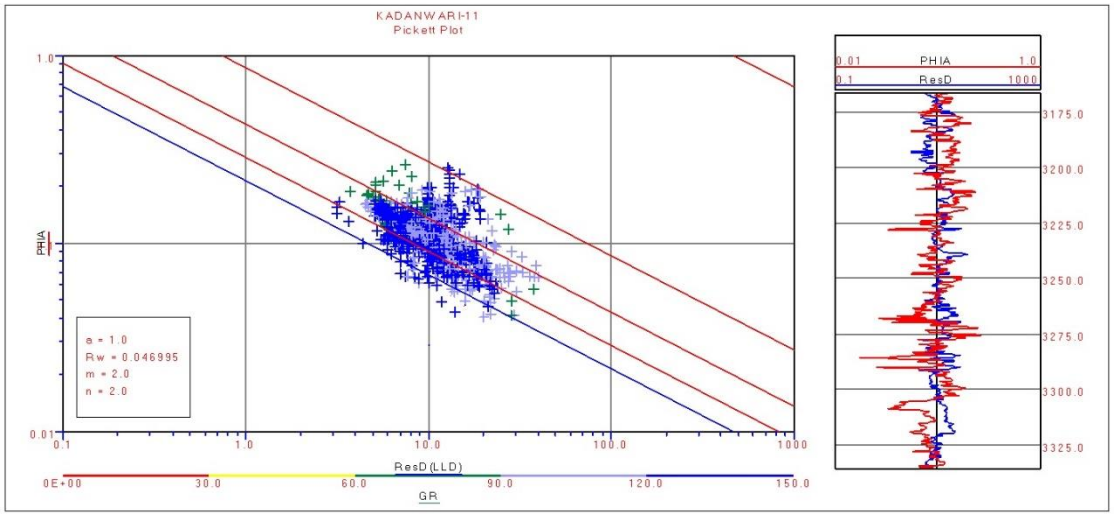

Figure 4.3 Pickett Plot of Kadanwari -11

4.9 Saturation of Water (S_w)

Water saturation provides information about the quantity of water present in the pore volume of rocks. However, it cannot definitively determine whether the pores in the formation contain hydrocarbons or water. Therefore, an assumption is made that these pores are filled with water. Water saturation is then calculated, and from this value, the amount of hydrocarbons present in the reservoir can be determined. Archie (Archie, 1942) derived a relationship for the calculation of formation water resistivity (Rw), which is as follows:

$$(S_w)_n = (\frac{a}{\varphi_m}) \times (\frac{R_w}{R_t})$$

Parameters are defined as:

a: The tortuosity factor, which is typically taken as 1.

m: The cementation exponent, often assumed to be 2.

n: The saturation exponent, is also frequently set to 2.

Rw: The resistivity of the formation water, which has been calculated previously.

Rt: The true resistivity of the formation (Laterolog (LLD) values).

4.10 Saturation of Hydrocarbon (S_{hc})

Hydrocarbon Saturation (S_{hc}) in Kadanwari-10 and Kadanwari-11 was calculated using the following equation:

$S_{hc} = 1 - S_w$ (Saturation of water)

4.11 Interpretation of Kadanwari-10

The objective of the petrophysical interpretation carried out on well Kadanwari-10 was to detect and delineate hydrocarbon-bearing zones. This analysis entailed the evaluation of multiple log curves to ascertain the petrophysical characteristics of the well.

4.11.1 G Sand

The G sand of Lower Goru Formation in the Kadanwari Gas Field is known to be productive, indicating potential zones of interest, as shown in Figure 4.4. G sand is situated between depths of 3076 meters and 3250 meters in Kadanwari-10. Two prospective zones, designated as Zone A and Zone B, have been identified within the G sand interval at the Kadanwari-10 location. These zones exhibit respective thicknesses of 10 meters and 11 meters, meeting the defined criteria for delineating zones of interest as

elaborated in section 4.5. Both these zones displayed consistent log readings, with crossovers in density and NPHI. LLD readings are on the right while MFSL appears on the left. The GR log is particularly useful in indicating potential shale regions. A cut-off value of 40% on the volume of shale log distinguishes between shale and sand, with values below this threshold indicating sand and values above indicating shale. Moreover, there's notable effective porosity, meeting the prerequisites for a reservoir, coupled with low water saturation and high hydrocarbon saturation. These observations led to the marking of the two zones (Figure 4.5).

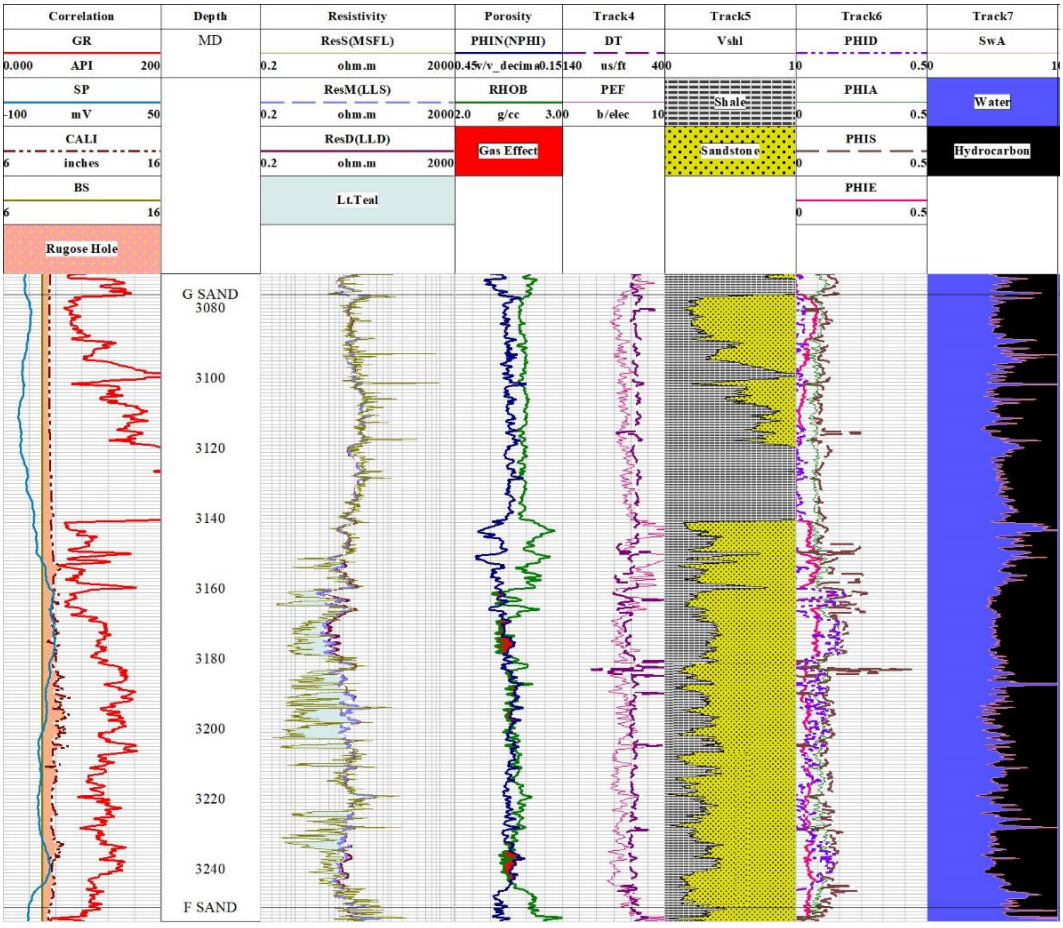

Figure 4.4 Petrophysical analysis and interpretation of the G Sand in Kadanwari-10**.**

A closer view of the zones of interest within the G Sand is depicted in Figure 4.5 below.

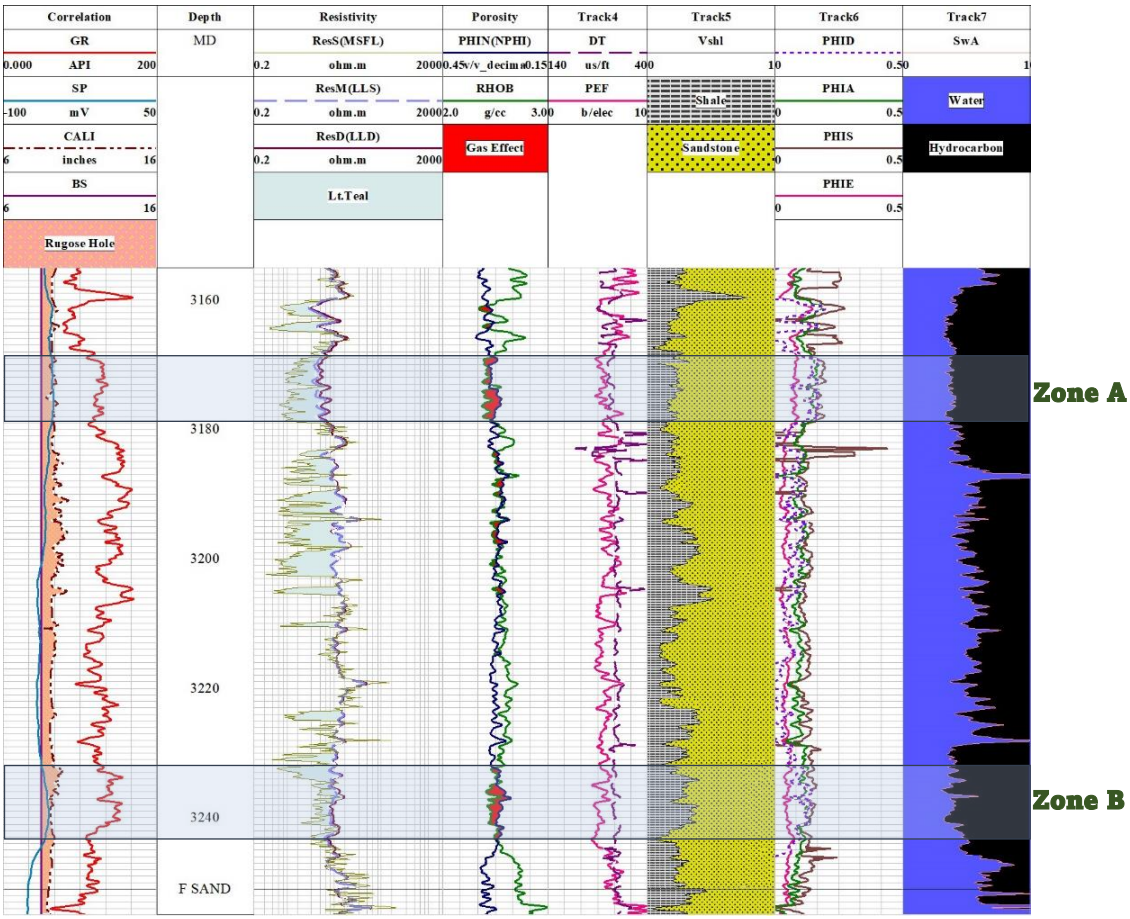

Figure 4.5 Closure view of zones of interest of G Sand

The petrophysical properties of zones of interest can be found in Table 4.1 below.

Table 4.1 Petrophysical parameters of the Reservoir zones within the G Sand Formation at Kadanwari-10 well.

Depth (m)	Thickness (m)	Vshl (%)	PHIA (%)	PHIE (%)	S_{wa} (%)	S_h (%)
Zone A (3169- 3179)	10	20	10	8	35	65
Zone B (3233- 3244)	11	25	9	7	39	61

4.11.2 F Sand

The F sand of Lower Goru Formation in Kadanwari Gas Field is recognized to exhibit productivity to a certain degree. Previous studies have highlighted that only a few beds, spanning 4-5 meters, are active producers in this sand. In this research, petrophysical analysis of the F Sand in Kadanwari-10 well identifies a potential zone of interest measuring 5 meters in thickness, from 3284m to 3289m, as depicted in Figure 4.6. The F Sand is situated at depths between 3250m and 3325m. Within the F Sand, a specific zone has been identified that meets the criteria for zones of interest, as elaborated in section 4.5. The F Sand displays significant variations in the resistivity log, which could be attributed to either the matrix or the fluids present in the formation.

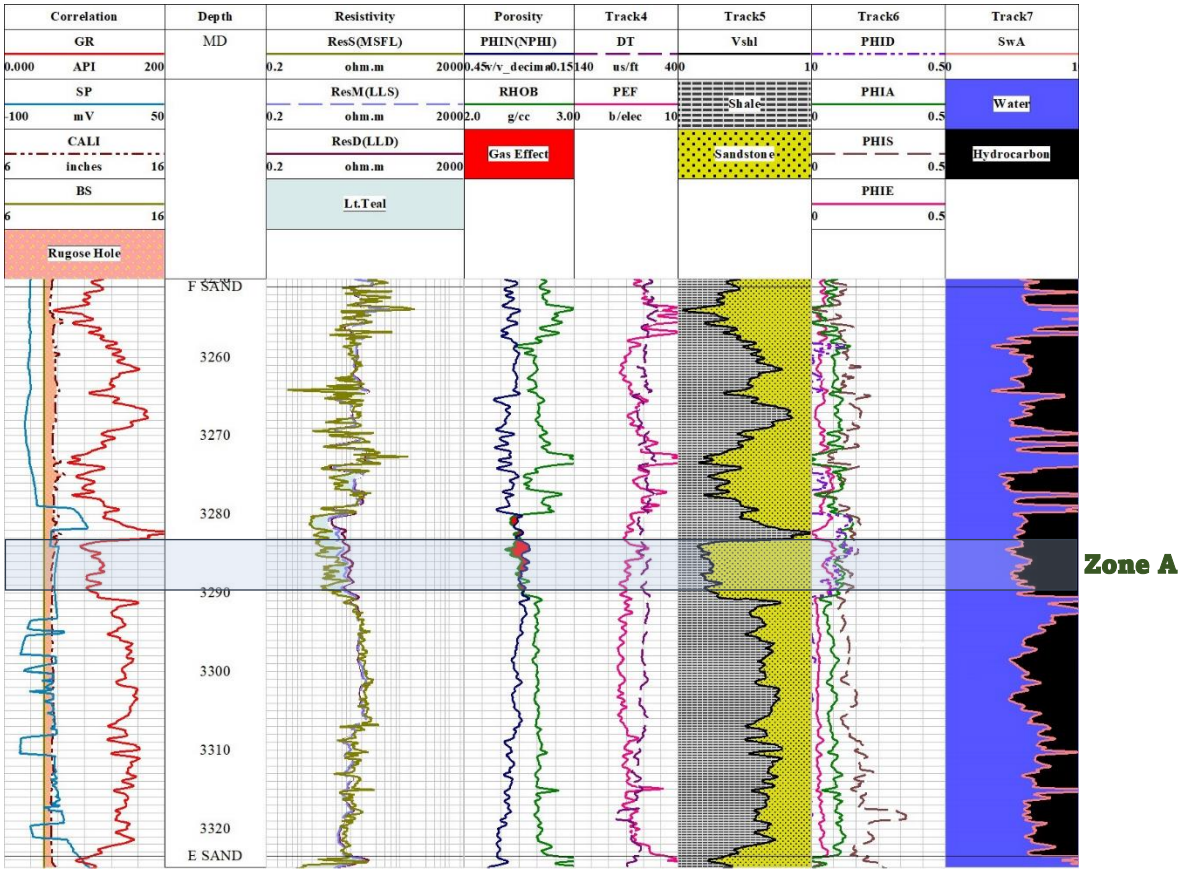

Figure 4.6 Petrophysical Interpretation and analysis of F Sand in Kadanwari -10

The petrophysical properties of zones of interest can be found in Table 4.2 below.

Table 4.2 Petrophysical parameters of the reservoir zones within the F Sand Formation at Kadanwari-10 well.

Depth (m)	Thickness (m)	Vshl (%)	PHIA (%)	PHIE (%)	S_{wa} (%)	S_h (%)
Zone A (3284- 3289)	5	23	9	7	41	59

4.11.3 E Sand

The E Sand of Lower Goru Formation in Kadanwari Gas Field is recognized for its productivity. In Kadanwari-10, the E sand is found between depths of 3323 meters and 3252 meters. Three distinct areas within the E sand in Kadanwari-10 have been identified as zones of interest based on the criteria detailed in section 4.5. Each of these zones exhibits consistent borehole conditions, with overlapping readings in density and NPHI, exhibiting crossover. The LLD readings are to the right, while MFSL is to the left. The GR log is particularly insightful for pinpointing potential shale areas. A threshold of 40% on the shale volume log differentiates between shale and sand; values beneath this cut-off indicate sand, while those above suggest shale. Additionally, there's a significant effective porosity that aligns with the requirements for a reservoir. This is further complemented by low water saturation and high hydrocarbon saturation. These factors contributed to the identification of the three zones in the E sand, as displayed in Figure 4.7.

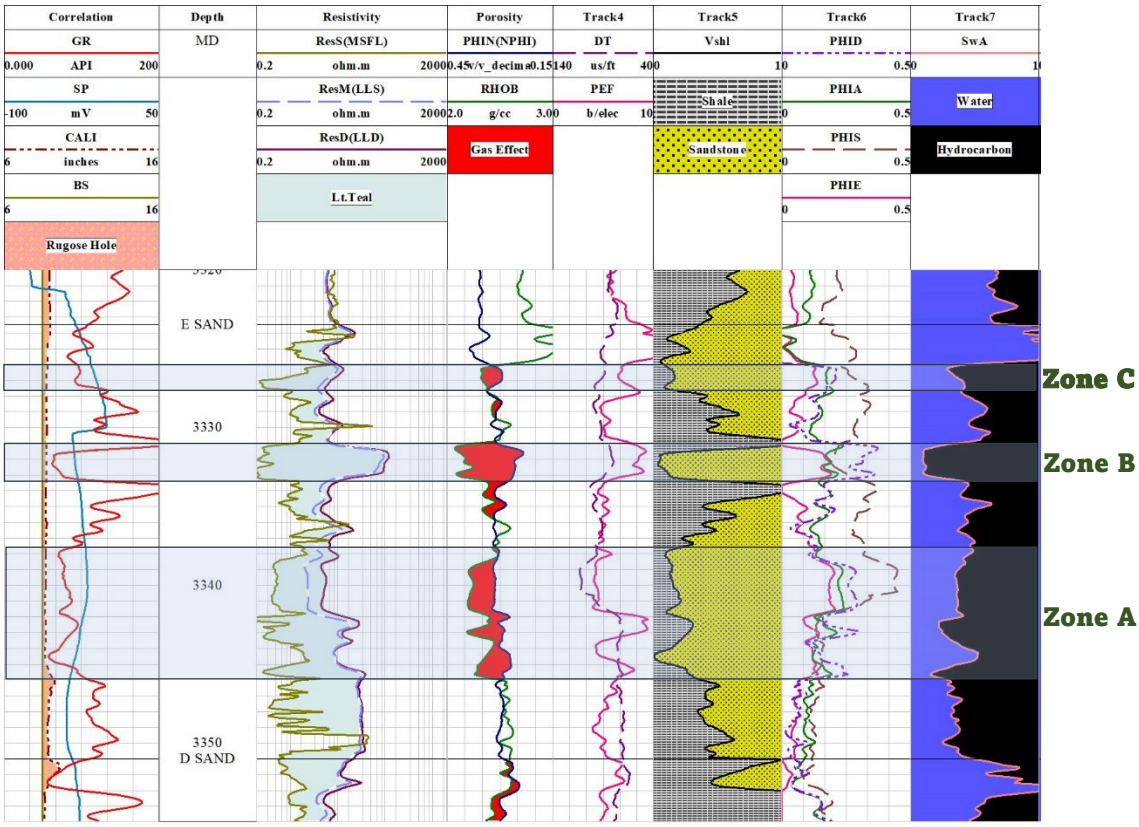

Figure 4.7 Petrophysical analysis and interpretation of the E Sand in Kadanwari-10**.**

The petrophysical properties of zones of interest can be found in Table 4.3 below.

Table 4.3 Petrophysical parameters of the reservoir zones within the E Sand Formation at Kadanwari-10 well.

Depth (m)	Thickness (m)	Vshl (%)	PHIA (%)	PHIE (%)	S_{wa} (%)	S_h (%)
Zone A (3337- 3346)	9	11	12	10	22	78
Zone B (3331- 3334)	3	8	11	9	7	93
Zone C (3326- 3328)	2	10	10	8	30	70

4.12 Interpretation of Kadanwari-11

The objective of the petrophysical interpretation carried out on well Kadanwari-10 was to detect and delineate hydrocarbon-bearing zones. Based on various log curves, conclusions about the petrophysical characteristics of the well have been drawn.

4.12.1 G Sand

The G sand in the Lower Goru Formation at the Kadanwari Gas Field is recognized for its productivity, pointing to potential areas of interest. In Kadanwari-11, this G sand lies between depths of 3165 meters and 3265 meters. Two distinct zones in this sand, each 9 and 10 meters thick, have been identified in Kadanwari-11 as meeting the criteria for zones of interest, as outlined in section 4.5. Consistent log readings with stable borehole conditions are evident in both zones, marked by crossovers in density and NPHI. LLD readings are on the right, while MFSL is on the left. The GR log stands out for its ability to identify possible shale areas. Using a 45% cut-off on the volume of shale log, it's possible to differentiate between shale (values above 45%) and sand (values below 45%). Additionally, there's a significant effective porosity, which fulfills the reservoir requirements, and this is complemented by low water saturation and elevated hydrocarbon saturation. These findings contributed to the demarcation of the two zones, as shown in Figure 4.8.

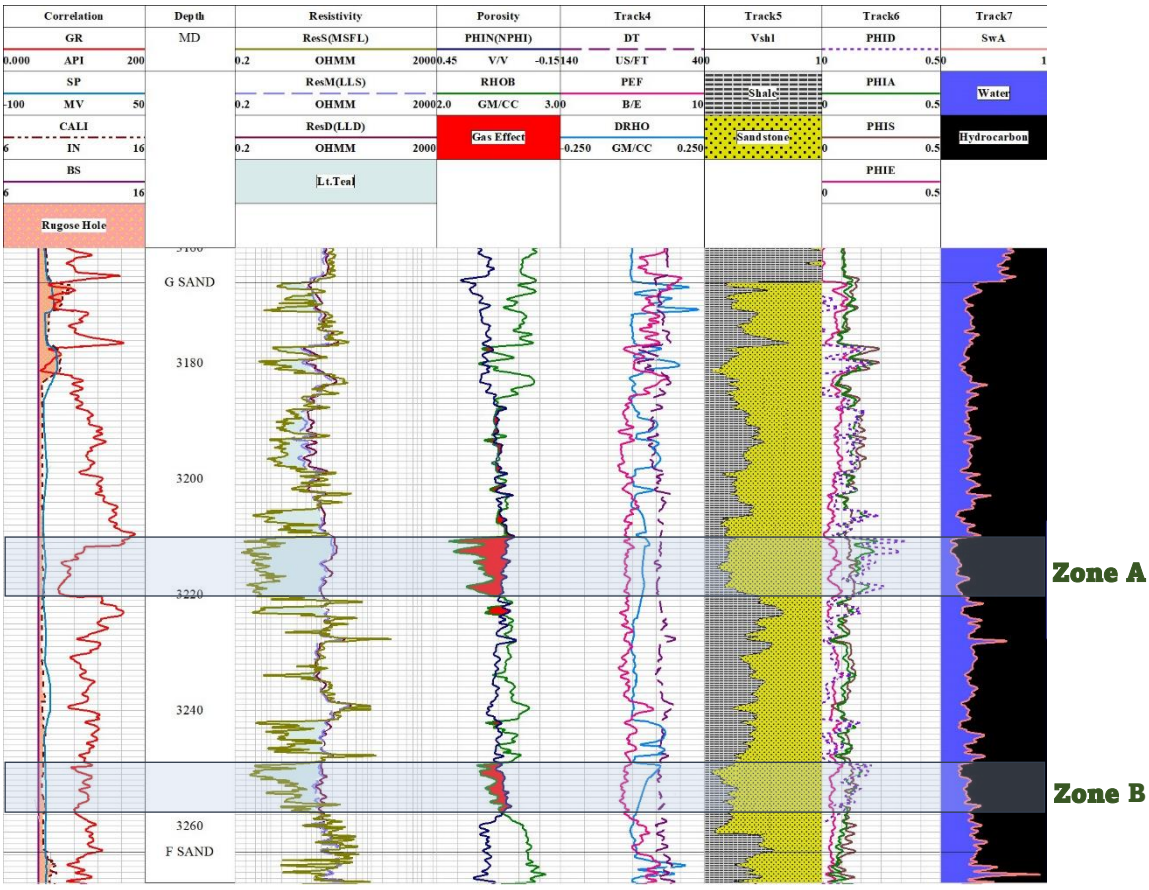

Figure 4.8 Petrophysical analysis and interpretation of the G Sand in Kadanwari-11**.**

The petrophysical properties of zones of interest can be found in Table 4.4 below.

Table 4.4: Petrophysical parameters of the reservoir zones within the G Sand Formation at Kadanwari-11 well

Depth (m)	Thickness (m)	Vshl (%)	PHIA (%)	PHIE (%)	S_{wa} (%)	S_h (%)
Zone A (3210- 3220)	10	17	13	11	9	91
Zone B (3249- 3258)	9	19	9	7	14	86

4.12.2 F Sand

The F sand of Lower Goru Formation in Kadanwari Gas field has limited productivity, with only a few beds spanning 4-5 meters showing production capabilities. The petrophysical analysis of the F Sand points to a potentially productive zone of 5 meters thick lying between depths of 3298 and 3303 meters, as depicted in Figure 4.9. This F Sand of Lower Goru Formation is generally located at depths ranging from 3265 to 3340 meters. Specifically, one zone within the F Sand in the Kadanwari-11 well meets the criteria for zones of interest, as elaborated in section 4.5. The F Sand Formation exhibits significant variations in resistivity logs, which could be attributed to either the formation matrix or the fluids present.

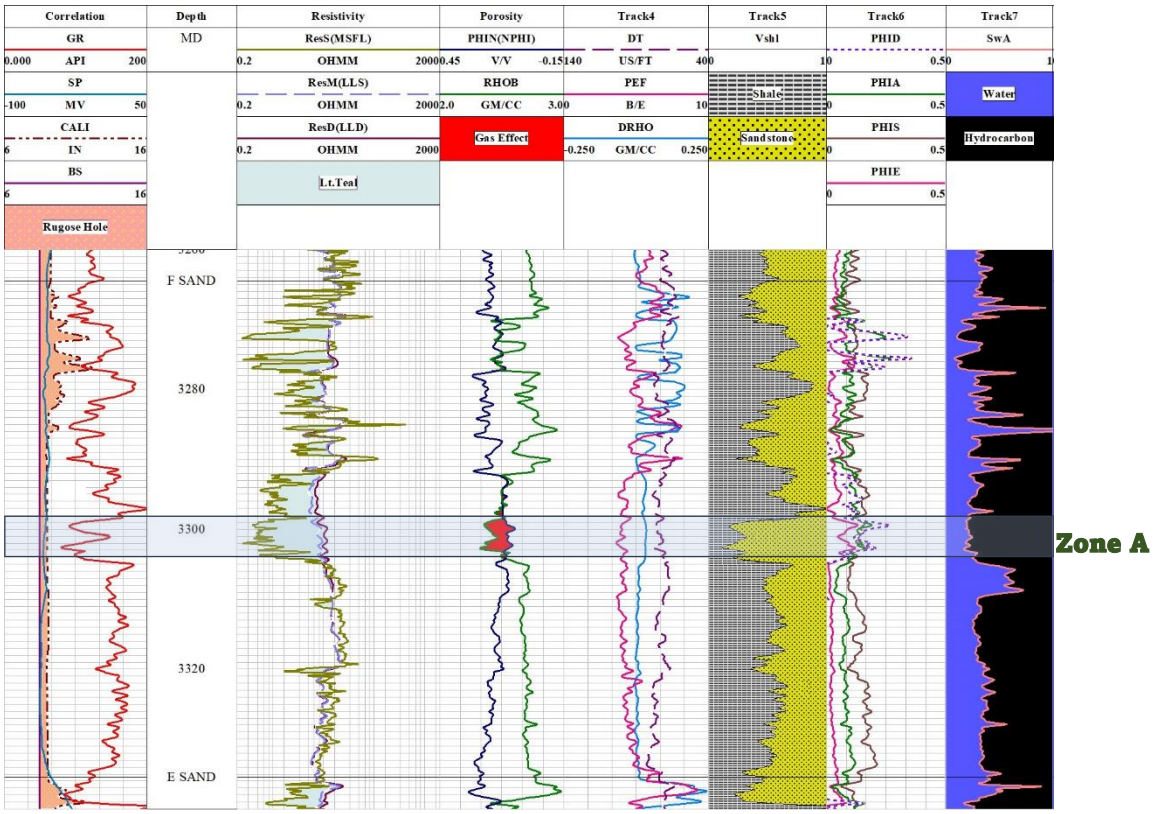

Figure 4.9 Petrophysical analysis and interpretation of the F Sand in Kadanwari-11**.**

The petrophysical properties of zones of interest can be found in Table 4.5 below.

Table 4.5: Petrophysical parameters of the reservoir zones within the F Sand Formation at Kadanwari-11 well

Depth (m)	Thickness (m)	Vshl (%)	PHIA (%)	PHIE (%)	S_{wa} (%)	S_h (%)
Zone A (3298- 3303)	5	25	7	6	21	79

4.12.3 E Sand

The productivity of the Lower Goru E Sand in the Kadanwari Gas field is well-known. In Kadanwari-11, this E Sand layer is located at depths ranging from 3330 meters and 3364 meters. Two distinct areas of 5 and 7 meters thick within the E sand in Kadanwari-11 have been identified as zones of interest based on the criteria of marking zone of interest outlined in section 4.5. Each of these zones exhibits stable borehole conditions, with overlapping readings in density and NPHI, exhibiting crossover. The LLD readings are to the right, while MFSL is to the left. The GR log is particularly insightful for pinpointing potential shale areas. A cutoff of 45% on the shale volume log differentiates between shale and sand; values beneath this cut-off indicate sand, while those above suggest shale. Additionally, there's a significant effective porosity that aligns with the requirements for a reservoir. This is further complemented by low water saturation and high hydrocarbon saturation. These factors contributed to the identification of the two zones in the E sand, as displayed in Figure 4.10.

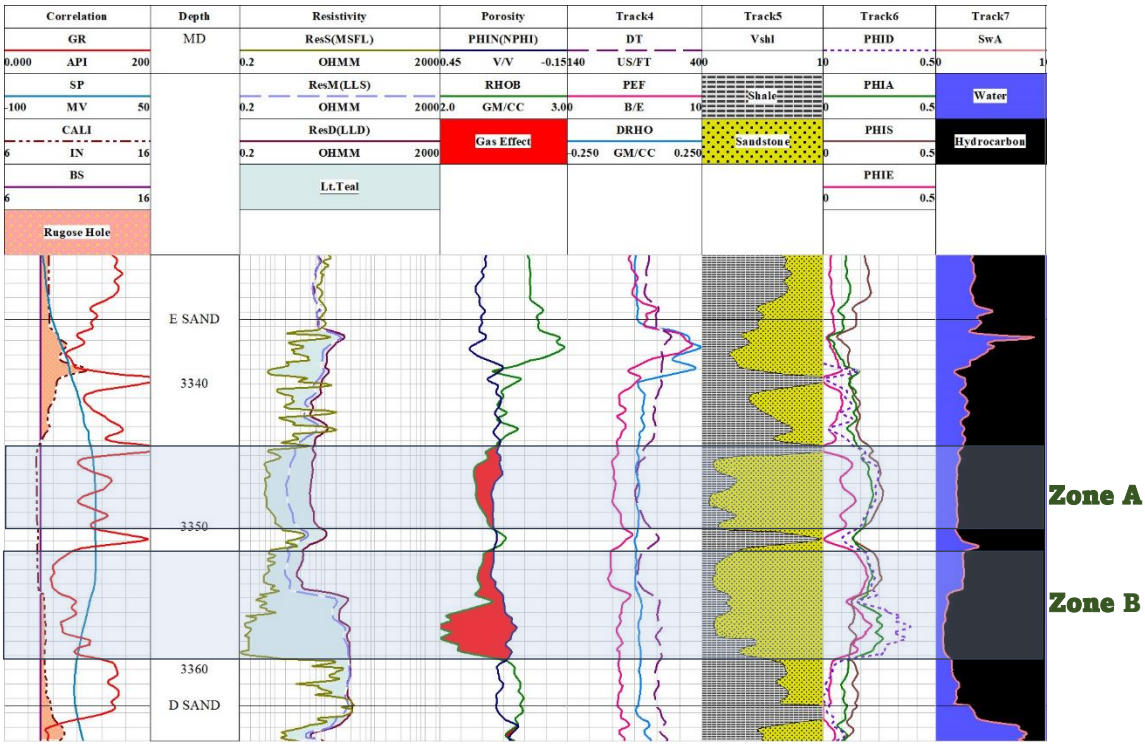

Figure 4.10 Petrophysical analysis and interpretation of the E Sand in Kadanwari-11**.**

The petrophysical properties of zones of interest of E Sand can be found in Table 4.6 below.

Table 4.6: Petrophysical parameters of the reservoir zones within the E Sand Formation at Kadanwari-11 well

Depth (m)	Thickness (m)	Vshl (%)	PHIA (%)	PHIE (%)	S_{wa} (%)	S_h (%)
Zone A (3345- 3350)	5	13	12	10	10	90
Zone B (3252- 3259)	7	15	14	12	7	93

CHAPTER 5

SEISMIC INVERSION

5.1 Seismic Inversion

Seismic inversion techniques are employed to create models that describe the characteristics of underground rocks and fluids, utilizing data from seismic surveys and well logs. When well data is unavailable, these properties can still be deduced solely from the seismic data. In the oil and gas sector, this technique is commonly employed to identify layers containing hydrocarbons beneath the earth's surface (Maurya & Sarkar, 2016).

Seismic data is produced via the process of forward modeling. It results from the convolution of the earth's reflectivity with a source wavelet. This convolution produces a trace with a limited bandwidth, which is governed by the seismic wavelet. The seismic data's band-limited characteristic means it lacks low frequencies, inhibiting the impedance trace from capturing the fundamental impedance or velocity structure essential for geological interpretation. Efforts to retrieve this resolution typically involve obtaining the reflectivity via a deconvolution process, which poses an inverse problem. Seismic inversion stems from inverse modeling (Zhang & Deng, 2018).

Seismic inversion methodologies can be broadly characterized into two main types: Pre-stack inversion and post-stack inversion. While post-stack seismic data solely yields P impedance because it's defined by the seismic amplitude R(0), pre-stack data gives both P and S acoustic impedance. Additionally, it provides derivatives such as Vp/Vs, Lambda-rho, and Mu-rho, which are vital for determining fluid and rock properties beneath the surface. The foundation of seismic inversion lies in a 1-D convolution model. In this model, seismic traces result from the convolution of the earth's reflectivity with a wavelet, influenced by noise (Barclay, 2008). In this study, I will be focusing on implementing post-stack inversion.

5.2 Post Stack Inversion

Post-stack inversion is a process employed in the geophysical industry to extract rock properties, such as impedance, from the reflectivity information in the seismic data. It doesn't need full aperture stacked data but uses only near-offset stack data to produce results that are both physically sound and geologically trustworthy. This inversion provides a rapid means to improve the fundamental stratigraphic interpretation of post-stack seismic information (Das et al., 2017).

Seismic data that has been stacked is used as the input for post-stack inversion. The stacking process helps in diminishing the influence of noise on the signal, ensuring that the true amplitude remains unaltered. Traces that originate from the common midpoint (CMP) are chosen and subsequently stacked at an incidence angle of zero. The seismogram produced from this depicts reflectivity at a standard incidence. Thus, when inversion is carried out on this type of seismic data, it's referred to as post-stack seismic inversion (Veeken & Da Silva, 2004).

The basic procedure involves transforming seismic amplitude data by employing model base algorithm, which is collected by summing traces (or "stacking"), into a model of subsurface properties. The process begins by generating an initial impedance model from well log data and seismic data or any available prior information. Then, using this model, synthetic seismic data is computed. The synthetic data is being matched to the actual seismic data, and the differences between them, known as the residuals, are quantified. Iterative inversion algorithms adjust the impedance model to minimize these residuals. This iterative procedure persists until a desirable alignment between the synthetic and actual seismic data is attained, or until predefined conditions are satisfied. The final impedance model provides valuable insights into the subsurface lithology and fluid content, aiding in exploration and production decisions.

The basic procedure of inversion is given in Figure 5.1.

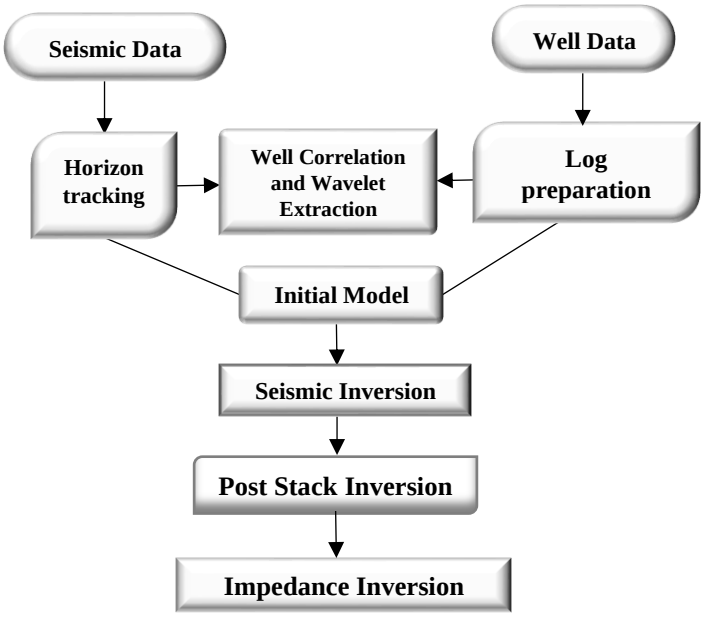

Figure 5.1 Basic post stack inversion workflow adopted in current study.

The post-stack inversion method offers several benefits, as outlined below:

i. Acoustic impedance pertains to the properties of layers, which makes interpreting stratigraphy more straightforward with impedance data than with regular seismic data.
ii. Reducing the effects of wavelets, lateral parts, and tuning improves subsurface layer clarity and resolution.
iii. The determination of acoustic impedance values allows for direct computation and comparison with well-log data, thereby establishing a connection to reservoir attributes.
iv. There's a correlation between porosity and acoustic impedance. Through geostatistical techniques, this impedance information can be translated into porosity details for the reservoir.
v. Specific reservoir zones can be accurately identified by utilizing acoustic impedance.

5.3 Basic Methodology

The main objective is to enhance the quality of underground imaging by minimizing the impact of wavelets that are present in seismic data (Margrave et al., 2001). This approach is based on the principle of convolution, which suggests that a seismic trace is created by combining the natural reflectivity of the earth with a wavelet and additional noise. Mathematically, this can be expressed as follows:

$$S = R \times W + N$$

Here,

S represents the seismic trace, R stands for the reflectivity of the earth, W denotes the wavelet, and N indicates noise. Assuming negligible noise, the equation simplifies to:

$$S = R \times W$$

To compute Earth's reflectivity (R), the formula used is:

$$R = \rho i + Vi + 1 + \rho i \times Vi \times \rho i + Vi + 1 - \rho i \times Vi$$

Here, ρ refers to density and V refers to the velocity of the p-wave. +1i+1 is the layer beneath layer i.

After noise filtering, the remaining seismic trace is then deconvolved by being multiplied with the inverse of the wavelet, thus isolating Earth's reflectivity. This isolated reflectivity can further be utilized to calculate acoustic impedance, achieved by altering the original formula as follows:

$$R = \rho i + Vi + 1 = \rho i \times Vi \times (1 - R1 + R)$$

The method does come with its challenges. A significant limitation is that band-limited wavelets are expected to eliminate the reflectivity's low-frequency component. Another central issue in inversion is filtering out noise and appropriately scaling the seismic data, as noted by (Russell & Hampson, 1991). To get more accurate results, the missing low-frequency component from seismic data is supplemented with logging data combined with stacked seismic data. A newer inversion technique is the model-based inversion, where an initial low-frequency model is continually adjusted to best match the seismic data The inversion process mainly involves preparing the data and feeding it into the software, syncing well logs with the seismic data, estimating wavelets, creating an

initial low-frequency model, and carrying out inversion analysis and the actual inversion (Karim et al., 2016).

5.4 Modal Based Inversion

In model-based inversion, an iterative process is employed to construct a geological model. The model is subsequently juxtaposed with the factual seismic data for evaluation. The outcomes of this comparison serve as a basis for enhancing the model during subsequent iterations, aiming to achieve a more accurate representation (Russel, 1991).

Model-based inversion proves to be effective in analyzing thin reservoirs because conventional seismic data is constrained by its band-limited nature, limiting both resolution and accuracy. Traditional direct inversion methods often fall short of meeting the stringent demands of the exploration industry. In contrast, model-based inversion incorporates both high and low-frequency elements, enabling a more detailed understanding of both stratigraphic and petrophysical reservoir properties (Russel, 1991).

The equation presented is for the Probabilistic Model-Based Seismic Inversion (PMBSI) as described by Hampson et al. (2005):

$$J = Weight_1 \times (S_t - W_t \times R_t) + Weight_2 \times (M - H \times R_t)$$

In this equation:

- J represents the objective function. The objective function essentially measures the difference between the observed seismic data and the data simulated using a given model. The goal in the inversion process is to minimize this difference, thus obtaining a model that fits the data best.
- St stands for the observed seismic data.
- Wt is the wavelet in the time domain.
- Rt refers to the reflectivity series in the time domain. Reflectivity series is a measure of how much seismic energy will be reflected at an interface between two layers with differing properties.

- M is the initial guess or starting model for impedance. This model can be derived from well logs, which are essentially recordings of the properties of rock layers encountered during drilling.
- H is the integration operator. When convolved with reflectivity Rt, it produces the acoustic impedance. Acoustic impedance is a measure of how much resistance a rock layer offers to the propagation of a seismic wave. It's a product of rock density and seismic velocity.

The equation essentially weighs the difference between observed seismic data and the synthetic (or predicted) seismic data produced by the model. The two terms in the equation allow for adjustments based on both the seismic data (1^{st} part of equation) and the initial guess of the impedance model (2^{nd} part of equation). By adjusting parameters and using optimization techniques, the best-fitting model (that which minimizes J) can be determined (Shakir et al., 2021).

5.5 Procedure of Modal Based Inversion

Seismic inversion, using a model-based approach, was executed on the seismic cube, with the reference well “Kadanwari-11" and “Kadanwari-10". The procedural steps for this inversion can be viewed in Figure 5.2. While data selection and horizon picking have been previously covered in the seismic interpretation chapter, the remaining steps will be elaborated upon here. Specifically, the G, F, and E Sands horizons were selected for seismic inversion. The Hampson and Russell software was employed to facilitate this inversion process.

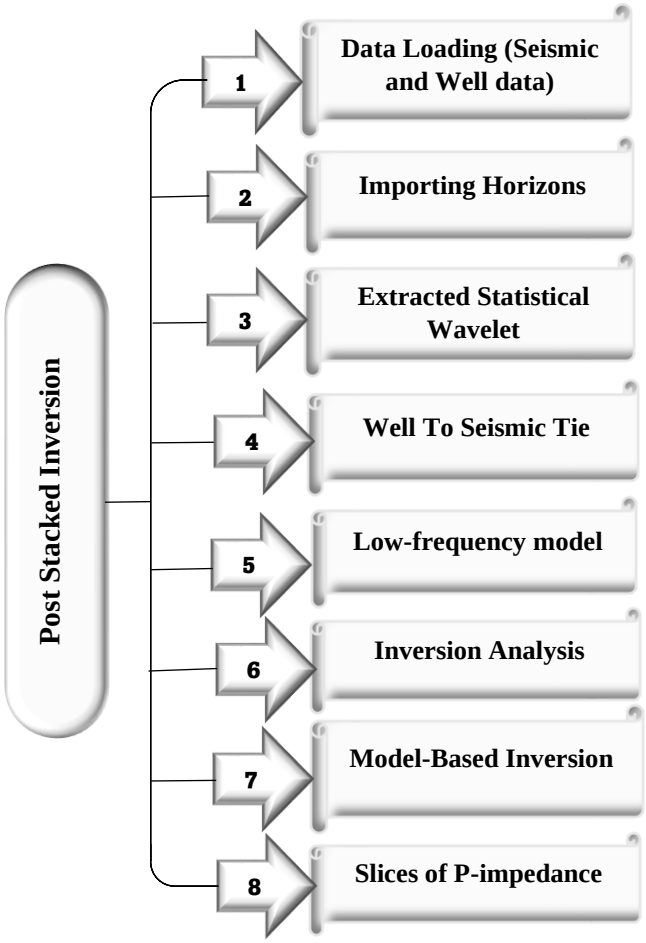

Figure 5.2 Adopted workflow for model-based Inversion.

5.5.1 Data Loading

The first step in the post-stack inversion process is to upload both seismic and well-related information into the Hampson & Russell Software. A 3D data block of the Kadanwari block is introduced into the software in SEG-Y format, along with interpreted are correlated with the seismic information to verify the exact well locations within the seismic volume. Loaded cube is shown in Figure 5.3.

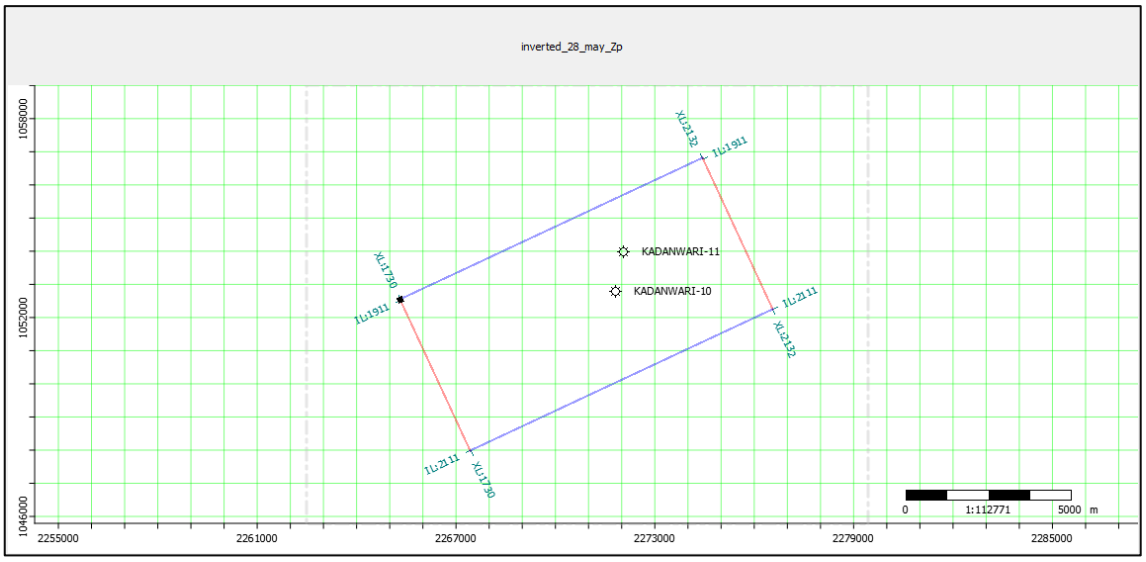

Figure 5.3 Configured the cube and well data in HRS software to initiate the inversion process.

5.5.2 Importing Horizons

The next step involves incorporating the specific horizons into the seismic section. These horizons, once interpreted, are sourced from the Kingdom software, and are formatted in time & amplitude. Reflections from three geological formations—G Sand, F Sand, and E Sand are fed into the corresponding software.

5.5.3 Extracted Statistical Wavelet

A reliable wavelet is the core of seismic inversion. To derive an acoustic impedance, a constant-phase wavelet is extracted from the seismic data and then convolved with the reflectivity series of the seismic section. This process facilitates the correlation between the inverted seismic reflectivity at the well location and the extracted reflectivity (Jain, 2013).

The wavelet varies across different subsurface locations. Factors such as geometrical spreading and attenuation complicate the wavelet's structure (Barclay et al., 2008). For this research, a statistical wavelet was employed. The extraction time window for this wavelet ranges from 2000 to 2500 ms, featuring a 200 ms wavelength and a taper

length of 25 ms. A zero-phase wavelet was utilized for the synthetic data. Figure 5.4 illustrates the extracted wavelet, highlighting its amplitude and phase spectrum.

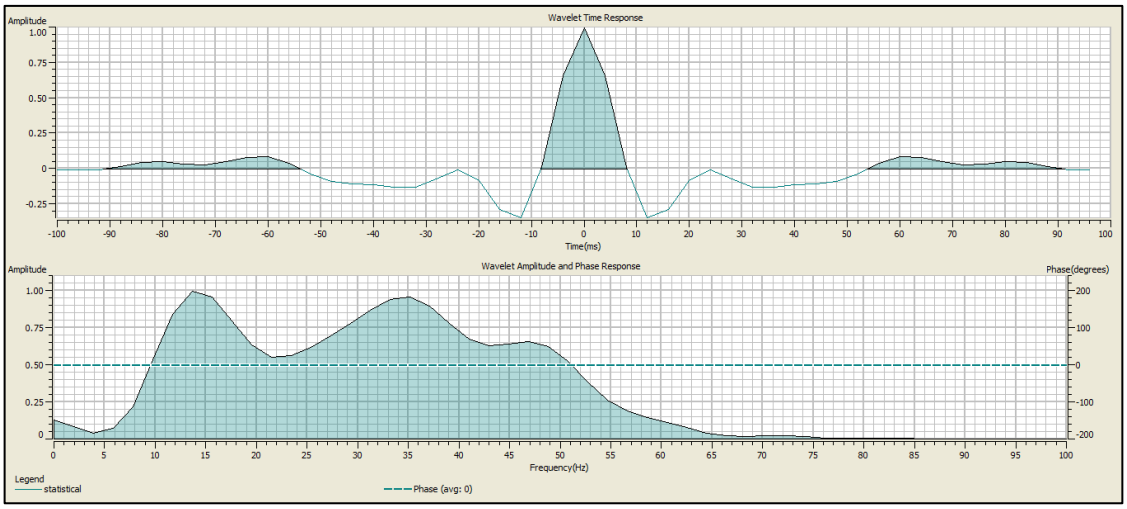

Figure 5.4 Statistical wavelet wavelet is extracted from the seismic data, highlighting its amplitude and phase spectrum.

To achieve accurate outcomes from seismic analysis and inversion, the wavelet must be in zero or minimal phase. The degree of phase shift in the input wavelet can significantly impact the inversion outcomes. A larger phase shift can lead to increased discrepancies in the derived impedance data (Jain, 2013).

5.5.4 Well-to-Seismic tie

In the process of well correlation, a synthetic trace is created to align with the existing seismic trace. This synthetic trace was adjusted – either elongated or compressed – to achieve the best fit with the actual seismic data. The integrity of the well-log data can have a substantial impact on the final display of the synthetic trace. The wells Kadanwari-10, and Kadanwari-11 were used to correlate well data with seismic data using synthetic traces generated from an extracted wavelet. This correlation is pivotal for seismic interpretation as it bridges the well and seismic data. As depicted in Figure 5.5, the correlation coefficient for Kadanwari-10 is approximately 74%. For Kadanwari-11, as

shown in Figure 5.6, the coefficient is 76%. The correlation was performed without rotating the phase.

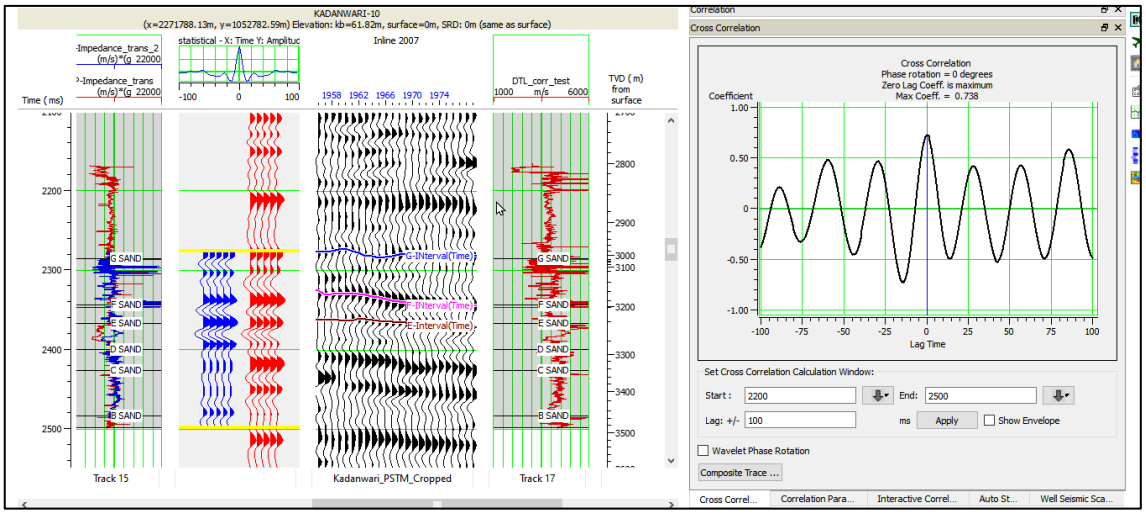

Figure 5.5 Seismic to well data correlation of Kadanwari-10

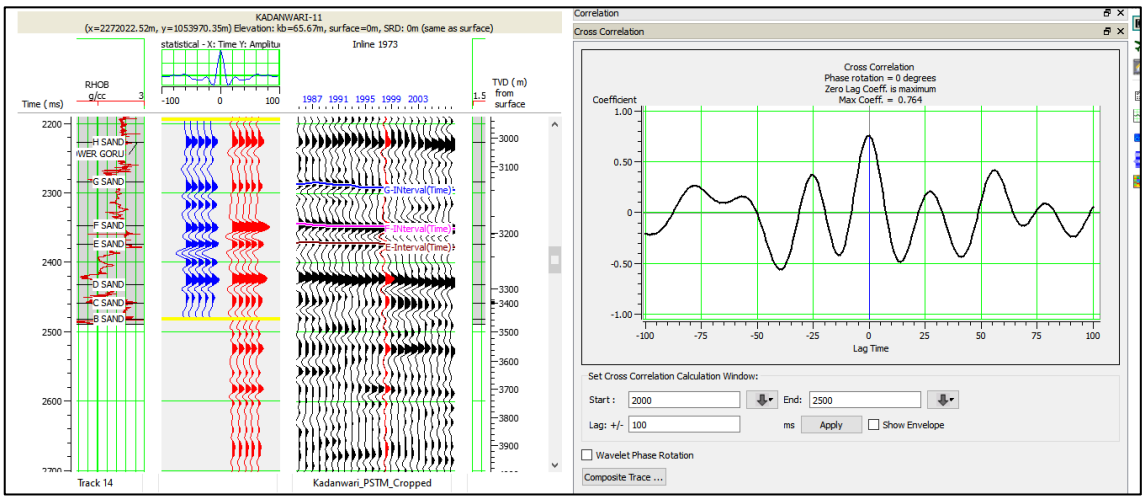

Figure 5.6 Seismic to well Data Correlation of Kadanwari-11

5.5.5 Low-frequency Model

The initial low-frequency model is often estimated using acoustic impedance, which can be categorized into two types: Relative Acoustic Impedance and Absolute

Acoustic Impedance. Relative Acoustic Impedance calculations don't necessitate the formation of a low-frequency model, making it useful for the qualitative assessment of seismic layers due to its focus on their relative attributes (Cooke and cant, 2010). On the other hand, Absolute Acoustic Impedance is an intrinsic property of geological layers and is pertinent to both qualitative and quantitative evaluations in seismic interpretation (Lee et al., 2013).

Seismic data typically lack low frequencies. To address this, a Low-Frequency Model (LFM) is created using a low-pass filter, which permits frequencies up to 10 Hz to pass while filtering out those above 15 Hz. Within the context of model-based inversion, the initial model was constructed using only the Zp log (created from density and sonic logs). The impedance (Zp) curve derived from both wells was applied to form a Low-Frequency Model, illustrated in Figures 5.7 and 5.8. This initial model was created for the time range between 2,000ms and 2,500ms, which encompasses the formation of interest. Subsequently, this model was then convolved with the seismic trace extracted from the seismic data.

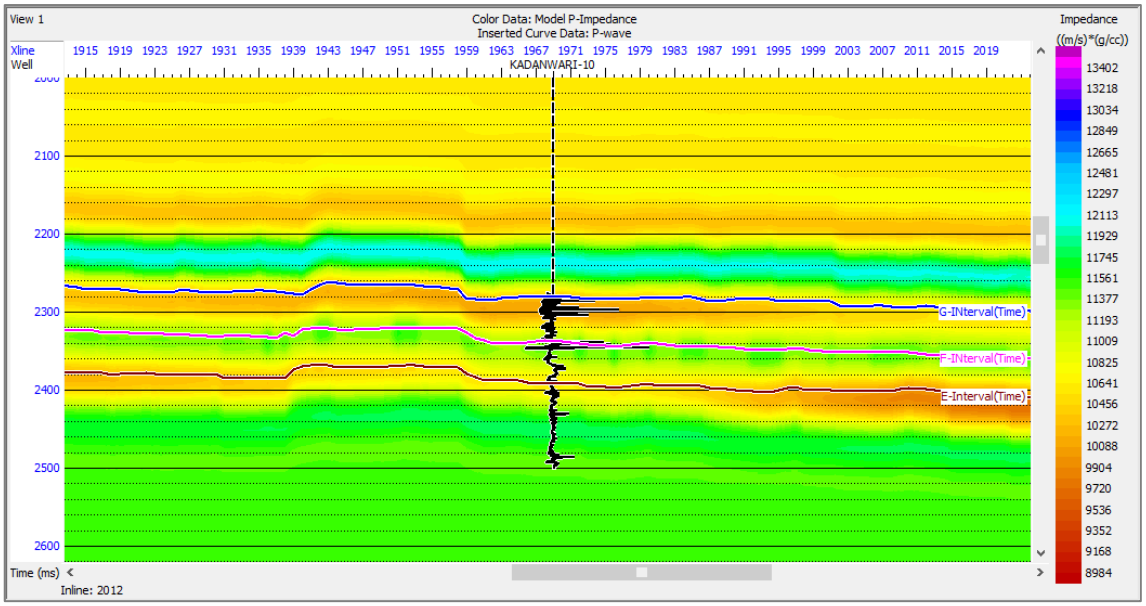

Figure 5.7 Low-frequency model of seismic data with well location of Kadanwari-10

In the figure, low impedance is represented by shades ranging from yellow to brown, signifying the presence of sand bodies. The figure illustrates that G and E sands exhibit comparatively lower P-impedance values ranging from 9536 to 10825 g/cm^3-m/s, in contrast to the F sand which shows a moderate range of impedance values spanning from 10825 to 11925 g/cm^3-m/s.

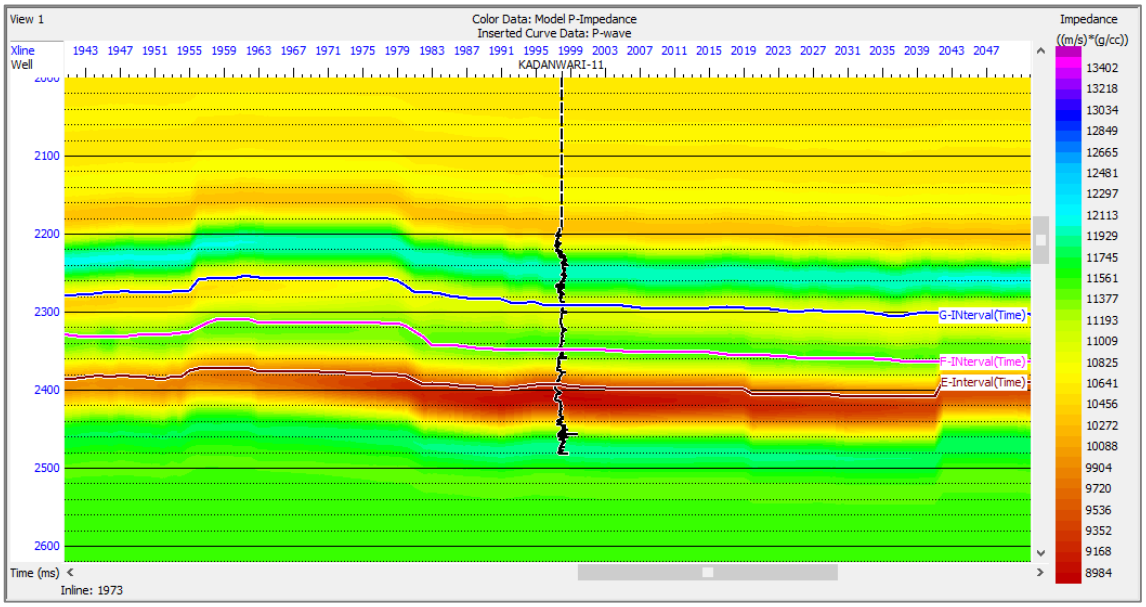

Figure 5.8 Low-frequency model of seismic data with well location of Kadanwari-11

Within the figure, the indication of low impedance is depicted through shades transitioning from yellow to brown, which highlights the presence of sand bodies. The visual representation illustrates that E sand displays notably lower P-impedance values, ranging from 8984 to 10825 g/cm3-m/s. On the other hand, G sand demonstrates impedance values that vary from lower to moderate, spanning the range of 10272 to 11009 g/cm3-m/s. In contrast, F sand exhibits a moderate range of impedance values from 10825 to 11925 g/cm3-m/s.

5.5.6 Inversion Analysis

In the process of model-based inversion, an initial low-frequency P-impedance model serves as the starting point. This model is then iteratively refined to achieve a close match between the seismic data and the synthetic trace.

The seismic cube data provided was examined for model-based inversion at the Kadanwari-10 and Kadanwari-11 well sites. Wavelets were extracted from a time window ranging from 2000 to 2500ms. The seismically extracted wavelet was adjusted by comparing the synthetic trace to the inverted trace at the well's location. Figures 5.9, and 5.10 depict the correlation between seismic traces (in black) and synthetic traces (in red). Kadanwari-10 displays a strong correlation coefficient of 99%, and a root mean square error of 0.0853 or 8% between the seismic and synthetic traces. The inversion analysis for Kadanwari-11 is similarly robust with a correlation coefficient of 99% and a root mean square error of 0.0416 or 4%.

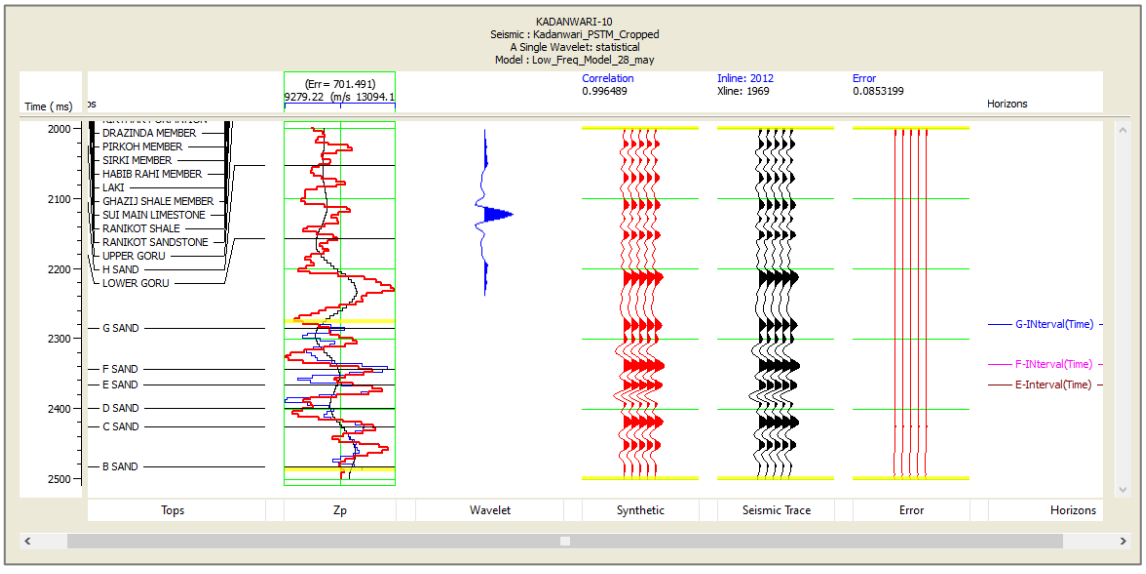

Figure 5.9 Model-based inversion analysis of Kadanwari-10

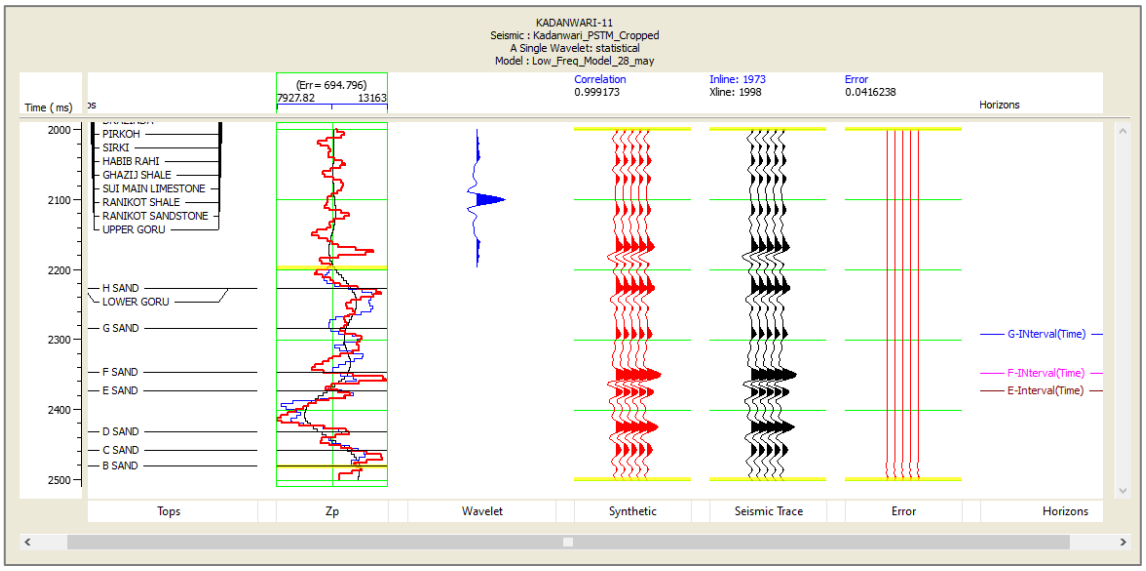

Figure 5.10 Model-based inversion analysis of Kadanwari-11

5.5.7 Model-Based Inversion Result (Inverted Section)

Model-based inversion proves to be highly effective, especially when examining both lateral and vertical variations in acoustic impedance. Model-based inversion was utilized to convert data into inverted Zp impedance within a specific time range from 2,000ms to 2,500ms, covering the formations of interest. Figures 5.11 and 5.12 display the resulting colourful sections, which are employed to detect the presence of the target in the area of interest. These inverted impedance sections demonstrate that MBI not only provides outstanding lateral resolution but also accurately captures variations in impedance within the reservoir.

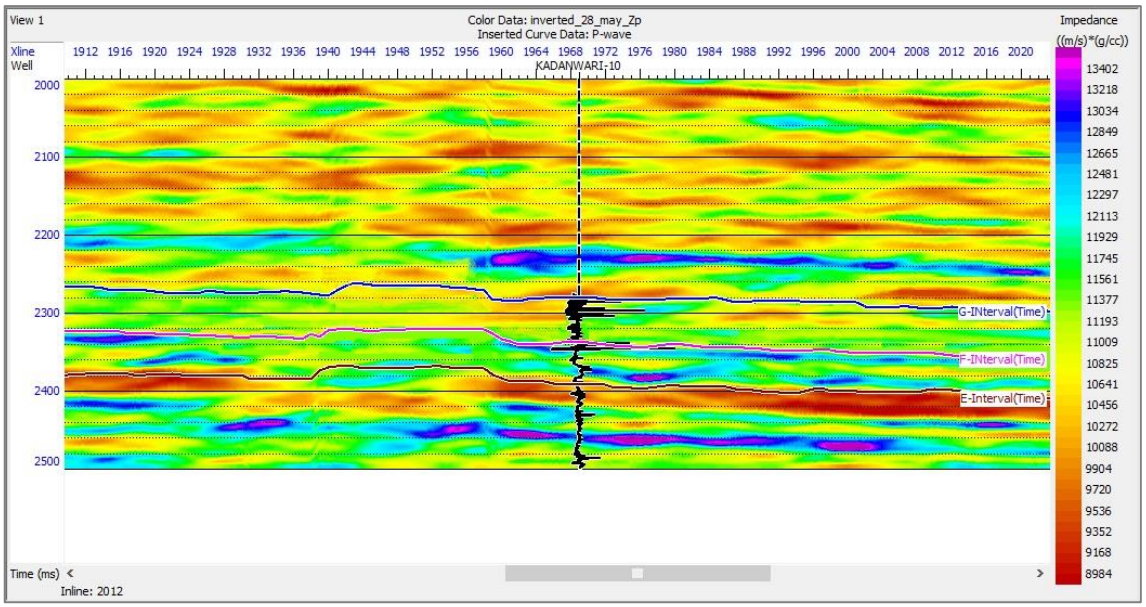

Figure 5.11 Inverted colorful section of impedance model at well Kadanwari-10

The color bar utilizes various colors to represent variations in the inverted impedance. In this scheme, yellow and brown indicate low impedance values, green indicates moderate impedance values while magenta and blue correspond to high impedance values.

In the vicinity of well Kadanwari-10, the main reservoir displays a notably low impedance (Zp) that ranges between 8984 and 10641 g/cm^3-m/s. This serves as a strong sign of gas saturation in the E Sand. The figure points out that the G Sand have even lower Zp impedance values, between 8984 and 11929 g/cm^3-m/s, suggesting the existence of a sand channel. On the other hand, F Sand presents impedance values in the range of 10825 to 11925 g/cm^3-m/s, hinting at the potential presence of a small-scale reservoir. The Lower Goru Formation comprises several layers of both sand and shale. Notably, high impedance anomalies are observed above and below the sand bodies, signalling the likely presence of shale layers. These shale layers could serve as seal rocks, effectively trapping hydrocarbons. The results are supported by both petrophysical and seismic interpretations, reinforcing the validity of these findings.

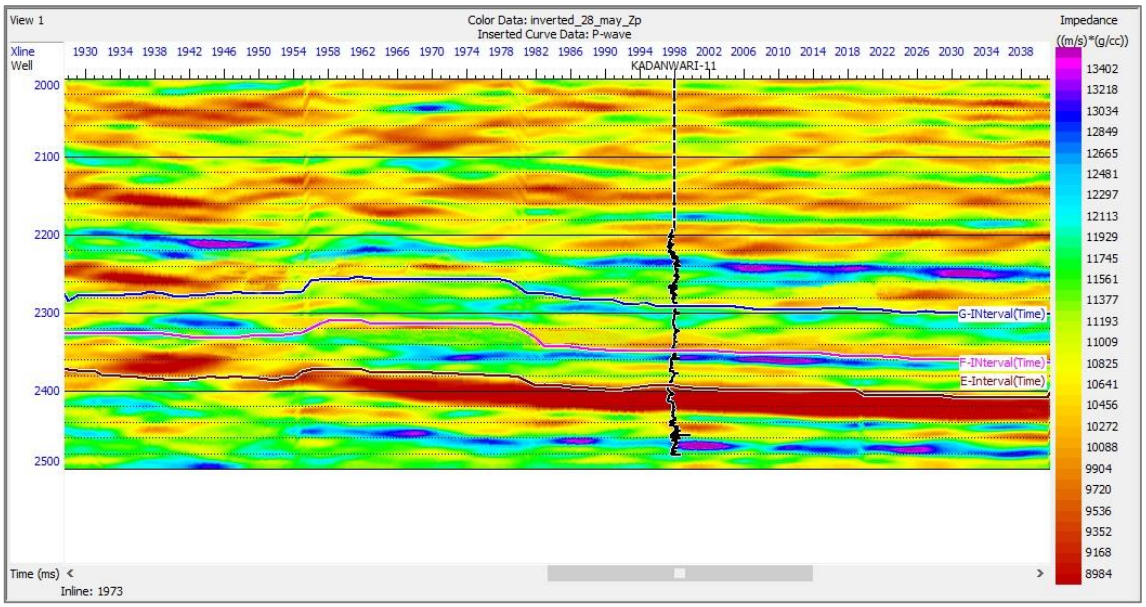

Figure 5.12 Inverted colorful section of impedance model at well Kadanwari-11

The color bar employs a range of colors to illustrate variations in the inverted impedance. In this color scheme, yellow and brown are indicative of low impedance values, green signifies moderate impedance values and magenta and blue represent high impedance values.

On section of the well Kadanwari-11, the primary reservoir exhibits a distinctively low impedance (Zp) value, falling between 8984 and 11009 g/cm^3-m/s. This is a clear indication of gas saturation within the E Sand. The figure demonstrates that the G sands show diminished Zp impedance values, spanning from 8984 to 11929 g/cm^3-m/s -m/s, pointing to the likelihood of a sand channel being present. Conversely, the F sand has impedance readings ranging from 9720 to 11925 g/cm^3-m/s, suggesting the potential existence of a minor reservoir. As the Lower Goru consists of several sequences of sand and shale layers. Observations of high impedance anomalies both above and below the sand formations indicate the presence of shale bodies. These shale bodies could serve as seal rocks. These findings are supported by both petrophysical and seismic interpretations.

5.5.8 Final Slices

The last stage involves extracting the P-Impedance slices for all formations of interest.

5.6 Slices of P-impedance

The slices of all three formations display the comprehensive variation in P-impedance across the entire cube. The color bar used in the slices utilizes a spectrum of colors to depict variations in the inverted impedance. In this color scheme, yellow and brown signify lower impedance values, green represents intermediate impedance values and magenta and blue correspond to higher impedance values.

5.6.1 P-Impedance slice of G Sand

The Inverted Zp Impedance slice of the G Sand, displayed in Figure 5.13, shows that the impedance values for G Sand range from 9,813 to 11,732 g/cm^3-m/s.

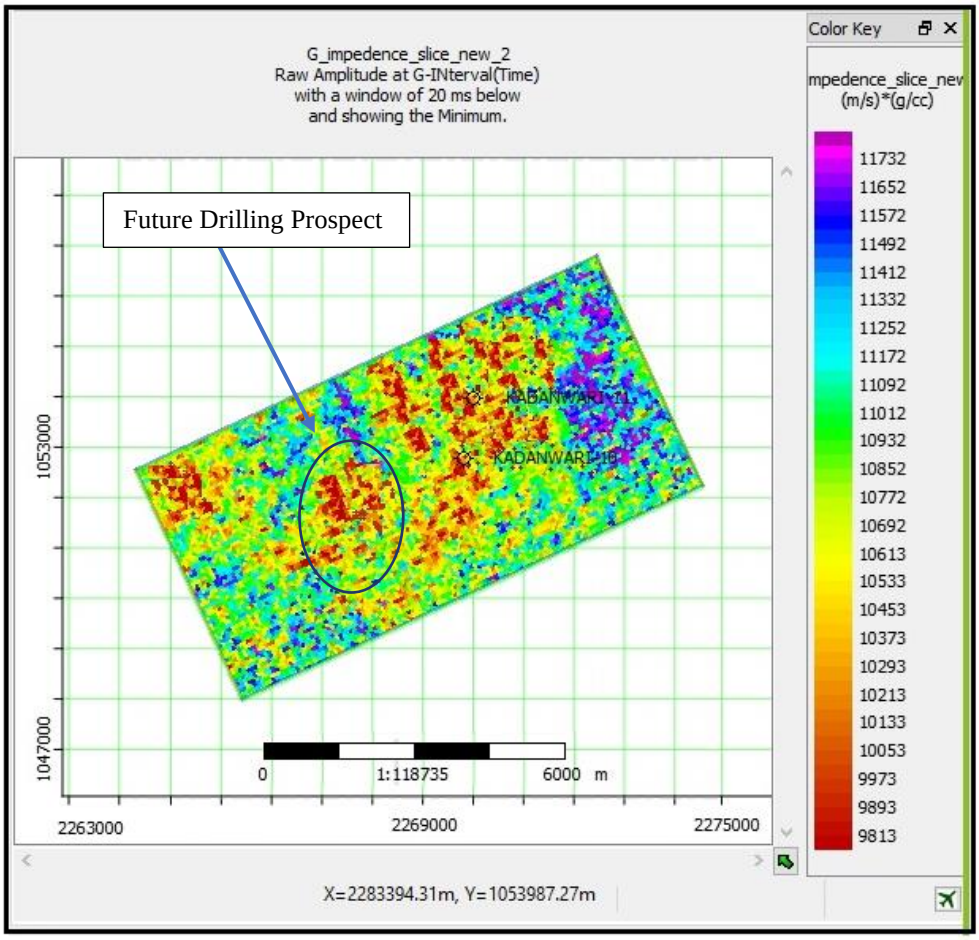

Figure 5.13 Inverted P-Impedance variations in a 3D cube slice of the G Sand.

The slice indicates areas of low impedance, ranging from 9,813 to 10,613 g/cm^3-m/s, lie in the central section of the study, predominantly in the cube's northwest corner and near the Kadanwari10 and 11 wells. These zones suggest the potential presence of hydrocarbon-bearing sand channels. In contrast, the northeast and certain sections of the southeast cube exhibit higher impedance values ranging from 11,252 to 11,732 g/cm^3-m/s. Meanwhile, the remainder of the cube exhibits moderate impedance values, spanning from 10,772 to 11,332 g/cm^3-m/s. The inversion results support and validate the findings obtained through both petrophysical analysis and seismic interpretation, confirming their accuracy. Based on all this information, it can be concluded that the G sand serve as a producing reservoir. The highlighted section within the inverted cube of G Sand, as depicted in Figure 5.13, indicates that this highlighted region, owing to its low impedance characteristics, holds potential as a prospective area for future drilling to extract hydrocarbons. This observation is further supported by the information found in the time and depth contour maps of the seismic interpretation.

5.6.2 P-Impedance slice of E Sand

The Inverted Zp Impedance slice of the E sand, as illustrated in Figure 5.14, indicates that the impedance values for the E Sand span from 8,368 to 10,575 g/cm^3-m/s.

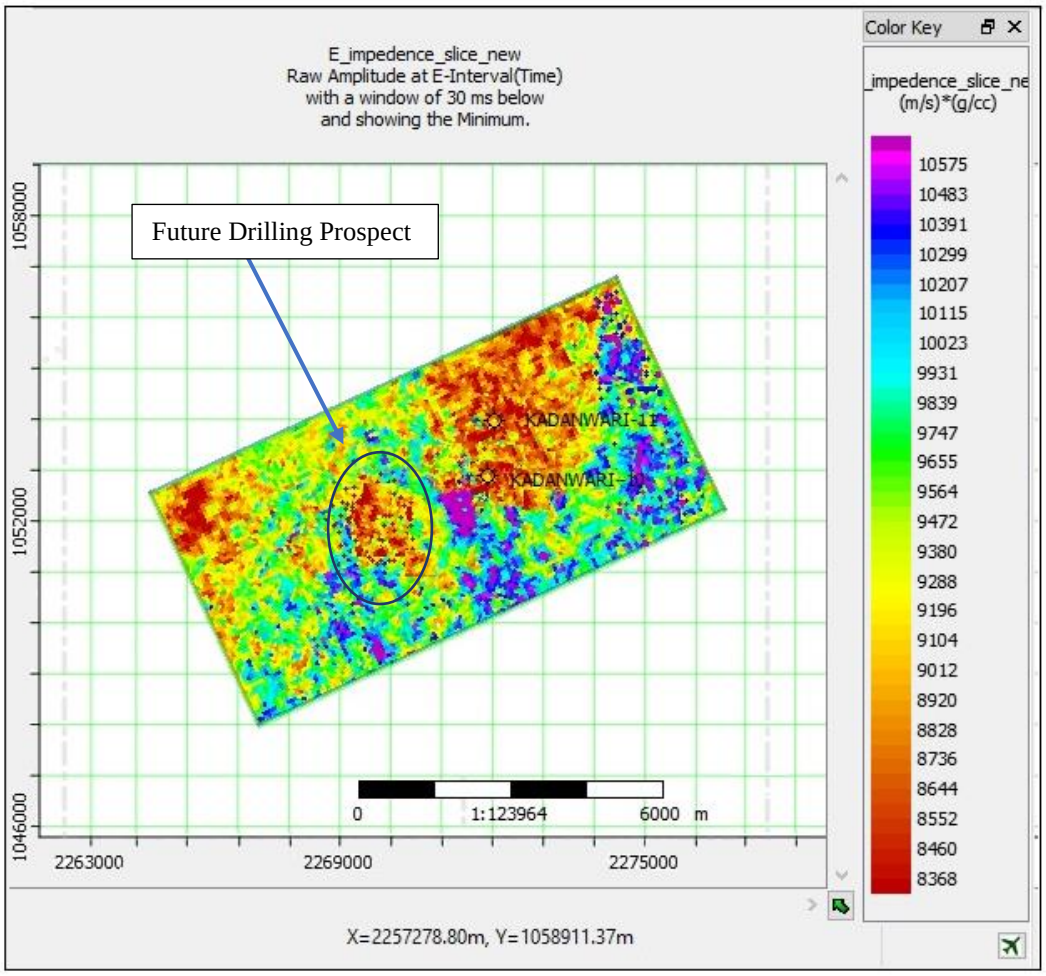

Figure 5.14 Inverted P-impedance variations in a 3D cube slice of the E Sand.

The slice highlights regions with low impedance values, which range between 8368 and 9288 g/cm^3-m/s, situated mainly in the centre of the study. These regions are especially prominent in the northwest corner of the cube and around the Kadanwari10 and 11 wells, as well as the upper northeast section. Such zones hint at the possible existence of hydrocarbon-rich sand channels. On the other hand, the eastern part and specific southern sections of the cube display elevated impedance values, lying between 10023 and 10575 g/cm^3-m/s. The rest of the cube shows moderate impedance values, ranging from 9380 to 9931 g/cm^3-m/s. The results from the inversion align with and reinforce the conclusions drawn from both the petrophysical study and the seismic interpretation, affirming their reliability. Considering all the information provided, it is evident that the E Sand is the primary hydrocarbon producer in this particular area. As shown in Figure 5.14, the emphasized area within the E Sand layer, due to its low

impedance nature, is viewed as a promising zone for potential future drilling activities to retrieve hydrocarbons. The seismic interpretation's time and depth contour maps further support this hypothesis.

5.6.3 P-Impedance slice of F Sand

The Inverted Zp Impedance slice of the F sand, as presented in Figure 5.15, reveals that the impedance values within the F Sand formation span from 8,351 to 12,025 g/cm3-m/s.

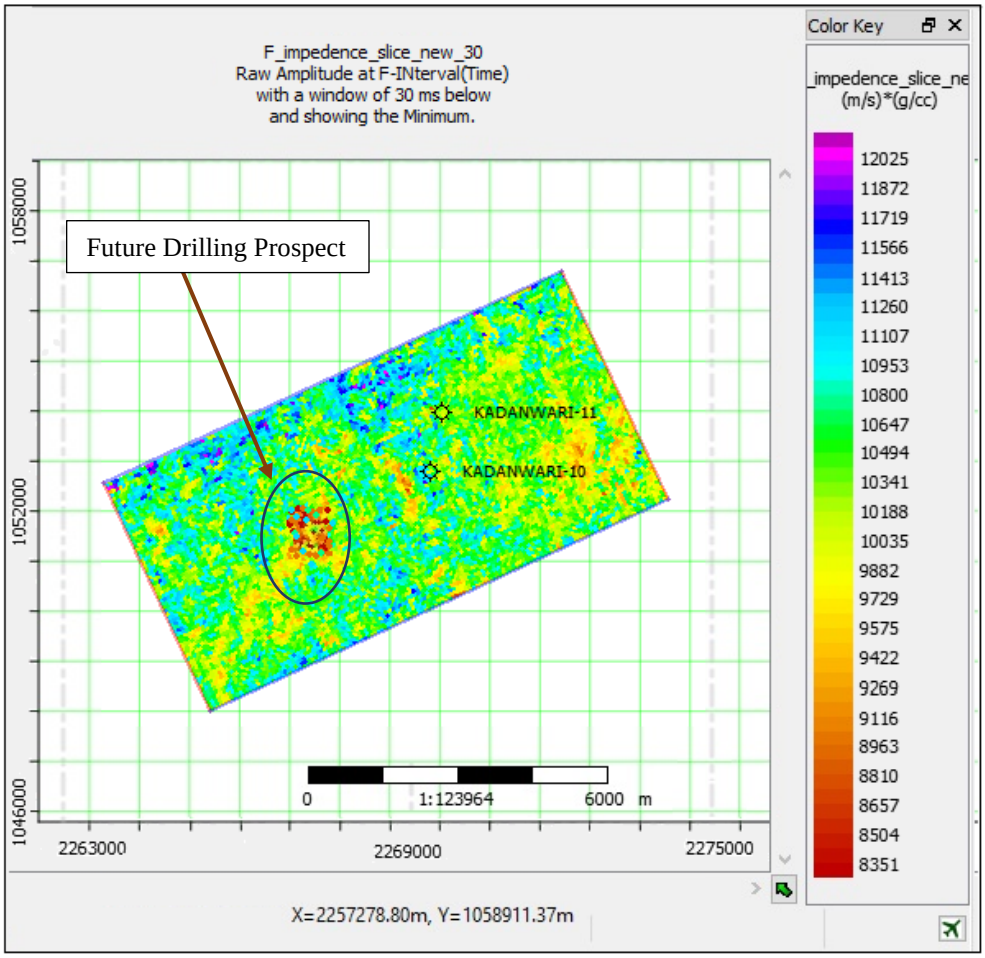

Figure 5.15 Inverted P-impedance variations in a 3D cube slice of the F Sand.

The slice identifies areas with low impedance values, ranging from 8351 to 9729 g/cm^3-m/s, mainly located in a small section of the middle and east. Conversely, the upper northern portion and a few southern parts of the cube showcase higher impedance values between 11107 and 12025 g/cm^3-m/s. The remaining parts of the cube present moderate impedance values, spanning from 9882 to 10953 g/cm^3-m/s. The inversion results validate and enhance the findings obtained from both the petrophysical analysis and seismic interpretation, thus confirming their reliability. While the F layer isn't highly productive, it hints at a potential presence of hydrocarbons. As depicted in Figure 5.15, the highlighted central region of the F Sand, due to its distinct low impedance features, also suggests a favorable area for prospective drilling to harvest hydrocarbons. This idea is further strengthened by the information presented in the time and depth contour maps derived from seismic interpretation.

5.7 Result and Discussion

The results of the inversion analysis provide a clear understanding of the geological formations and their relation to hydrocarbon production in the Kadanwari Gas Field. Two primary formations, G and E Sand of Lower Goru Formation, stand out as significant sources of hydrocarbon production due to their consistently low impedance values. These low impedance values indicate the likelihood of hydrocarbon presence within these formations. Conversely, the F layer, while not a prolific producer, exhibits distinctive low impedance features at specific locations, suggesting the possible presence of hydrocarbons. This highlights the potential for successful hydrocarbon extraction through prospective drilling efforts in this area. Notably, the Lower Goru Formation, characterized by alternating layers of sand and shale, plays a vital role in the entrapment of hydrocarbons. The high impedance anomalies observed both above and below the G and E sand bodies are indicative of shale layers, which serve as effective seal rocks, trapping hydrocarbons within the reservoir. The insights obtained from this analysis align with previous research studies by Zhang et al. (2022), Monalisa et al. (2023), and Francis & Syed (2001). These studies support and substantiate the findings regarding the reservoir potential of G and E sand zones in the Kadanwari Gas Field, derived from the inversion results.

CHAPTER 6

SEISMIC ATTRIBUTES

6.1 Seismic Attributes

Seismic attributes can be described as "quantities that are measured, computed, or inferred from seismic data." The primary purpose of attributes is to offer precise and comprehensive insights to interpreters regarding the structural, stratigraphic, and petrophysical characteristics of a seismic prospect (Taner, 2001).

Seismic attribute analysis involves breaking down seismic data into various distinct attributes. This disintegration of seismic data lacks formal guidelines for attribute computation or defining their nature. In fact, any geological or geophysical parameter derived from seismic data can be considered an attribute. Amplitude is an inherent attribute of seismic data (Barens, 2001). Seismic attributes play a crucial role in offering qualitative insights for understanding both structural and stratigraphic features, such as channels, meanders, pinch-outs, thin bed tuuning etc. They can also provide indicators for rock types and fluid content, contributing to a more comprehensive understanding of reservoir characteristics (Strecker et al. 2004).

Attributes are primarily employed to detect various features and changes in the subsurface. These include the identification of distinct bright spots, areas of gas accumulation, and demarcations of sequences. They can also highlight significant shifts in depositional settings, effects arising from thin-bed tuning, and discrepancies such as unconformities. Additionally, they can point out notable lithological transitions, localized alterations suggesting fault presence, and spatial relationships related to porosity (Seregey, 2007).

6.2 Significance of Seismic Attribute

Seismic amplitude represents a fundamental attribute of seismic data, influenced by the reflection coefficient. Seismic attributes hold significance because each of them has the capability to emphasize distinct geological features. The interpretation of 3-D seismic data is improved by analysing seismic attributes, including amplitude, instantaneous frequency, reflection strength, and instantaneous phase polarity. These attributes assist in recognizing geological structures and signal the existence of fluids (Dewett et al., 2021).

Seismic attributes have become increasingly important in the fields of petroleum exploration and production, especially as a component of seismic interpretation. Originating in the 1990s, these attributes have evolved into various forms, including structural and stratigraphic attributes While amplitude data is the basic type of seismic data, seismic attributes can unveil features that aren't readily apparent in the amplitude data alone. Utilizing seismic attributes can enhance our capabilities in geological interpretation, especially in environments with thin-bed reservoirs (Chopra and Marfurt, 2005).

6.3 Classification of Attributes

Over the past thirty years, as the range and types of seismic attributes have expanded, numerous researchers have endeavoured to categorize them into groups. Seismic properties may be classified in several ways, and over the years, multiple authors have put forward their own categorizations. The categorization often corresponds to the application, locality, or approach that the author is emphasising. The presence of several categorizations highlights the dynamic nature of the discipline and the numerous applications of seismic features in geological interpretation and reservoir characterization (Koson, 2014). Seismic attributes can be classified in various ways as elaborated below:

Attribute families categorized based on the generation process (Dewett et al., 2021).

i. Complex trace attributes (e.g., instantaneous attributes etc.)
ii. Fourier attributes (e.g., Spectral decomposition attribute etc.)
iii. Multi-trace Attributes (e.g., coherence, dip/azimuth etc.)

iv. Time attribute (e.g., horizon time picks, isochrones)

Complex trace attributes are further classified based on the domain characteristics of the attributes (Taner, 2001)**.**

i. Post stack attributes
ii. Pre stack attributes

b. Classified according to their computational characteristics:
   i. Instantaneous Attributes
   ii. Wavelet Attributes or Response Attributes
c. Attributes can be further sub-classified based on their relationship to geology:
   i. Physical Attributes
   ii. Geometrical Attributes

6.4 Attributes Analysis in the Study Area

The study area's attribute analysis involved the utilization of the following attributes.

6.4.1 Instantaneous Phase

The phase information operates independently of trace amplitudes and pertains to the propagation of the phase of the seismic wave front. Given that wave fronts are often characterized as lines of consistent phase, the phase attribute is also a physical property. This makes it an effective tool for discriminating and classifying geometric shapes. The computation for this attribute, using real and imaginary traces, is given by:

$$\Theta (t) = \arctan [h (t) / f (t)]$$

Because instantaneous phase refers to the phase component of wave propagation and lacks amplitude information, it is the greatest indication of lateral continuity. It may be used to highlight interfaces in sections with high amplitude decay and even deeper horizons that are not apparent in normal amplitude sections (Khan & Akhter, 2015). The instantaneous phase attribute enhances the visibility of strong events, making them more distinct. It is particularly effective at emphasizing the discontinuities of reflectors, faults, pinch outs, angularities, and bed interfaces. Additionally, features such as seismic sequence boundaries, sedimentary layer patterns, and areas with onlap/offlap patterns tend to exhibit enhanced clarity when visualized using the instantaneous phase attribute (Das et al., 2017).

The highlighted circles in Figures 6.1, 6.2 and 6.3 pinpoint the discontinuities caused by faults, as well as the lateral continuity of Lower Goru sands.

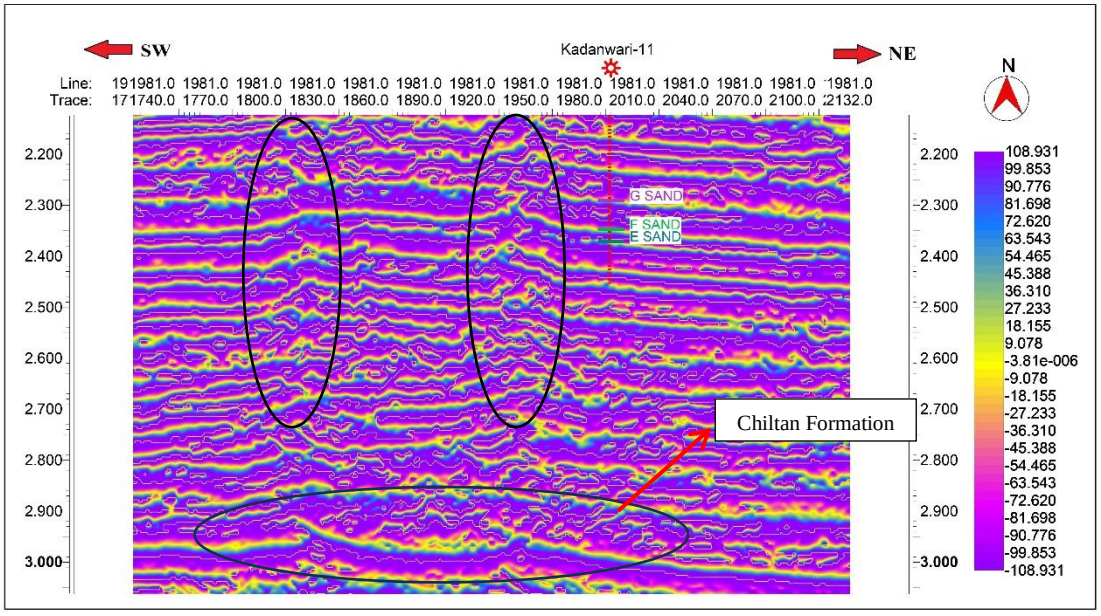

Figure 6.1 Instantaneous Phase Attribute at well Kadanwari-11 on inline 1981, with circles highlighting the discontinues and lateral continuity of horizons.

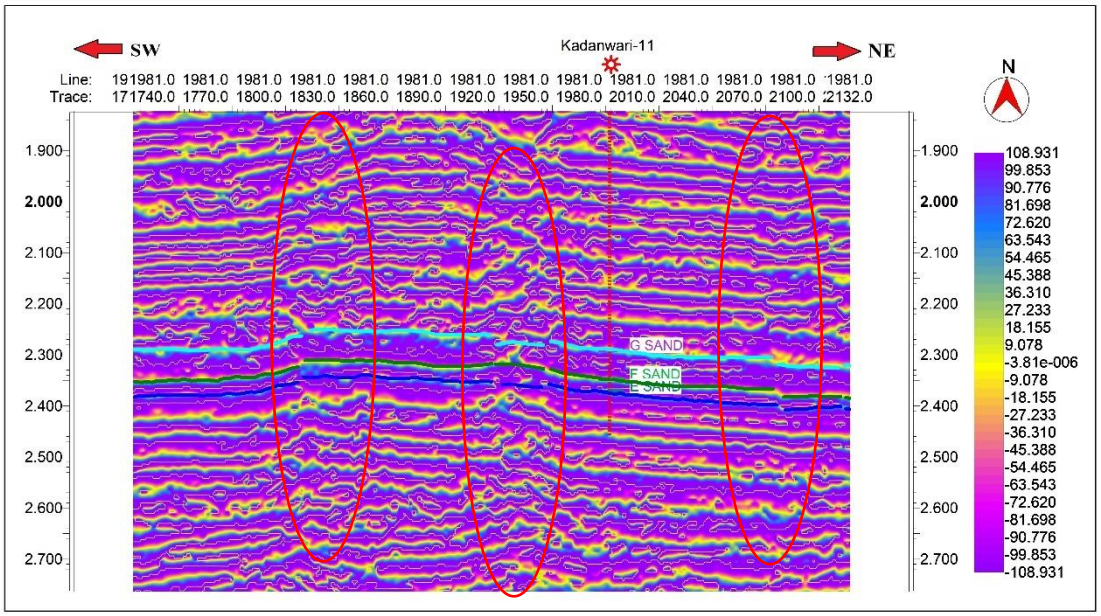

Figure 6.2 Instantaneous Phase Attribute at well Kadanwari-11 on inline 1981, with circles highlighting the discontinues and lateral continuity of marked horizons of interests.

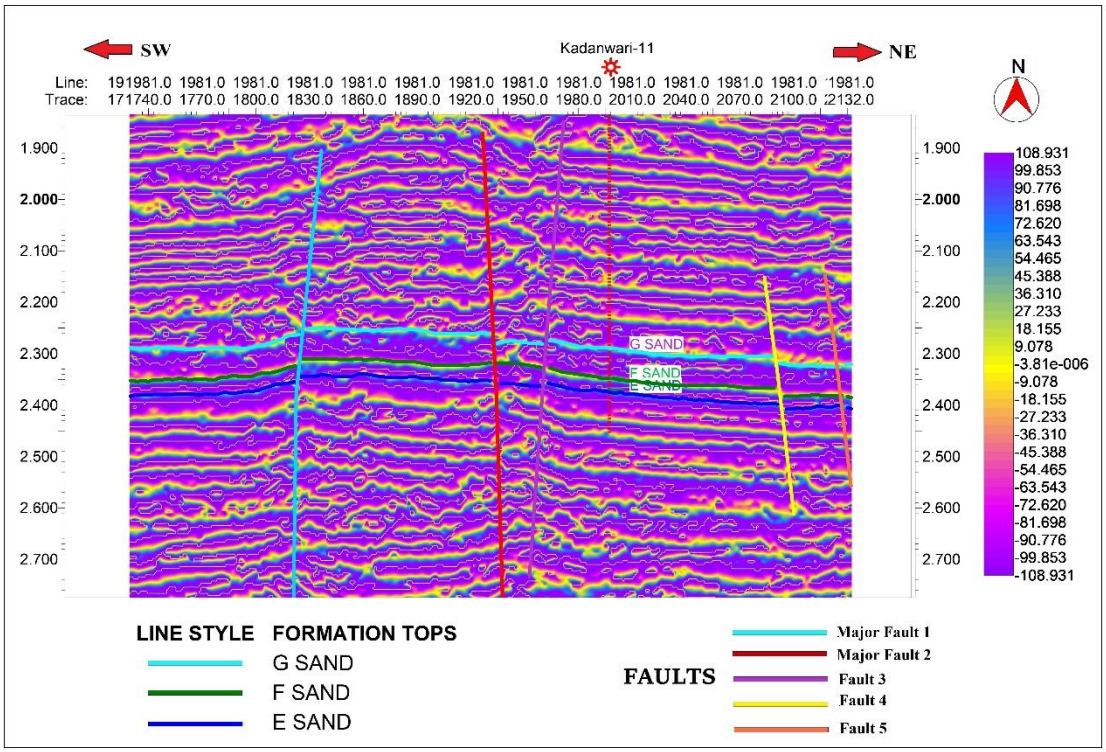

Figure 6.3 Instantaneous Phase Attribute at well Kadanwari-11 on inline 1981, demonstrates the identifies the faults and horizons at previous discontinuity points.

6.4.1.1 Results and Discussion

Figure 6.1, 6.2 & 6.3 illustrates the instantaneous phase attribute, with a range of values spanning from -108 to +108 degrees. The interpreted horizons align with the zero phase regions highlighted in yellow. This alignment provides additional validation for the interpretation, considering that the input data is zero phase. Circles highlighted the discontinuities caused by faults. While arrow denotes the lateral continuity of high impedance Chiltan Formation of Lower Indus Basin. Major primary faults which are in my case are MF1 and MF2, are originated from Chiltan formation.

The highlighted circles in Figures 6.1, 6.2, and 6.3 serve to identify faults, confirming their presence by comparing them to the normal amplitude section depicted in Figure 3.6 of the interpretation section. A noticeable distinction can be made when comparing the results with amplitude-based sections: the instantaneous phase attribute reveals significantly deeper horizons, and clear discontinuities of faults that might not be as clearly visible in conventional amplitude sections, same is suggested by (Das et al., 2017).

6.4.2 Trace envelope (instantaneous amplitude)

The attribute known as the "Trace Envelop," alternatively referred to as "Reflection Strength," signifies the total instantaneous energy of the trace or signal and exhibits a magnitude that is directly related to the reflection coefficient. The trace envelope attribute has a direct connection to the contrasts in acoustic impedance. It can reflect either the contrast of individual interfaces or, more commonly, the collective behaviour of multiple interfaces, contingent on the seismic bandwidth (Barnes, 2001). It emphasizes areas with pronounced acoustic events, appearing as bright spots on both positive and negative events. Bright spots offer valuable insights into the presence of channel bodies or sandy lithology due to variations in acoustic impedance. This attribute also provides information regarding lithological changes, sequence boundaries, the effects of thin-bed tuning, significant shifts in the depositional environment, and the

potential presence of gas, among other geological features (Taner and images, 2001). Seismic interpreters find this attribute particularly valuable because it eliminates the reliance on the original seismic trace values, which are influenced by the phase or polarity of the seismic data, both factors significantly influence the apparent brightness of a reflection (Koson et al., 2014).

This attribute is calculated for the Kadanwari cube to identify significant variations in lithologies. Since it represents the modulus of the complex trace, the envelope trace will consistently maintain a positive value. Figure 6.4 displays the envelope attribute map for Incline 1981 within the Kadanwari cube with circles highlighting the discontinuities and high amplitude or horizons. In this map, a prominent thick (red) area signifies the highest reflection strength, which corresponds to the Lower Goru Sands. The highlighted circles in the subsequent Figure 6.4 illustrate spatial patterns that indicate variations in sand thickness and structural breaks due to faults.

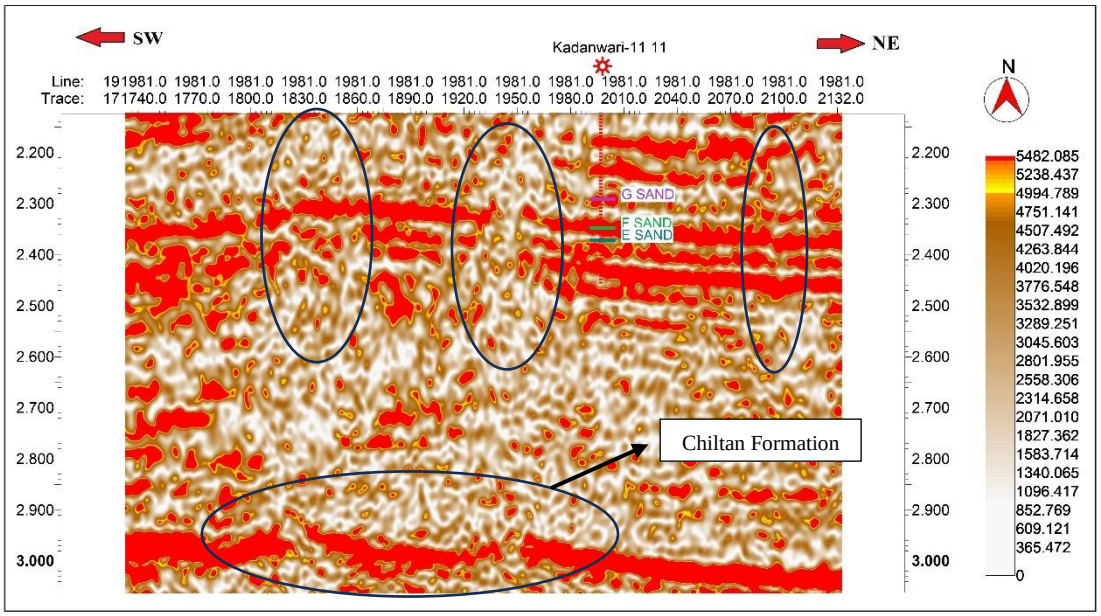

Figure 6.4 Instantaneous amplitude or Trace envelope attribute at well Kadanwari-11 on inline 1981, with circles highlighting the discontinues and lateral continuity of marked horizons of interests.

Figure 6.5 displays the envelope attribute map for Inline 1981 within the Kadanwari cube with marked horizon of G, F and E sand of Lower Goru Formation.

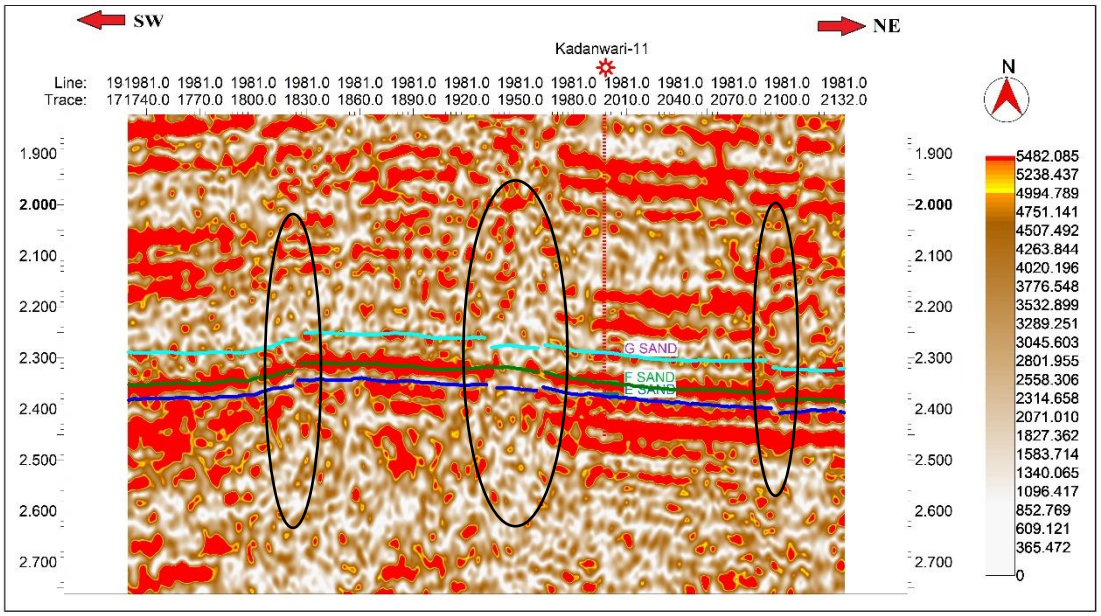

Figure 6.5 Instantaneous amplitude or Trace envelope attribute at well Kadanwari-11 on inline 1981, with marked horizon of G, F and E sand of Lower Goru Formation.

6.4.2.1 Results and Discussion

In the figures, a significant and pronounced red-colored region indicates the highest level of reflection strength, which corresponds to the Lower Goru Sand intervals (G, F, and E sand intervals) and the Chiltan formation. The highlighted circles in Figure 6.4 and 6.5 serve to illustrate spatial patterns that reveal variations in sand thickness and structural disruptions caused by faults. This confirmation is achieved by comparing them to the standard amplitude section shown in Figure 3.6 in the interpretation section.

The amplitude anomaly at the desired horizons (G, F, and E sand intervals) is more conspicuously and distinctly observable in the Instantaneous Amplitude attribute section. The Chiltan Limestone stands out with a remarkable peak in instantaneous amplitude, primarily owing to the substantial contrast in acoustic impedance between the

Chiltan Limestone and the shales overlying it (Sembar Formation). So, the lower Guru sands (G, F, and E sand intervals) and Chiltan formation exhibit a positive response, thereby verifying their presence. Several other authors (Chopra & Pruden, 2003; Das et al., 2017; Ashraf et al., 2019) have also provided similar reviews on this observation.

6.4.3 Spectral Decomposition Attribute

The process of spectral decomposition involves breaking down seismic data into its constituent different frequency elements through various mathematical techniques, such as employing short-time windows and utilizing the Fourier transform. This method shifts the analysis of seismic information from the time-based perspective to a frequency-based one. By investigating data across different frequencies in the time domain and making comparisons, valuable insights into the finer aspects of the data can be gained (Ashraf et al., 2019).

Spectral decomposition phenomenon, characterized by higher frequencies corresponding to shorter wavelengths and the ability to detect narrow channels, led to the development of this technique. Within specific frequency bandwidths, various structures of differing sizes become more discernible because of tuning to factors such as thickness and other properties (Tayyab et al., 2017). Spectral decomposition attributes were employed in my study area. By conducting spectrum analysis on the recorded amplitude and frequency data of the Kadanwari 3D cube, it was determined that a frequency bandwidth of 8-60 Hz is evident in the dataset. The provided figure illustrates that the amplitude remains stable within the range of 0.6-1, with a bandwidth of 10-40 Hz (Figure 6.6).

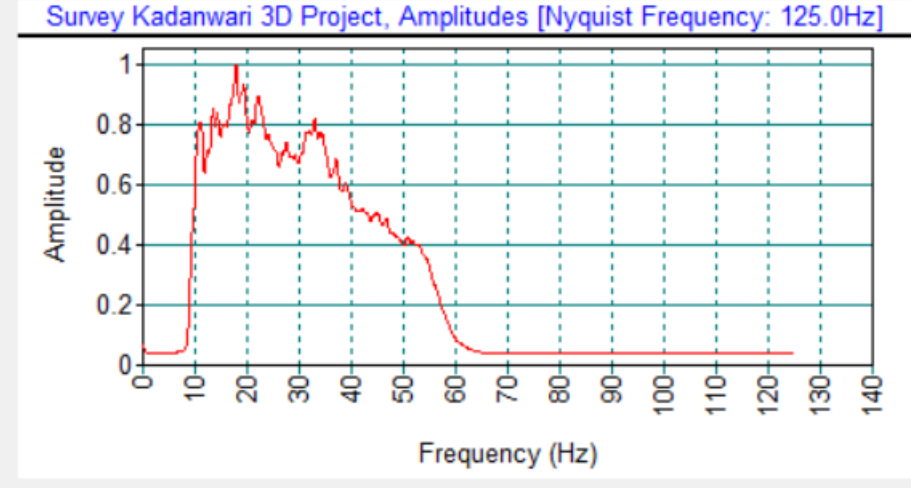

Figure 6.6 Amplitude and frequency spectra for Kadanwari 3D cube.

The attribute seismic sections, taken from the same inline, were exhibited using distinct frequencies (28 Hz, 37 Hz, and 48 Hz) with the intention of examining the outcome of spectral decomposition at each precise frequency. As the frequencies increased incrementally, the thin sand beds of Lower Goru (G, F, and E sands) within the Kadanwari 11 well became progressively visible. This trend is depicted in Figure 6.7 to Figure 6.10, each within their corresponding frequency sub-bands.

The highlighted circles point out structural features that are not readily distinguishable in normal amplitude seismic section as shown in following figures below.

\

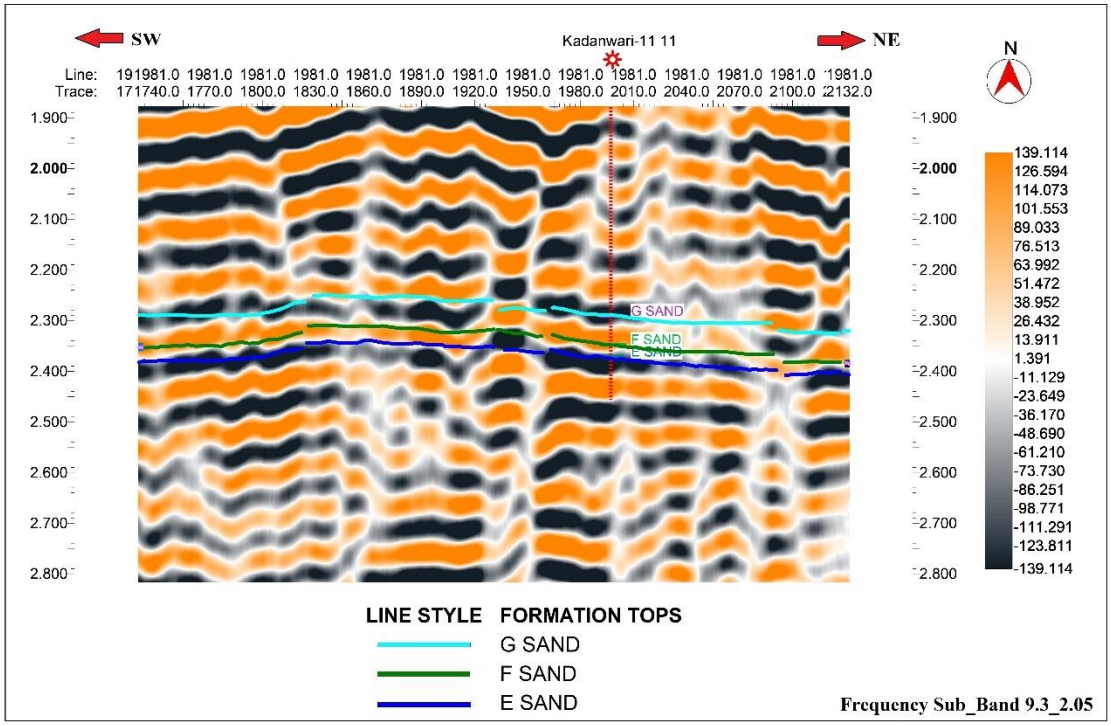

Figure 6.7 Spectral Decomposition attribute of inline 1981 at 9.3 Hz frequency.

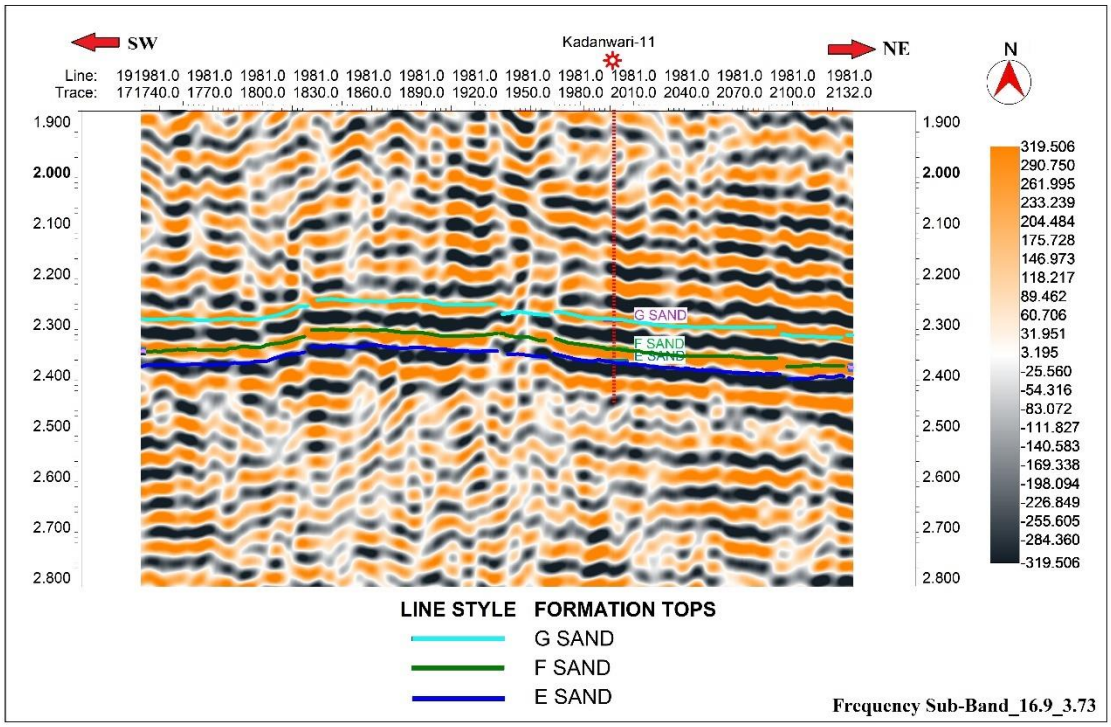

Figure 6.8 Spectral Decomposition attribute of inline 1981 at 16.9 Hz frequency.

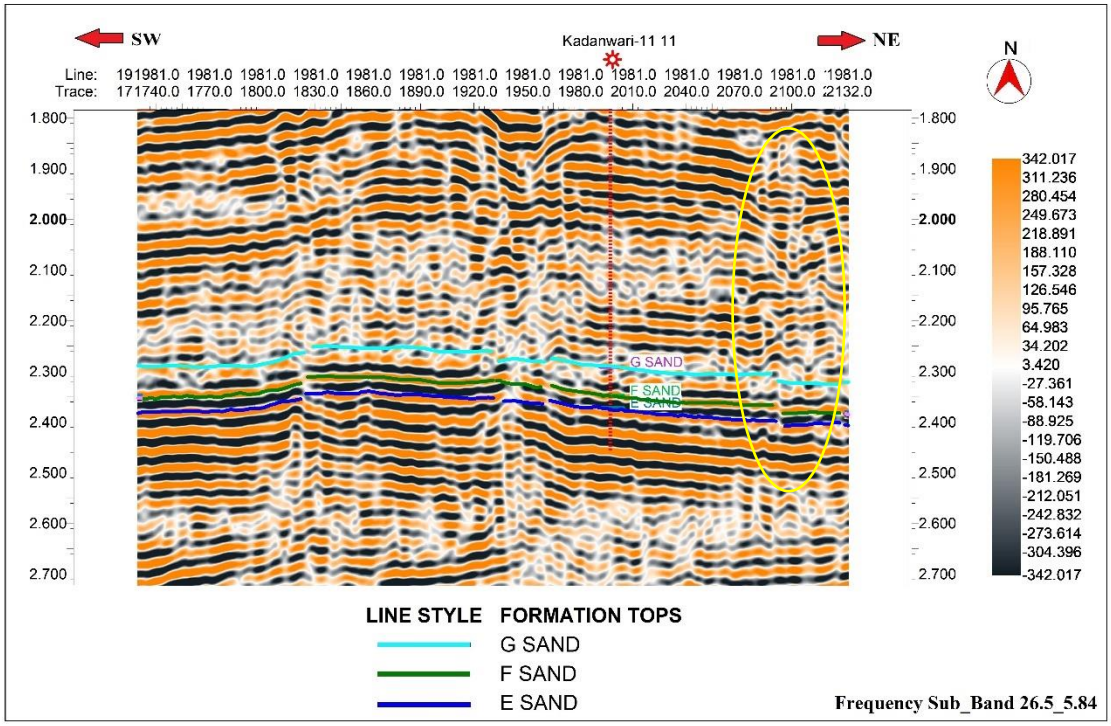

Figure 6.9 Spectral Decomposition attribute of inline 1981 at 26.5 Hz frequency.

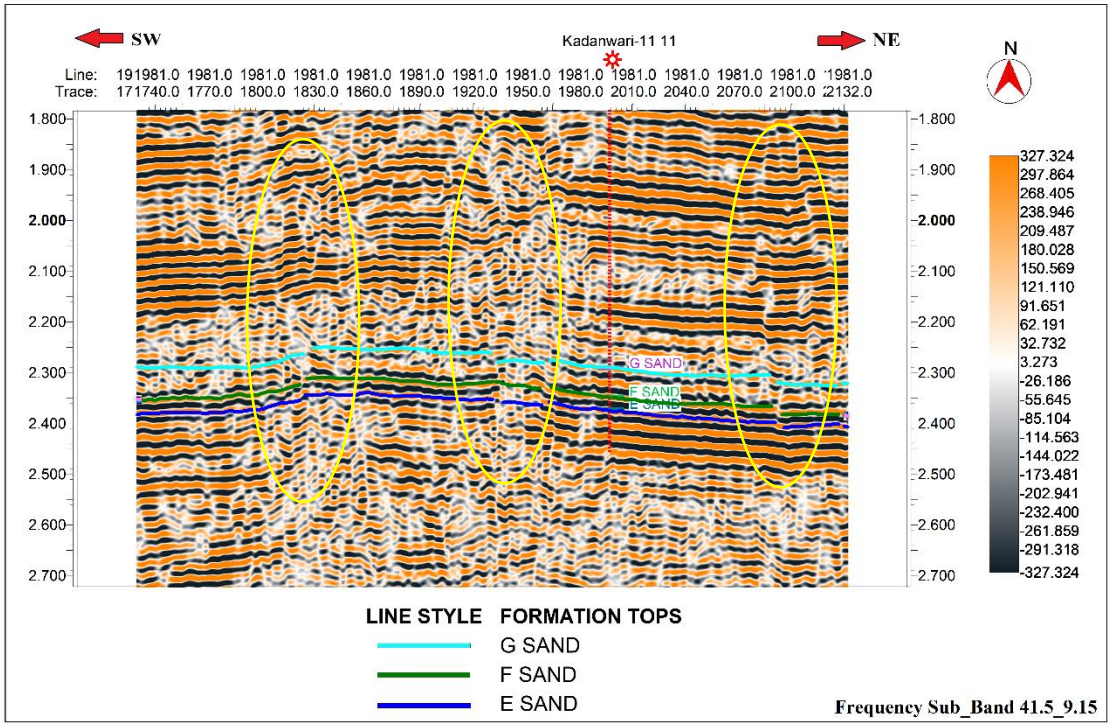

Figure 6.10 Spectral Decomposition attribute of inline 1981 at 41.5 Hz frequency.

6.4.3.1 Results and Discussion

Spectral decomposition attribute proves particularly effective in identifying thin bed sand layers. Thicker beds are more prominently depicted through lower frequencies, whereas finer bed layers are optimally distinguished using higher frequencies (Koson et al., 2014). Similar methodology was applied to my area under investigation, resulting in the identification of faults and horizons within the Lower Goru Sands at various frequencies. These figures illustrate that as frequency increases, spectral decomposition becomes valuable for effectively revealing discontinuities. Circles highlights the discontinuities. These features were previously undetectable within the normal time amplitude seismic section. In certain frequency ran

ges, different structures with varying sizes become more distinguishable due to their sensitivity to factors like thickness and various properties (Ahmad & Rowell, 2012). The spectral decomposition attribute reveals distinct characteristics at various frequencies within a specified band limit. Among these frequencies, four particularly noteworthy results are depicted in the figures above. The initial figure illustrates the attribute's performance at a frequency of 9.3 Hz. At this specific frequency, the identification of thin beds is challenging, but thicker beds are clearly discernible. Subsequently, the attribute was examined at a slightly higher frequency, 16.9 Hz, where the beds remain somewhat unresolved but exhibit improved delineation compared to the 9.3 Hz frequency. As the frequency increased to 26.5 Hz, the spectral decomposition attribute remarkably achieved a precise resolution of the thin beds, and an emerging fault became evident, which had remained unresolved at previous frequencies. Finally, the attribute was assessed at 41.5 Hz, where it proficiently resolved the thin beds and confirmed the presence of a fault that was relatively challenging to pinpoint on a standard seismic section.

Thicker beds or characteristics exhibit enhanced amplitude at lower frequencies, while thinner beds display increased amplitude at higher frequencies (Tayyab et al., 2017). The figures demonstrate that as frequencies rise, sand beds G, F, and E are most effectively resolved. The highlighted circles in the preceding figures depict structural disruptions arising from faults. This validation is accomplished by contrasting them with the reference amplitude section featured in Figure 3.6 within the interpretation section.

CHAPTER 7

MACHINE LEARNING-BASED VS COMPUTATION, AVO VALIDATION, AND FACIES MODELING

7.1 General Introduction

Within the broad field of artificial intelligence, machine learning centers on techniques and algorithms that allow computers to learn from examples. Its primary objective is to autonomously extract information from data, employing computational and statistical approaches (Ali et al., 2023). The utilization of machine learning (ML) in geosciences has become increasingly prevalent because of advancements in computer science algorithms. ML has proven to be a valuable tool in this field due to its ability to analyze provided data and identify underlying relationships, ultimately enabling the prediction of the desired outcome (Gupta et al., 2021).

Shear sonic log (DTS) plays a significant role in identifying the specific lithologies and fluid types present within reservoirs, which holds paramount importance in field development & production. It is especially valuable for distinguishing between wet sands and gas-bearing sands (Liu et al., 2021). In the Lower Indus Basin (LIB), many wells lack shear sonic logs (DTS) for various reasons. In such cases, DTS logs are often generated through complex computational processes that rely on several assumptions and prerequisites. These computational methods can potentially impact the accuracy of the true reservoir characteristics Recently, machine learning (ML) has evolved as a robust and highly optimized method for accurately predicting shear sonic logs (DTS) with a reduced requirement for extensive input dataset (Ahmed et al., 2022).

In my research, I utilize a machine learning-based multi-regression approach to calculate shear sonic velocity (Vs), which greatly improves prediction accuracy when compared to Vs values obtained through the Castagna equation. To validate the reliability of this approach, I employed the AVO forward modeling algorithm to the shear sonic

velocity (Vs) values obtained from both methods. The results revealed that the Vs computations derived from the machine learning approach consistently provided better results compared to those obtained from the Castagna equation.

7.2 Methodology for Vs Prediction

In order to improve the accuracy of predicting shear velocity (Vs), conducted a comparative analysis between two distinct methods: the widely accepted Castagna equation and a new approach incorporating machine learning-based multi-regression. This study not only assesses and compares the predictive capabilities of these methods but also validates their results using the AVO forward modeling algorithm. Figure 7.1 below presents a comprehensive workflow that illustrates the entire process.

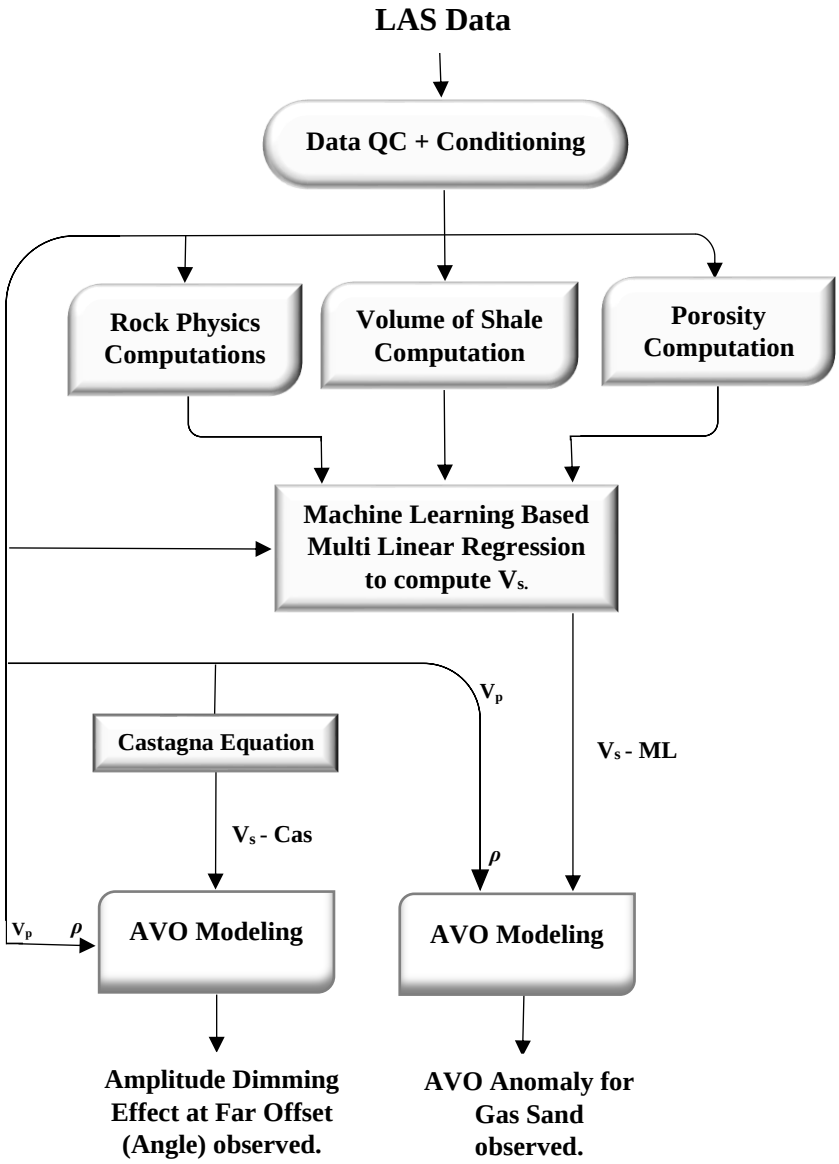

Figure 7.1 Flow Chart of the ML-based multi-regression approach for predicting shear sonic velocity (Vs) and its validation using AVO forward modelling compared to the Castagna equation.

The flow chart presented above provides a structured overview of the Vs prediction process and its validation through AVO forward modeling. Each step is delineated in detail in the subsequent sections.

7.3 Load LAS file

At the initiation of the workflow, the LAS data file of the Kadanwari-03 well is imported. This pivotal step serves as the foundation for further analysis. The predictive methodology employed in this chapter is systematically evaluated by executing the entire workflow using specialized K-tron wavelet software.

7.4 Data Quality Control & Conditioning

In the second phase of the workflow, a comprehensive quality control (QC) assessment of the data is carried out to ensure its accuracy and reliability. The primary objective is to identify any irregularities, errors, or anomalies within the data that could potentially undermine its reliability or accuracy. The process begins by loading the LAS data files and identifying the specific depth range within which the logs have been run or acquired. This step sets the boundaries for the dataset under examination. To refine or enhance the quality of the data and prepare it for subsequent analysis, an initial data conditioning process, including procedures like deglitching, trimming, and filtering, is performed. This phase's significance lies in ensuring that the LAS data is free from artifacts or discrepancies that could potentially lead to misinterpretations in subsequent geological analyses. Through the systematic resolution of glitches, removal of irrelevant

data, and noise mitigation, this phase establishes a solid foundation for accurate interpretations and modeling of subsurface geological features. After the conditioning process, Figure 7.2 illustrates the final set of input logs that will be employed for computation purposes.

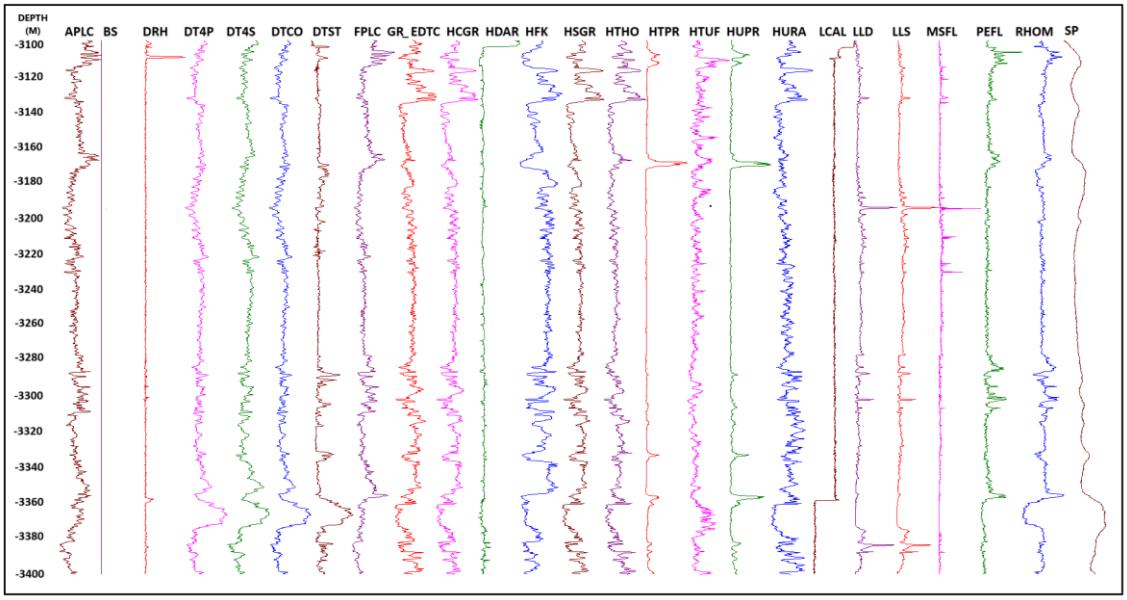

Figure 7.2 Final set of Input log curves for depth interval of my interest from 3110 to 3400 m.

7.5 Parameter Computation and Analysis

After performing the initial refinement/conditioning on the data, three parameters were calculated, which are as follows:

1) Rock physics analysis
2) Volume of shale computation
3) Porosity computation

7.5.1 Rock Physics Computation

The term "rock physics" encompasses a range of methods used to characterize the geological attributes (such as lithology, porosity, and saturation) of rock under specific physical conditions (such as temperature and pressure), along with their corresponding elastic and seismic properties (including velocity, elastic modulus, and impedance). These approaches can be employed for rock physics modeling, which involves predicting seismic elastic properties based on geological information, or for rock physics inversion, which entails estimating geological characteristics from elastic (seismic) observations (Dalvand & Falahat, 2021).

In order to construct a machine learning-based multi-regression model for predicting Vs, it is crucial to have labeled training data. Rock physics equations provide a framework for generating synthetic data by simulating the expected Vs given certain rock properties. These synthetic datasets can be combined with real data for training purposes. The P-wave velocity (sonic) log, S-wave velocity (computed shear sonic) log, and density log serve as the inputs for calculating various elastic logs associated with different moduli, including acoustic impedance and shear acoustic impedance logs. In the K-tron Wavelet software, the rock physics functions library is utilized to extract rock physics parameters, as depicted in the figure presented below, labeled as Figure 7.3.

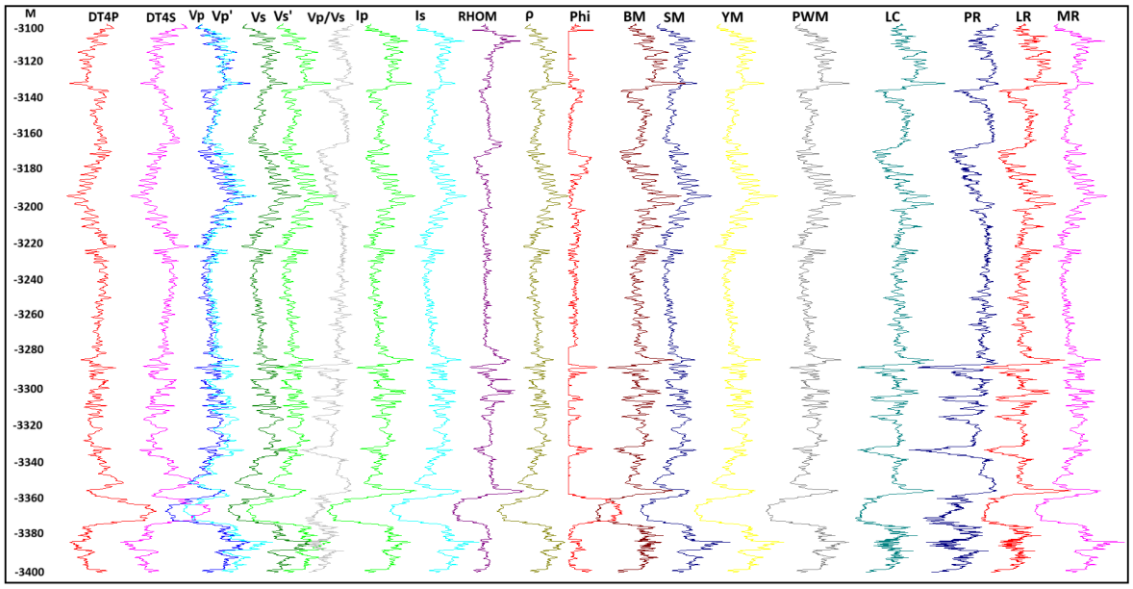

Figure 7.3 Automated computation of rock physics parameters via the rock physics functions library in K-tron Wavelet software.

The rock physics analysis illustrated in the figure above yields critical parameters that hold significant importance in understanding the mechanical properties of rocks. These derived parameters serve as fundamental inputs for a machine learning-based multi-regression model. This model is designed to learn, analyze and comprehend intricate relationships between these mechanical properties and the shear wave velocity (Vs). By assimilating these relationships, the model gains the ability to make highly accurate predictions of Vs. This integration of rock physics analysis and machine learning enhances the predictive capabilities, allowing for improved characterization and modeling of subsurface materials and their associated mechanical properties. These rock physics parameters play a crucial role in characterizing the physical properties of subsurface materials, facilitating better geological and geophysical analysis in various applications.

7.5.2 Volume of Shale Calculation

The volume of shale was computed from the input GR log. For an understanding of the lithological composition of subsurface formations, shale volume is essential. Shale possesses distinct acoustic and mechanical properties that have a significant impact on the velocity of shear waves (Vs). The determination of the shale fraction within a geological formation can be achieved by the computation of its volumetric measurements. The provided information has significant value due to the characteristic of shale exhibiting comparatively lower Vs in comparison to other rock types. Shale volume is a key factor in predicting Vs (shear wave velocity) based on the lithological composition of the subsurface. The volume of shale (Vsh) was employed as one of the input features for the machine learning-based multi-regression model.

7.5.3 Porosity Computation

Porosity is an essential characteristic of subsurface formations. Porosity values can be determined by analyzing neutron porosity (NPHI) and compressional velocity (Vp) data. Averaging these values provides an accurate representation of the subsurface porosity distribution. Porosity provides information about the empty or void spaces within

the subsurface material, which can significantly affect the propagation of seismic waves, including the velocity of shear waves (Vs). Porosity and Vs are frequently correlated. In general, materials that have higher porosity tend to exhibit lower values of Vs. This is because the existence of voids or pores within the material decreases its stiffness, which in turn reduces its shear wave velocity. Porosity was employed as an input feature in a machine learning-based multi-regression model with a purpose of predicting Vs. By incorporating porosity as an input feature, the model can utilize this data to improve the accuracy of its predictions.

7.6 Machine Learning-Based Multi Regression

ML encompasses computational techniques that enable systems to learn from data and improve their ability to make accurate estimations and classifications (Rahimi & Riahi, 2022).

Multiple Linear Regression is a widely used statistical method in various fields, such as geophysics, for establishing the connection between multiple independent variables and a dependent one. In geophysics, multiple linear regression is a highly adaptable technique capable of addressing various challenges, including the prediction of geological features, the estimation of parameters beneath the Earth's surface, and the simulation of geophysical processes (Radwan et al., 2022).

In my scenario, I employ a Multi-Linear Regression (MLR) model for the automated prediction of shear sonic (DTS). The model is trained by utilizing a variety of independent variables that have been previously computed. These variables encompass initial logs, rock physics calculations, volume of shale determinations, and porosity computations, all of which are fed into a neural network. The model uses these inputs to learn the intricate relationships between these parameters and Vs (shear sonic velocity), enabling it to make more accurate predictions of Vs.

In the Lower Indus Basin, there are thin packages of sand and shale that are challenging to differentiate manually. To address this, I've employed machine learning to identify and classify these layers into distinct groups. After the classification, neural-network-based multi-regression analysis is carried out to derive their specific shear wave

equations. Figure 7.4 depicts the computation of Vs Equations for the three distinct lithologies using a machine-learning approach.

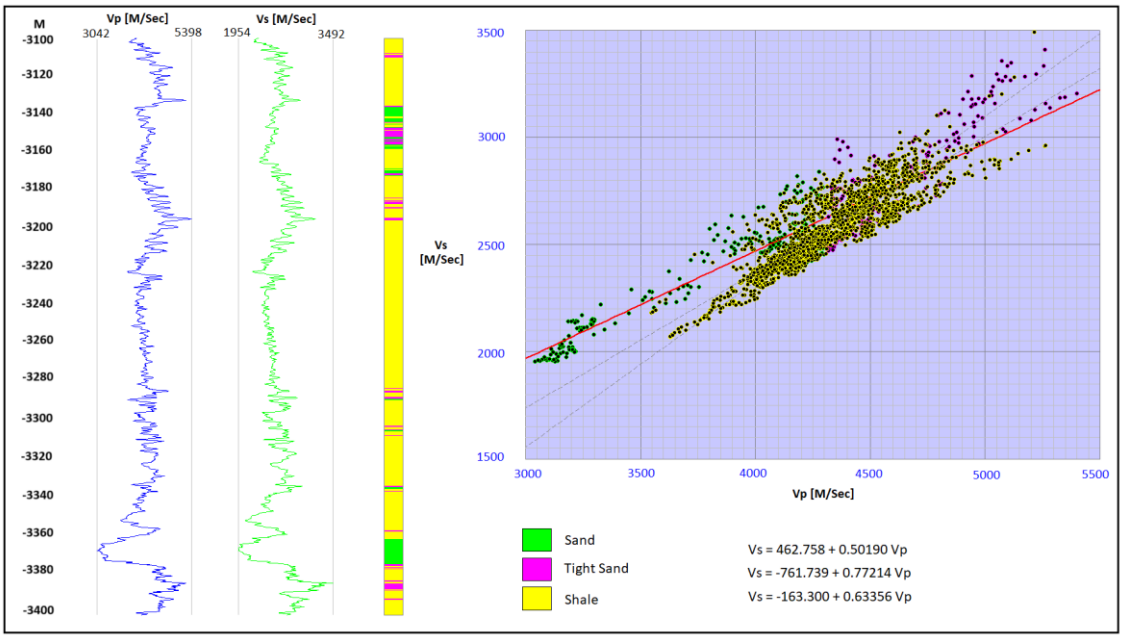

Figure 7.4 Shear Sonic (Vs) Computed from Multi-Regression Based Machine Learning Algorithm.

In this particular machine learning model, the primary objective is to categorize data based on input parameters through a multiple regression approach. The data is categorized into three distinct categories:

1. **Pure Clean Sand**: This category represents geological formations composed primarily of clean, unadulterated sand.
2. **Shaly Sand (Tight Sand)**: This category encompasses sand formations that contain varying degrees of shale intermixed, often referred to as tight sand.
3. **Shale**: This category consists of geological formations dominated by shale rock.

Once the data points are successfully categorized and clustered into these three groups, individual regression equations are computed for each category, enabling precise shear sonic predictions. The equations for each lithology are as follows:

i. **For Clean Sand**:

$$V_S = 462.758 + 0.50190\ V_P$$

ii. **For Tight Sand (Shaly Sand)**:

$$V_S = -761.739 + 0.77214\ V_P$$

iii. **For Shale**:

$$V_S = -163.300 + 0.63356\ V_P$$

These equations were formulated using data from wells where both compressional sonic (Vp) and shear sonic (Vs) values were accessible. The model dynamically switches between these equations on a sample-by-sample basis, contingent upon the specific lithology of each sample being evaluated. If this multi-regression model is used on a well without shear sonic data, the appropriate equation will automatically be selected based on the category.

The presence of Shear Sonic logs, commonly referred to as DTS, holds paramount importance in the process of distinguishing lithological and fluid properties within reservoirs. This discrimination is pivotal for effective field development and production strategies. Unfortunately, a significant number of wells within the Lower Indus Basin (LIB) do not possess DTS logs. In the absence of these logs, reservoir analysis relies on traditional methods that rely on empirical relationships and rock physics models. However, these conventional techniques entail extensive computations and necessitate certain assumptions and prerequisites. These factors can potentially introduce uncertainties and compromise the accurate characterization of reservoir properties. (Ahmed et al., 2022).

To assess the accuracy of the shear sonic values predicted by the Machine Learning model, a comparative analysis was conducted. Initially, Vs values were calculated using the Castagna equation. Subsequently, an Amplitude Versus Offset (AVO) analysis was employed to compare the predicted Vs values with those obtained through the Castagna equation. This rigorous evaluation ensures the reliability and effectiveness of the machine learning model in estimating shear sonic values within various lithological contexts.

7.7 Castagna's Computed Vs

The Castagna relationship, which relates compressional velocity (Vp) to shear velocity (Vs), was originally employed the DTS (Shear Sonic) log in wells where Vs was not available (Castagna et al., 1985). The Castagna equation for Vs is as follows:

$$V_S = a \times V_P^b$$

Or

$$V_S = a + b \times V_P$$

Or

$$V_P = 1.16 \times V_S + 1.36$$

Where:

- ✓ V_S represents the shear wave velocity.
- ✓ V_P denotes compressional wave velocity.
- ✓ a and b are constants that depend on the type and region of rocks being analyzed.

To determine the reliability of the computed shear sonic (Vs), I employed the Castagna equation across the entire log, from top to bottom, and derived the Vs values (referred to as Vs from Castagna). For this computation, I exclusively utilized the actual acquired Vp and density data, with the Vs values being determined solely through the Castagna equation.

7.8 AVO/AVA Modelling

AVO, which stands for Amplitude Variation with Offset, is also referred as AVA (Amplitude Variation with Angle) because it is based on the relationship between the angle of incidence and the reflection coefficient (Amplitude Variations with Offset (AVO) - AAPG Wiki, n.d.). AVO modeling is a geophysical technique utilized to simulate the propagation of seismic waves as they travel beneath the Earth's surface across geological formations. It helps in predicting how the amplitude of seismic reflections varies with changes in the angle of incidence or offset, which is vital for characterizing subsurface properties (Castagna, 1993).

Geophysicists can gain insights into rock properties, such as porosity, density, and rigidity, as well as the fluid content (whether it contains water, oil, or gas, and in what proportions) by studying how the amplitude of the reflection changes with offset. Specifically, certain AVO responses are indicative of gas-bearing sands, which can be a target for drilling (Talib et al., 2020).

In this research two distinct methodologies employed for the computation of Vs, namely the Castagna equation and a machine learning-driven multi-regression technique. AVO modelling facilitates the evaluation and comparison of the Vs values acquired from both methods. Through the application of AVO modelling, synthetic seismic responses were generated using the Vs values derived from both approaches. Results, presented below, demonstrate that the Vs values obtained from the machine learning-based approach consistently provide better results compared to those from the Castagna equation. AVO modelling helps confirm this by demonstrating that the synthetic seismic responses generated using Vs values from the machine learning method exhibit more pronounced responses. validating the superiority of this approach.

7.8.1 Amplitude Versus Angle (AVA) gathers

Amplitude Versus Offset (AVO) gathers form as a result of variations in the reflection's amplitude of seismic waves at different incidence angles or offsets. In these gathers, each trace represents a seismic recording corresponding to a specific source-receiver offset or angle. Through the analysis of amplitude variations within these traces, geophysicists can deduce the possible existence of hydrocarbons and subsequently determine strategic drilling locations for exploration or production wells. Certain subsurface conditions cause noticeable changes in the reflection coefficient or amplitudes with increasing offset. For instance, gas-bearing sands often lead to a significant AVO response. This is because the contrast in certain rock properties, like density and velocity, between gas-bearing and surrounding rocks is distinct. Gas-bearing sands often produce stronger reflectivity at far offsets compared to near offsets, which can be seen as a brightening or increase in amplitude with offset in the AVO gather. By integrating the predicted Vs into AVO analysis, one can enhance the ability to detect and characterize gas-bearing sands (An & Lu, 2018).

7.8.2 AVA Gathers-Castagna

This research aims to assess the reliability of computed shear sonic data by incorporating Castagna-derived shear velocity (Vs) values into the Amplitude Versus Angle (AVA) model. The AVA analysis is a critical technique in the exploration of subsurface geology and reservoir characterization, relying on fundamental parameters such as compressional velocity (Vp), shear velocity (Vs), and density (RHOB) (Lu et al., 2018). These logs were employed to create a synthetic AVA gather. As illustrated in Figure 7.5, there's an observed amplitude dimming effect at higher offsets or higher angles.

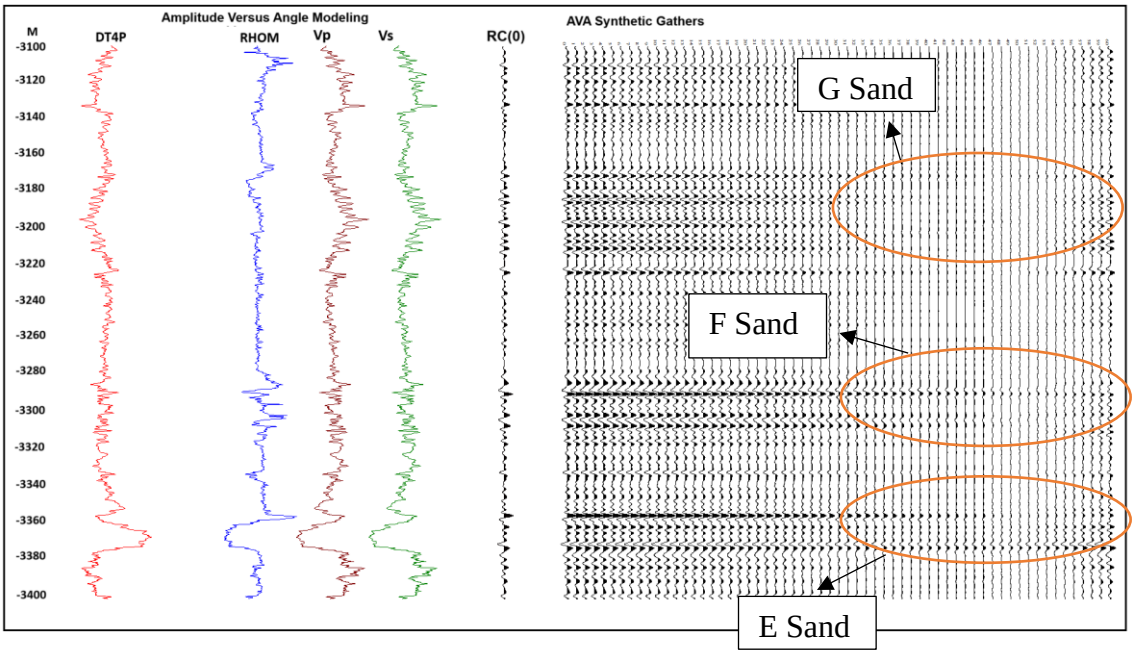

Figure 7.5 AVA Synthetic-gathers generated from shear sonic (Vs) computed by Castagna equation, shows dimming effect highlighted by circles.

As evident from the above Figure 7.5, when implementing AVO using the Castagna equation, a dimming effect becomes noticeable. This dimming effect could impact the interpretation of subsurface properties and potentially lead to mischaracterizations of reservoirs. Additionally, no AVO anomalies are detected at far angles or offsets. Further investigation is needed to understand the underlying causes of

this dimming effect and to determine if adjustments or corrections are necessary when utilizing Castagna-derived Vs values in AVA analysis.

7.8.3 AVA Gathers-Machine Learning

This research focuses on validating the accuracy of computed shear sonic values by integrating shear velocity (Vs) values derived from a ML-based multi regression algorithm into the Amplitude Versus Angle (AVA) synthetic gathers. The study aims to identify the presence of gas sands, particularly in the G, F, and E sand intervals, by analyzing AVA effects at steeper angles/offsets.. As illustrated in Figure 7.6, the amplitudes appear more pronounced at higher angles/offsets, and an AVO anomaly is clearly observed.

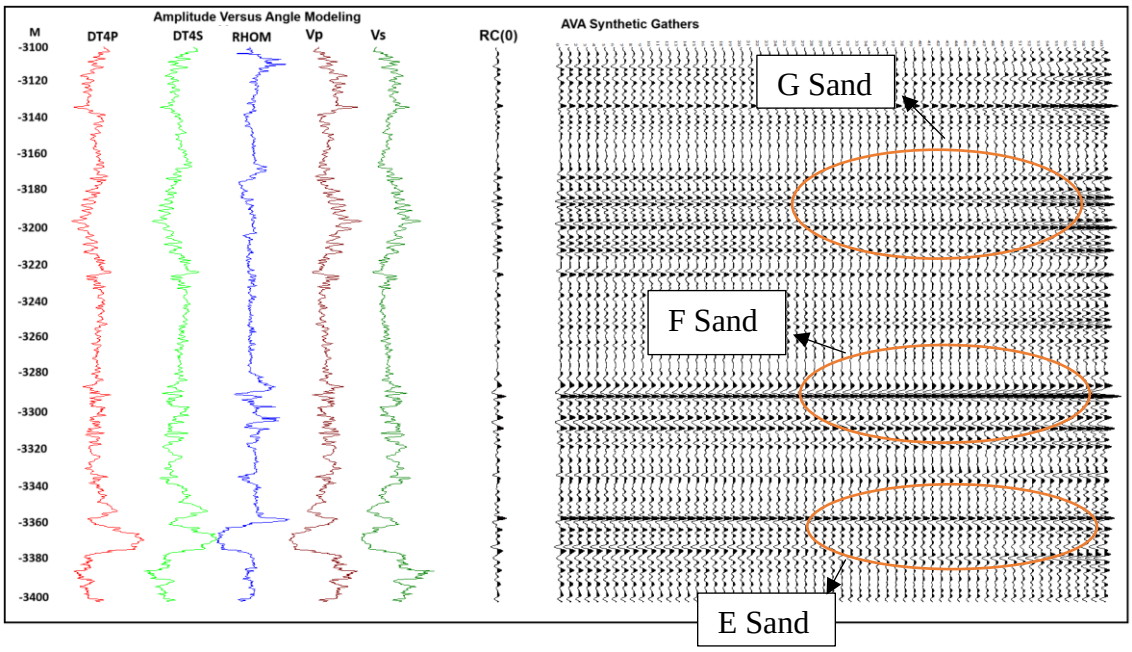

Figure 7.6 AVA effect at steeper angles, highlighting the presence of G, F and E gas sands.

Results

Figure 7.6 shows the AVA effect at far angles, with red-highlighted circles indicating the presence of G, F, and E sand intervals, which have been chosen as the

horizons of interest for my research. Several convincing reasons lead to the presumption that these regions contain Gas Sands.

Firstly, prior petrophysical analyses and inversion results have also indicated the presence of gas sands in the area. Moreover, Kadanwari is a well-known Gas-rich field, lending further validity to this indication. Furthermore, Gas sands tend to exhibit distinctive seismic responses due to their lower density and higher compressibility compared to surrounding rock formations. The selection of a far angle set at 60 degrees is significant as it yields the most optimal outcomes for detecting AVO anomalies associated with gas-bearing sands in this context. Gas-filled reservoirs typically manifest as conspicuous amplitude anomalies within seismic data at this specific angle due to their strong impedance contrast with adjacent rock formations (Lu et al., 2018).

From the results of AVO modeling, we can identify the presence of gas sands. Furthermore, this modeling validates the shear sonic values computed through multi-regression techniques. In contrast, shear sonic values calculated using Castagna's equation proved to be unreliable, as they did not produce any AVO anomalies. On the other hand, when employing machine learning algorithms to compute shear sonic values, we observed AVO anomalies, confirming their reliability. Therefore, shear sonic values derived from machine learning prove to be more reliable and yield superior results compared to those obtained from the Castagna equation.

7.9 Facies Modeling

Facies modeling is a method for identifying and classifying various rock types or "facies" based on their geophysical features. Facies analysis based on cross-plots is a globally recognized and essential methodology for effectively characterizing hydrocarbon reservoirs and other lithologies based on their respective log responses (Rahimi & Riahi, 2022).

This research utilizes three cross plots to delineate shale, shaly sand, and clean sands by analyzing log data obtained from the Kadanwari-03 well. The common techniques employed for facies modeling based on cross plots include establishing polygon boundaries and utilizing cluster analysis. In this investigation, the polygon

method based on clusters is employed for facies modeling. For this research, the facies modeling is carried out using the polygon clustering method by employing the kriging algorithm.

- **Polygon clustering method**

Kriging algorithm of machine learning is employed to estimate the value of a random field, such as facies, at a location where there are no direct observations, using data collected from nearby locations. This approach involves the identification of patterns or clusters representing various rock types through cross-plots. After recognizing patterns on the cross plots, polygons can be drawn around these clusters. Any data point located within a particular cluster is then categorized as belonging to the facies associated with that polygon. This essentially forms a boundary around data points that exhibit similar logging properties and are presumed to belong to the same rock type.

When the polygon cluster method is combined with Kriging, it involves utilizing the polygons created on the cross plots as a reference for determining facies types. Subsequently, Kriging is applied to model the spatial distribution of these facies' types within the reservoir. This integrated approach allows for a more comprehensive understanding of the facies distribution in the reservoir, enhancing the accuracy of predictions at unobserved locations.

7.9.1 Vp versus Vs Cross plot

In facies modeling, Vp and Vs curves derived from well logs or geophysical data play a pivotal role. These curves represent the variations in acoustic and shear wave velocities as a function of depth within the subsurface. Vp represents the velocity at which seismic compressional waves propagate through geological formations, while Vs signifies the speed of shear waves, which move perpendicular to the direction of wave propagation. The process typically involves creating a cross-plot by directly comparing the Vp and Vs curves. This allows for a direct visualization of how these velocities relate to each other, which can reveal distinct patterns or trends indicative of three geological facies as shown in Figure 7.7.

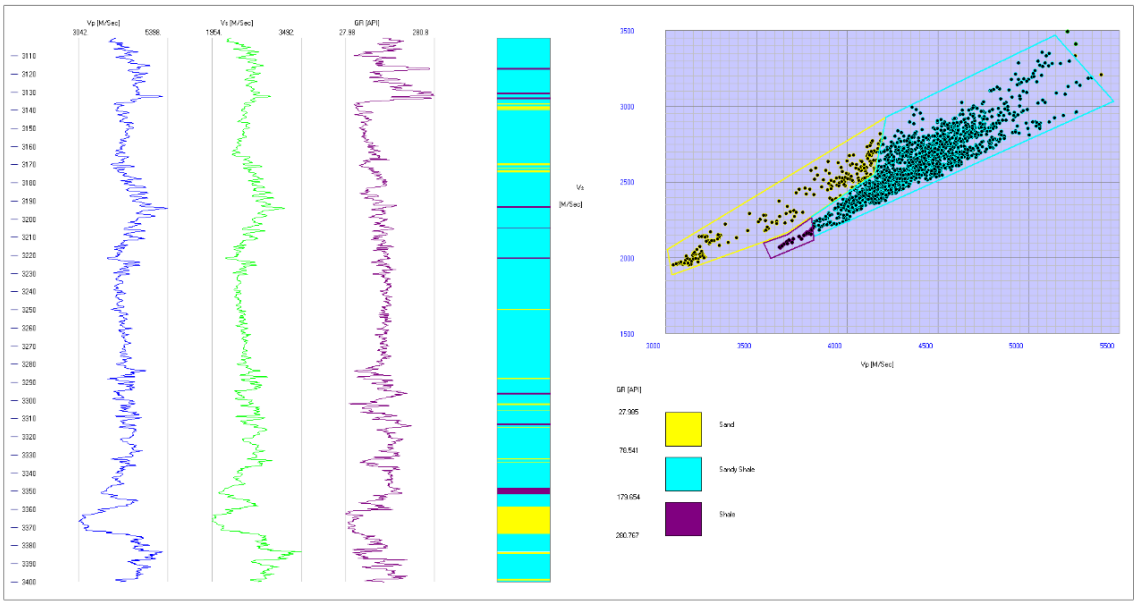

Figure 7.7 Crossplot of Vp vs. Vs from the Kadanwari-03 well within the depth interval of 3110 to 3400 meters.

To construct the cross-plot (as illustrated in Figure 7.7), the Kriging algorithm is employed to identify clusters of data points. This algorithm's details are explained in a previous section. The Gamma Ray (GR) log is employed as a benchmark automatically to establish a baseline for distinguishing between sand (26-78 API), shaly sand (79- 179 API) and shale (180-280API) by evaluating their responses in terms of Vp and Vs. Consequently, distinct colors are assigned to these lithologies based on the corresponding GR values, allowing for the color-coding of individual data points on the Vp vs. Vs cross plot. This color-coding provides a visual representation that helps identify and differentiate lithological variations and patterns.

Results

Figure 7.7 displays the Vp vs. Vs cross-plot, highlighting the presence of three distinct facies: clean sand (yellow), shale (purple), and shaly sand (cyan). These facies are recognized based on their unique clustering patterns within the cross-plot.

1. **Clean Sand:** Clean sand facies, characterized by a relatively low clay content and higher porosity, cluster in an area of the plot where both Vp and Vs values are comparatively lower (Anderton, 1985).

2. **Shale:** Shale, known for its relatively high clay content, tends to cluster in the region of the plot characterized by high Vp values and Vs values. In this region, Vp (P-wave velocity) values are notably higher than Vs (S-wave velocity) values (Michelena et al., 2009)..

3. **Shaly Sand:** Shaly sand, an intermediate lithology, clusters between shale and clean sands on the cross-plot due to its properties falling between those of shale and clean sand (El-Sayed, 2020).

Vp vs. Vs cross plot offers a powerful tool for reservoir characterization by enabling the identification and spatial distribution modeling of various rock facies based on their seismic velocities.

7.9.2 Vp & Density Cross plot

In facies modeling, Vp and density curves derived from well logs or geophysical data play a key role. Different lithologies have different physical qualities, and their responses on a Vp vs. RHOB cross plot may help identify them, as seen in Figure 7.8 below. As previously stated before, Vp is used to determine the propagation velocity of compressional waves (primary waves). It is affected by the compaction, fluid content, porosity, and rock lithology. Density, also known as RHOB, is a measurement that quantifies the bulk density or mass per unit volume of a rock. The rock's mineral composition, porosity, and the type of fluid filling the pores all have an influence on it.

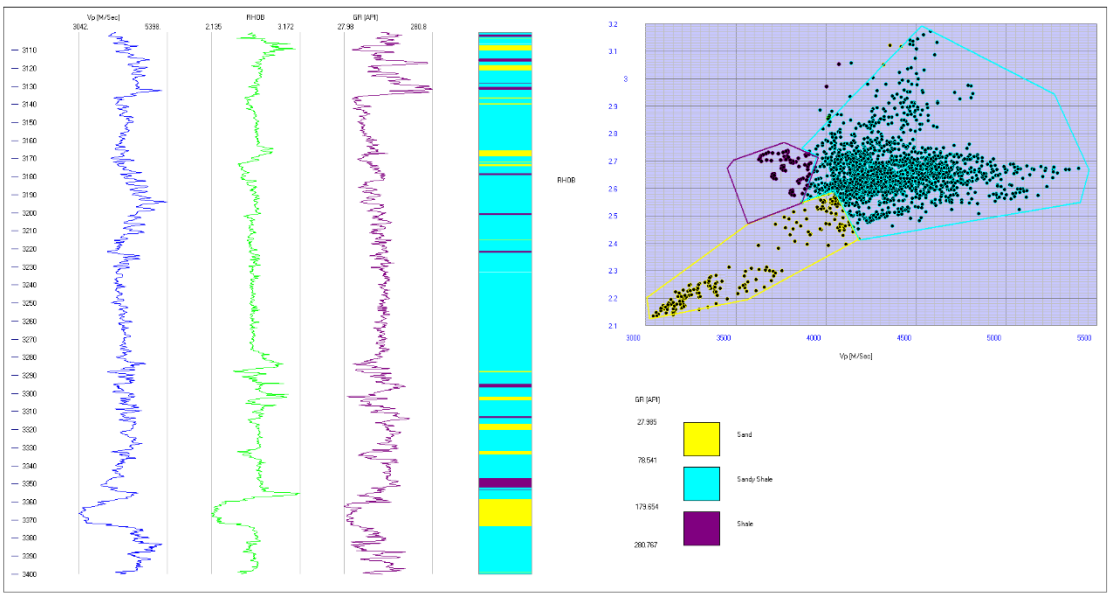

Figure 7.8 Crossplot of Vp vs. RHOB from the Kadanwari-03 well within the depth interval of 3110 to 3400 meters.

To construct the cross-plot (as illustrated in Figure 7.8), the Kriging algorithm is employed to identify clusters of data points. This algorithm's details are explained in a previous section. The Gamma Ray (GR) log employed as a benchmark automatically to establish a baseline for distinguishing between sand (26-78 API), shaly sand (79- 179 API) and shale (180-280API) by evaluating their responses in terms of Vp and RHOB. Consequently, distinct colors are assigned to these lithologies based on the corresponding GR values, allowing for the color-coding of individual data points on the Vp vs. RHOB cross plot. This color-coding provides a visual representation that helps identify and differentiate lithological variations and patterns.

Results

Figure 7.8 displays the Vp vs. Density cross-plot, highlighting the presence of three distinct facies: clean sand (yellow), shale (purple), and shaly sand (cyan). These facies are recognized based on their unique clustering patterns within the cross-plot.

1. **Clean Sand**: Clean sand facies appear in regions characterized by lower RHOB values and higher Vp values. These sands are typically water-saturated and exhibit these characteristics on the cross plot (Anderton, 1985).
2. **Shale**: Shale facies cluster in regions with moderate to high RHOB values and relatively low Vp values. Shales are known for their higher density and lower compressional wave velocity, which are reflected in this plot (Michelena et al., 2009)..
3. **Shaly Sand**: Shaly sand facies, falling between clean sands and shales on the cross plot, exhibit intermediate density and Vp values. These formations are a mix of clean sand and shale and display this characteristic on the plot (El-Sayed, 2020).

Understanding how various lithologies behave on a Vp vs. RHOB (bulk density) cross plot can be immensely valuable in the process of reservoir characterization. Over time,

and when combined with additional logs or data resources, enables geoscientists to detect lithological changes, pinpoint hydrocarbon-rich zones, and discern other essential reservoir features, improving reservoir assessment accuracy more correctly. Moreover, the Vp vs. RHOB cross plot serves as a means to validate and corroborate the outcomes derived from previous crossplot analyses, further bolstering the reliability of the findings.

7.9.3 Vs & Density Cross plot

In facies modeling, Vs and density curves derived from well logs or geophysical data play a crucial role. The relationship between shear wave velocity (Vs) and bulk density (RHOB) in different rock types is an important factor to consider when interpreting lithology. Distinct trends can be observed on a Vs versus RHOB cross plot, aiding in their differentiation, as depicted in Figure 7.9 below.

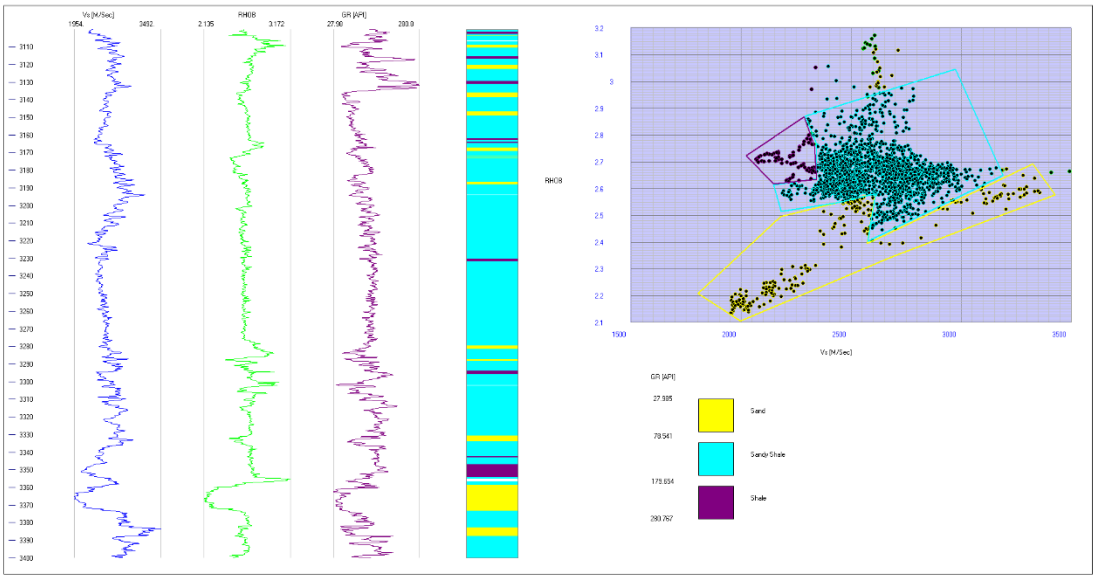

Figure 7.9. Crossplot of Vs vs. RHOB from the Kadanwari-03 well within the depth interval of 3110 to 3400 meters.

To construct the cross-plot (as illustrated in Figure 7.8), the Kriging algorithm is employed to identify clusters of data points. This algorithm's details are explained in a previous section. The Gamma Ray (GR) log is employed as a benchmark automatically

to establish a baseline for distinguishing between sand (26-78 API), shaly sand (79- 179 API) and shale (180-280API) by evaluating their responses in terms of Vs and RHOB. Consequently, distinct colors are assigned to these lithologies based on the corresponding GR values, allowing for the color-coding of individual data points on the Vs and RHOB cross plot. This color-coding provides a visual representation that helps identify and differentiate lithological variations and patterns.

Results

Figure 7.9 displays the Vs vs. Density cross-plot, highlighting the presence of three distinct facies: clean sand (yellow), shale (purple), and shaly sand (cyan). These facies are recognized based on their unique clustering patterns within the cross-plot.

1. **Clean Sand**: . Clean, water-saturated sands will appear in regions with higher Vs and lower RHOB values. Gas-bearing sands will show a noticeable decrease in Vs, but RHOB may not drop as drastically as it does in the Vs vs. RHOB relationship (Anderton, 1985).
2. **Shale**: Shale facies cluster in regions with moderate to high RHOB values and relatively low Vs values. Shales are known for their higher density and lower compressional wave velocity, which are reflected in this plot (Michelena et al., 2009).
3. **Shaly Sand**: Shaly sands exhibit Vs values that lie between the ranges observed for clean sands and shales, with their bulk density generally higher than clean sands but typically lower than pure shale. These shaly sands are positioned in an intermediate zone, falling between the defined regions for shales and clean sands (El-Sayed, 2020).

The Vs (shear wave velocity) vs. RHOB (bulk density) cross plot is important in geophysics and petrophysics because it provides insight into rock characteristics, which aids in lithological differentiation and fluid content determination.

7.10 Result and Discussion

In this research, a machine learning-based multi-regression approach was employed to calculate shear sonic velocity (Vs), resulting in significantly improved prediction accuracy compared to Vs values obtained through the Castagna equation. To validate the reliability of this approach, the AVA forward modeling algorithm was utilized with Vs values obtained from both methods. The study reveals the superiority of shear sonic values derived from machine learning techniques over those obtained from the Castagna equation. The presence of a dimming effect observed in the synthetic AVA gathers when using the Castagna equation suggests potential limitations in its accuracy. The research article (Suleymanov et al., 2023) validates the results by employing machine learning to predict elastic parameters while integrating rock physics parameters.

Furthermore, the research extends its findings by employing a machine learning-based Kriging algorithm for facies modeling. The study conducted by Zare et al., 2020 corroborated the findings by employing a machine learning-driven kriging algorithm to categorize the clusters into distinct facies. This modeling effort successfully categorizes the challenging-to-distinguish thin sand and shale layers within the Lower Goru Formation into three distinct groups: sand, shale, and shaly sand. The results validate that utilizing various cross-plots yields consistent classifications of facies. This validation is of paramount importance, as it refines drilling strategies, enhances insights into reservoir behavior, and improves hydrocarbon recovery processes.

The combined use of machine learning for Vs calculation and facies modeling, as demonstrated in this study, offers a comprehensive approach to subsurface characterization and reservoir exploration. Experts can effectively differentiate between different rock types and accurately determine the presence of hydrocarbons. This, in turn, significantly enhances overall reservoir management and production operations, emphasizing the critical role of advanced computational methods in improving the accuracy and reliability of geophysical data analysis and interpretation (An & Lu, 2018).

CHAPTER 8

GEOMECHANICS WITH AUTOMATED PRE-CONDITIONING OF PETROPHYSICAL LOGS USING MACHINE LEARNING

8.1 Geomechanics

Geomechanics is the study of the investigation of how subsurface rock formations deform or experience structural failure due to variations in stress, pressure, and temperature and it is becoming more important in the industry of oil and gas exploration (Busetti, 2019). Geomechanics is the theoretical and practical study of how geological materials behave mechanically. Its application involves mitigating risks and maximizing benefits associated with the mechanical instability of reservoirs and nearby geological formations due to activities linked to oil and gas exploration and extraction. These activities encompass processes like well drilling, hydraulic fracturing, gas or water injection, and resource depletion. The primary objective is to anticipate the occurrence of such instabilities, ultimately leading to risk reduction (Haq, 2019).

Reservoir geomechanical parameters are calculated to understand the mechanical behavior of subsurface rock formations, which is important for optimizing drilling, completion, and production strategies in the oil and gas sector. This information is used for stress analysis, hydraulic fracturing design, reservoir modeling, wellbore stability, subsidence prediction, environmental risk assessment, resource estimate, well location, and overall operational safety, assuring efficient and sustainable hydrocarbon production.

8.2 Reservoir geomechanics parameters

Pore pressure refers to the pressure exerted on fluids within the pore spaces of a rock formation. Pore pressure information plays a crucial role in enhancing our understanding of various aspects during exploration activities. This includes gaining

insights into the shape of the basin, the durability of traps, the routes taken by hydrocarbons during migration, and how pressure is distributed across geological formations. In addition, pore pressure data is helpful in identifying faults that effectively seal and those that may have leaks. By utilizing this data, drilling risks can be reduced by applying appropriate mud weight and optimizing casing design, which ensures effective control of the wellbore (Khan et al., 2017). The pressure experienced at a certain depth, known as **overburden** or lithostatic pressure, or vector stress, results from the cumulative weight of both the layers of material above a specific stratigraphic level and the pore fluids contained within those layers. The force exerted on the solid rock structure is referred to as **vertical effective stress.** This effective stress determines the degree of compression inside rocks, and a reduction in this stress leads to the development of overpressure conditions. The **fracture gradient** refers to the minimum pressure needed to induce or propagate fractures in a rock at a particular depth. It relies on factors such as rock strength, in-situ stress, and pore pressure. Pore pressure and fracture gradients have multiple applications in reservoir geomechanics, including maintaining wellbore stability, implementing hydraulic fracturing operations, and managing reservoir compaction (Tosaya, 1982; Khan et al., 2017).

8.3 Artificial Neural Network (ANN)

The Artificial Neural Network (ANN) is a machine-learning model or a computational system inspired by the functioning of neurons in the human brain. It consists of a vast number of neurons organized into different layers, each with specific functions (Shi et al., 2016). An ANN architecture generally comprises three fundamental layers: the input layer, hidden layers, and output layer. The ANN can be trained using various algorithms, but the back-propagation algorithm, often referred to as the BP algorithm, is the most frequently used. The objective of the **backpropagation** algorithm is to optimize the weights of a neural network to enable it to effectively learn the mapping of arbitrary inputs to corresponding outputs (Syed et al., 2022). I intend to utilize the backpropagation algorithm in machine learning to produce my outcomes. The provided Figure 8.1 depicts a basic ANN:

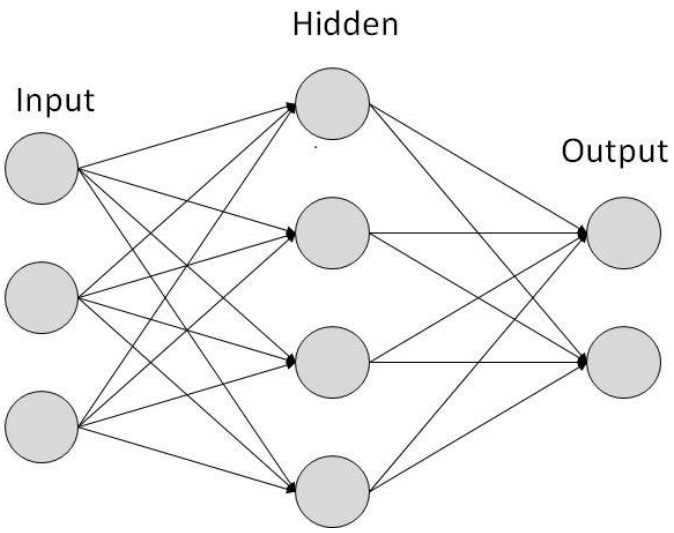

Figure 8.1 Basic Artificial Neural Network procedure

In the conventional approach, the input typically includes 4-5 logs: the gamma log, neutron porosity (NPHI), bulk density (RHOB), and compressional (DT) and shear (DTS) sonic logs. These logs are employed for the purpose of my analysis. The hidden layers utilize weight training sets to effectively train various algorithms. The output layer is responsible for providing the outcome. In my scenario, the objective is to identify and distinguish shale, sand, & tight sand, while also assessing the properties related to reservoir geomechanics.

This chapter explores the integration of machine learning techniques to compute geomechanical properties through automated preconditioning of petrophysical logs. This chapter presents three distinct workflows aimed at using machine learning algorithms for the preprocessing and conditioning of well log data, which are subsequently used as inputs to evaluate critical geomechanical properties including overburden stress, overburden stress gradient, vertical effective stress, pore pressure, pore pressure gradient, and fracture gradient.

8.4 Layer boundaries (1st Workflow)

The layer boundaries (i.e., sand, shale) are delineated by the outcome of the initial workflow. The complete process of this initial workflow is illustrated in Figure 8.2.

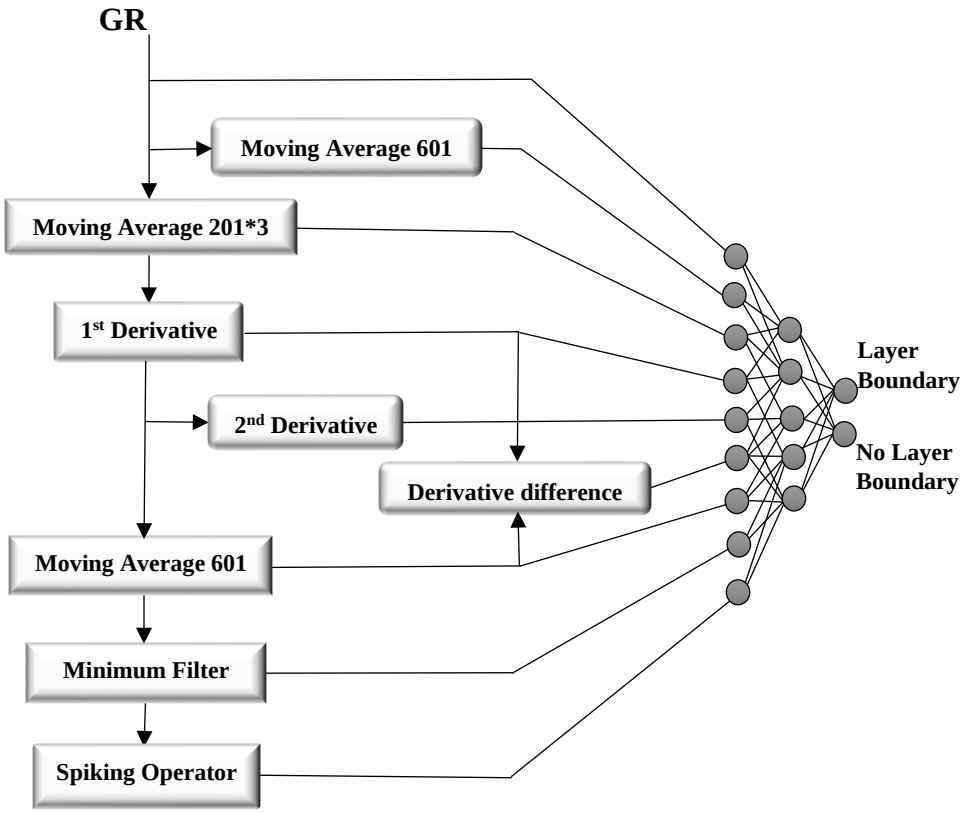

Figure 8.2 First workflow to delineate Layer Boundaries.

The first workflow focuses on employing machine learning models to accurately identify and classify the boundaries of sand and shale intervals within the logged section. This classification is essential for a comprehensive understanding of the stratigraphic heterogeneity and provides valuable insights for further evaluations of geomechanical properties.

The script of this initial workflow is shown in Annexure A, and the results derived from this script are displayed in Figure 8.3.

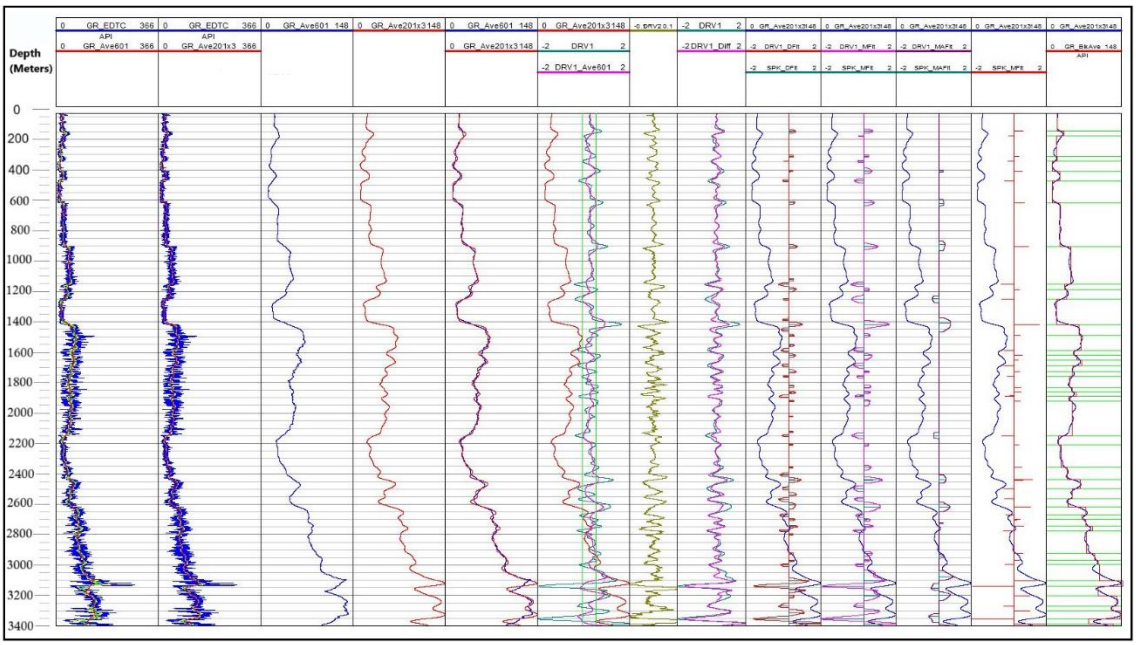

Figure 8.3 Outcome of first workflow to delineate Layer Boundaries

8.4.1 Methodology and Explanation

The first step is to take the single gamma ray log as an input log. Through the utilization of diverse algorithms, a range of modified logs is derived from this original GR log. The initial track named GR_EDTC features the original log-in marked by blue color. The name "GR_EDTC" is the original one instead of just "GR," because it was modified to eliminate glitches after its initial acquisition. The scale of the original GR log is 0 to 366. The first algorithm which is applied to the GR log is the Moving average on 601 samples. This moving average is labeled in red color as “GR_ Ave601” and is superimposed on an original log with the same scale displayed in the 1st track. In the third track GR_ Ave601 is displayed independently in blue color. The scale limit has been reduced from 366 to 148 in order to enhance its visibility. In moving Average on 601 samples means the neural network calculates the average of 300 samples both before and after the central value of 601. This resulting average is assigned to the central number. Afterward, it advances one step downward and this procedure is repeated until it computes the average of all the samples within the log. I have taken the average to somewhat smooth out the curve. Even within GR_Ave601, there are still some fluctuations that persist in the log data. Hence, following the experimentation with various moving averages on distinct samples, I decided to employ an iteration of moving

averages of 201 samples to the GR_Ave 601 log. Since it would be doing less smoothing, therefore, it would be applied 3 times to the original log. This moving average is denoted in red color as “GR_ Ave201*3”. Using the identical scale, it is superimposed onto the original log and depicted in the 2nd track. In the fourth track GR_ Ave201*3 is displayed independently in red color. The scale limit has been reduced from 366 to 148 to improve its visibility.

The basic aim of this method is to pre-train the log data into the neural network. This is essential because the original log exhibits significant fluctuations. By employing moving averages, it becomes relatively more manageable for the neural network to address these fluctuations to a certain degree. In simple words, I tried to simplify the log data before training it in machine learning. In the fifth track, the moving average of 601 (GR_ Ave601) and moving average of 201 (GR_ Ave201*3), are superimposed on each other within the same track. The blue one is a moving average of 601 and the red one is a moving average of 201. As we can see in the track, specifically within a depth range of 1600 to 2000, the log response of GR_Ave601 exhibits more pronounced oscillations or minute vibrations, implying a substantial presence of noise. This leads to the loss of distinct layer signatures. Whereas, within the same interval, the moving average of 201*3 retains the layer signatures in the form of vibrations or oscillations. From the comparison, it can be inferred that the moving average of 201 (GR_ Ave201*3) is a much better choice to be used as an input into the neural network. Moving forward, I proceed to compute the first-order derivative of GR_ Ave201*3, denoted as "DRV1". In the sixth track, DRV1 is represented in green color with a scale of -2 to 2 along with GR_Ave201*3 in red. This first-order derivative, DRV1, functions as an edge detector operator. Additionally, I also computed a second-order derivative of GR_ Ave201*3 designated as "DRV2" displayed in the seventh track, represented by an olive-green color. However, it was observed that the second derivative exhibited an excessive amount of noise or fluctuations. Consequently, upon evaluating the results, the decision was made to utilize the DRV1 instead. Whenever lithology or formation changes, naturally log trend also changes. In such instances, the first-order derivative (DRV1) will interpret this alteration as a boundary change, producing a peak in its output. When there is a significant change in the GR_ Ave201*3 value, DRV1 will exhibit a more pronounced peak in its output. Conversely, if the GR_ Ave201*3 log parameter is decreasing, DRV1 will generate a negative peak in its output. Next, I applied a moving average of 601 on the first-order

derivative (DRV1) to smoothen the curve. This curve is labeled as “DRV1_Ave601” in the same sixth track distinguished by pink color.

Sometimes within the layer, there are minor variations and when a derivative is applied to such regions, these subtle changes are slightly magnified. As a result, the derivative might misinterpret these enhanced changes as variations in lithology, which may not be the case. To address this issue, two threshold lines are drawn on the first-order derivate (DRV1). These threshold lines are determined based on 5% to 10% of the maximum and minimum values of DRV1. Values falling below this 10% threshold line are filtered out, while those exceeding this threshold are interpreted as indications of variation or change. These lines will serve as a reference for the implementation of the minimum filter, the details of which will be explained in the following discussion. In the eighth track, the difference between DRV1 and its moving average, DRV1_Ave601 and presented as "DRV1_Diff," which is distinguished by pink shade. DRV1_Diff is overlaid on DRV1 within the same track. Notably, DRV1 exhibits pronounced peaks, while its difference from its moving average DRV1_Diff represents comparatively lower values than DRV1. This difference is calculated to mitigate the heightened peaks to a certain degree. Next, a difference filter is applied on DRV1_Diff and labeled in red color as “DRV1_DFlt” and displayed in the ninth track. GR_ Ave201*3 log is displayed in the same track just for reference. Within the DRV1_Diff log, a specific value range is defined, which is based on the 5-10% of the minimum and maximum values of the log. The difference filter diminishes all values of DRV1_Diff that lie within this defined range to zero. Values exceeding this defined range are interpreted as peaks and troughs. In the same track, the spiking operator, which is named “SPK_DFlt”, is applied to the difference filter. The spiking operator scans this difference filter trace. Whenever the non-zero values are encountered, it attempts to identify the location of the highest sample in the case of a peak, marked this specific sample, and rest of the values are set to zero. Similarly, when dealing with a trough, the spiking operator locates the position of the lowest value, marks that particular sample, and resets the remaining values to zero. As a result of this process, the presence of a maximum or minimum value is indicated by the appearance of a spike in the results.

Since the difference filter (DRV1_DFlt) picks unnecessary information especially minor changes arising from various factors. To address this concern, a minimum filter is introduced and applied directly to DRV1. The Minimum filter is displayed as

“DRV1_MFlt” highlighted in green, in the tenth track along with GR_ Ave201*3 log as a reference. As previously discussed, two threshold lines are drawn on the first-order derivative (DRV1) in the sixth track. These lines are generated using the range of 5% to 10% of the maximum and minimum values within DRV1. Values that are lower than this 10% threshold line or values that fluctuate between these reference lines are set to zero, whereas values exceeding this threshold are detected as peaks. As the minimum filter operates much better than the difference filter, it has been chosen for further utilization. The spiking operator was then applied to the minimum filter, which is shown as "SPK_MFlt" in the same 10^{th} track, as indicated by green. The spiking operator examines the minimum filter trace. When it finds a non-zero value, it keeps it until the next zero value occurs. The operator chooses the highest non-zero number and marks it as a single peak spike while setting all other values to zero. On the other hand, in cases when values decrease, the spiking operator identifies the lowest non-zero value and classifies it as a trough spike, subsequently resetting all other values to zero. The minimum filter and the spiking operator have also been implemented on the first-order derivative moving average (DRV1_Ave601) as well, as evident in the 11th track. Here, “DRV1_MAFlt” is represented in purple and “SPK_MAFlt” in green. However, it is noticeable that this approach results in an additional smoothing curve, causing the loss of the distinct layer variation signature. As a result, it is decided not to proceed with this approach. As the spiking operator applied to the minimum filter yields better results, therefore spiking minimum operator along with the moving average of GR 201*3 have been displayed in the 12^{th} track, ensuring clear differentiation of lithological contrasts. All these spikes symbolize boundary points where there are transitions between layers or where lithology has been changing. Positive spikes signify an increase in log values, whereas negative spikes indicate a decrease in log values.

8.4.2 Result & Discussion

Finally, all these logs have been fed to the neural network, which gives us results in the form of markers that distinguish boundaries between different geological layers. In the final log, the GR moving average of 201*3 is displayed. Over this moving average curve, spikes have been designated as markers, signifying the interfaces between distinct layers. Within each interval, the block average of gamma-ray symbolized as

"GR_BkAve", has been carried out, illustrating the block-like response of the GR between interfaces.

The Boundary Identification Workflow employs machine learning models to precisely identify and classify sand and shale boundaries within logged sections. This aids in comprehending stratigraphic heterogeneity and offers insights for further geomechanical property assessments.

All this script is written in Python using the K-tron GeoStudio Petrolib library. The source code of this script is given in Annexure A.

8.5 Volume of shale (2nd Workflow)

The color-based block average of the shale volume is established based on the results derived from the second workflow. The procedure of this secondary workflow is shown in Figure 8.4.

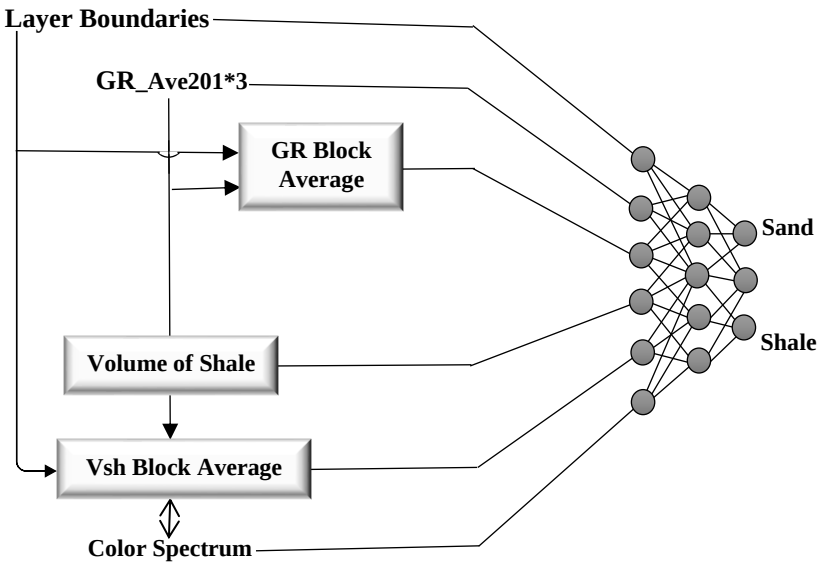

Figure 8.4 Second workflow for computation of block averages for the volume of shale.

The aim of the previous workflow is to mark boundaries. The second workflow is focused on the computation of block averages for the volume of shale, a key parameter in the characterization of rock formations. By employing artificial neural networks or

machine learning techniques, we can automatically classify or interpret sand, shale, and intermediate layers.

This workflow has been developed using the K-tron Petrolib library and the script of this source code has been shown in annexure B and the results derived from this script are displayed in Figure 8.5.

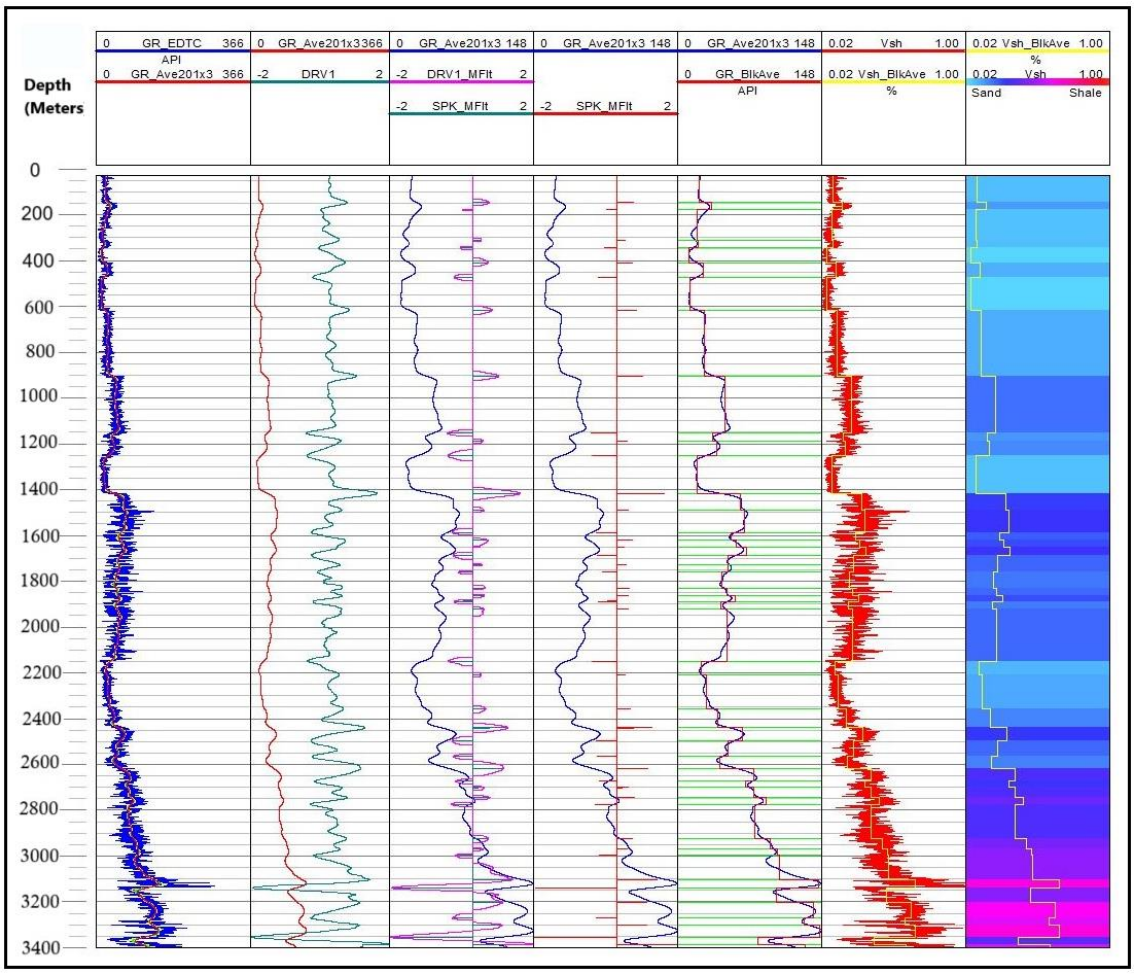

Figure 8.5 Second workflow for computation of block averages for the volume of shale.

8.5.1 Methodology and Explanation

In the concluding stage of the previous workflow, the interfaces demarcating the boundaries between the geological layers have been identified through the utilization of machine learning techniques. The initial five log tracks remain consistent with those

utilized in the previous workflow. In the very first track, the original GR_EDTC log is displayed along with GR_Ave201*3 which is superimposed on it. Both have a scale limit from 0 to 366. Moving to the second track, GR_Ave2013 is presented in red, accompanied by the first-order derivative DRV1 in green. On the third track, GR_Ave201*3 is shown in blue with a scale range of 0 to 148, the first-order derivative's minimum filter, DRV1_MFlt, is represented in pink, and the spiking operator overlaid on this minimum filter, SPK_MFlt, is displayed in green. The fourth track depicts GR_Ave2013 with a scale reduced from 0 to 148 and SPK_MFlt displayed separately. Moving on to the fifth track, it presents the block average of GR (GR_BlkAve) together with GR_Ave2013 for reference. As we previously discussed, the neural network identified interface boundaries, and within these boundaries, a block average has been carried out. With these layer markers, neural network computes the volume of shale from the gamma-ray. Furthermore, within these same boundaries, a block-averaging algorithm is applied to the shale volume. In the sixth track, the shale volume, represented as "Vsh," is highlighted in red with a scale range of 0.2 to 1.

8.5.2 Result & Discussion

In the concluding phase, machine learning uses a color spectrum to visualize this block average of shale volume (Vsh_BlkAve), to clearly identify the layers of shale, sand, and tight sand. This color representation is demonstrated in the seventh and final track. A blue shade indicates sand, transitioning to a darker blue as the shale component increases. A pink color designates shale.

The Volume of Shale Computation Workflow concentrates on calculating block averages for the volume of shale, a critical parameter for characterizing rock formations. It relies on artificial neural networks or machine learning techniques to automatically categorize sand, shale, and intermediate layers. These computed values then serve as inputs for evaluating reservoir geomechanical properties.

All this script is written in Python using the K-tron GeoStudio Petrolib library. The source code of this script is given in Annexure B.

8.6 Reservoir Geomechanics Properties (3rd Workflow)

Geomechanical parameters are derived through the utilization of the third workflow procedure, as illustrated in Figure 8.6.

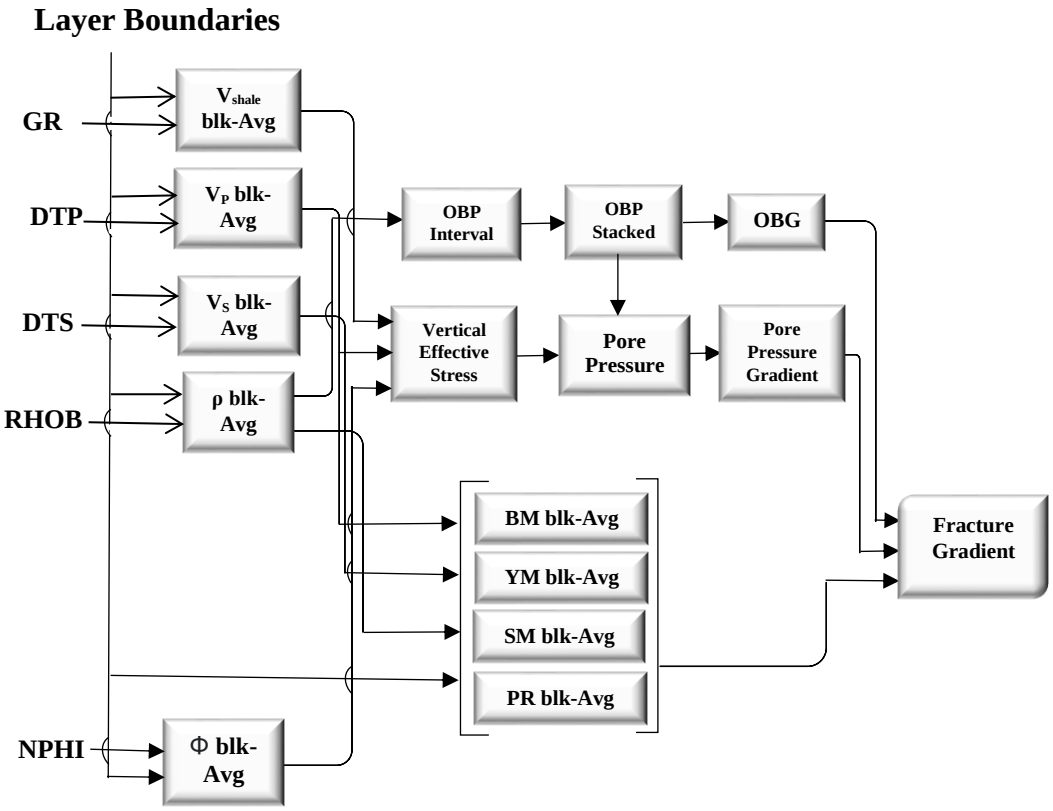

Figure 8.6 Final workflow to derive Geomechanical parameters.

This workflow focuses on the computation of essential rock physics parameters, which are subsequently used as inputs into machine learning to evaluate reservoir geomechanical properties, including overburden stress, overburden stress gradient, pore pressure, pore pressure gradient, and fracture gradient. These outputs, generated through systematic and automated workflows, provide a robust and streamlined approach to geomechanical evaluation, enabling more efficient decisions in various applications, such as wellbore stability analysis, hydraulic fracturing design, and reservoir management.

The script of this workflow has been designed by a fellow research student, Saman Fatima (2023), and I am utilizing this framework to produce results of geomechanical properties for Kadanwari-03 well, as shown in Figure 8.7.

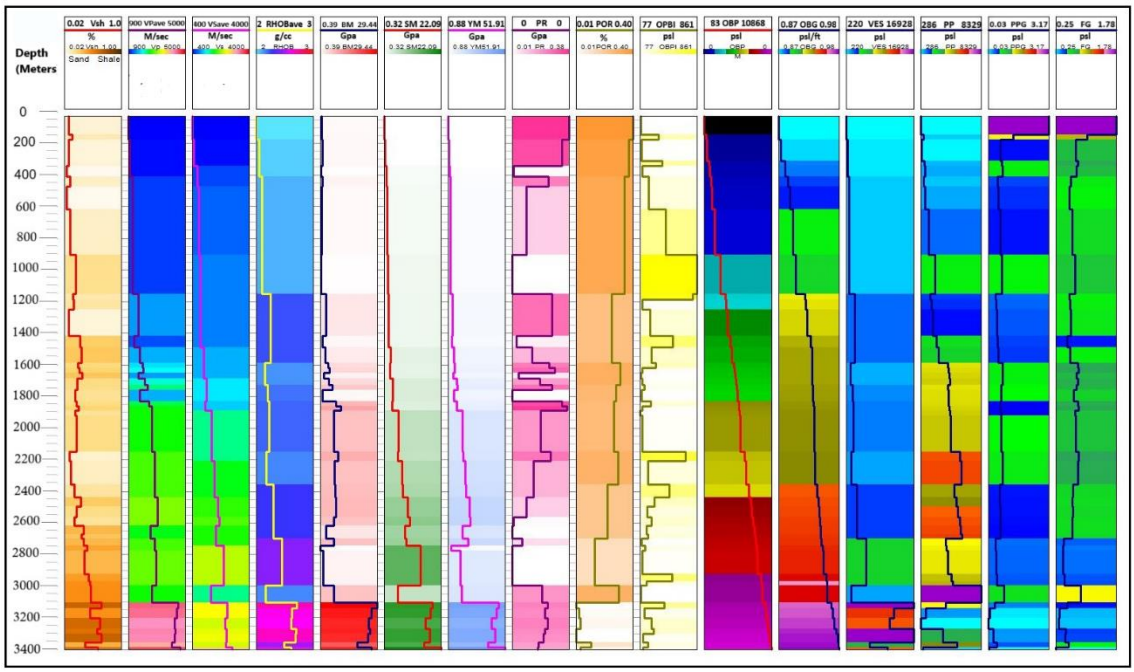

Figure 8.7 Results of final workflow to derive Geomechanical parameters.

8.6.1 Methodology and Explanation

In this third and final procedure, the layer boundaries derived from the conclusion of the first workflow are used, together with the color spectrum-based representation of the block average Volume of shale from the second workflow, taking these as inputs into machine learning or artificial neural network that initiates the third workflow. In the first track, the volume of the shale (Vsh) log is illustrated with a color gradient changing from skin to light brown, indicating a transition from sand to a more shaley composition, and dark brown indicates the presence of shale. This color gradient visually aids in distinguishing between sand and shale formations in the log. Utilizing identical markers, the compressional velocity (Vp) is computed from the sonic log (DTP). Subsequently, its block average within each interval is calculated and exhibited in the second track, employing a rainbow color spectrum. Similarly, the shear velocity (Vs) is determined from the shear sonic log (DTS). Its block average within each interval is calculated and presented in the third track, using the same rainbow color spectrum as before. In the fourth track, the average density log (RHOB_Ave) is calculated using Gardner's equation

(Gardner, 1974). After computing its block average, the data is visually represented using a color spectrum that transitions from blue to pink and red.

Next, some rock physics parameters in the block average form have been computed from these three logs (Vp, Vs, RHOB). The very first one is the Bulk Modulus (BM) which is displayed in the fifth track with a color gradient spanning from white to red. The next one is the Shear Modulus (SM), which is displayed in the sixth track with a color spectrum ranging from white to green. Subsequently, the Young Modulus (YM) is displayed in the seventh section, featuring a color spectrum that spans from white to blue. Moving on, the Poisson Ratio (PR) is presented in the eighth track, employing a color spectrum that varies from white to pink. If the NPHI log is accessible, the mean block average of the Porosity log (POR) is calculated and exhibited in the ninth track using a color range that transitions from white to brown. If the NPHI log is unavailable, this porosity log can also be computed using the density log. At this point, all the necessary parameters for the computation of reservoir geomechanical properties have been determined.

- **Computed Geomechanical parameters**

The first geomechanical parameter is Overburden pressure (OBPI), also referred to as vertical stress or lithological pressure, which is determined using the density log through the application of the Bryant & Bell method (Bryant, 1986). Subsequently, the block average of overburden pressure is computed for each interval and displayed in the tenth track using a color spectrum that transitions from white to yellow. Overburden pressure refers to the stress exerted on a rock due to the load of the rock and soil layers above it. When this overburden pressure becomes greater than the pressure of fluids within the rock's pore spaces, it leads to the compression of the formation (Richard, 2015).

Moving to the eleventh track, stacked overburden pressure with depth (OBP) from top to bottom is computed and displayed by using 6 color spectra. As evident in the provided Figure 6.6, there's a continuous increase in the stacked overburden pressure from the top layer to the bottom, signifying that the pressure is increasing as more layers are added. In the subsequent twelfth track, the overburden gradient (OBG) has been derived from the stacked overburden pressure. The gradient represents the rate of change. The resulting overburden gradient is then displayed using a color spectrum consisting of five distinct colors. In the 13th track, the vertical effective stress (VES) has been calculated for each

interval using the Bowers method (Bowers, 1994), based on the interval velocity. The resulting blocky average of VES values is visually represented in the 13th track using a color spectrum comprising five distinct colors: blue, green, yellow, red, and pink. There are two prevalent methods for computing vertical effective stress (VES)

- The Bowers method (Bowers.1994).
- The Athy method (Athy,1930).

In the Athy method, vertical effective stress (VES) is derived with the assistance of porosity, whereas in the Bowers method, interval velocity is utilized. In my scenario, I employed the Bowers method. In the next track another geomechanics parameter, Pore Pressure (PP) has been computed from an over-pressure gradient by using the Terzaghi method (Terzaghi,1943), and its blocky average is illustrated in the 14^{th} track, utilizing a color spectrum comprising five distinct colors: blue, green, yellow, red, and pink. The rate of change of pore pressure is called the Pore Pressure Gradient (PPG). The block-averaged curve of the pore pressure gradient is visualized in the 15th track using the same color spectrum of five colors. In the final track, the last component of geomechanics, the Fracture gradient (FG) has been computed from the Eaton method (Eaton,1969). Fracture gradient is computed with the help of the overburden gradient, Poisson's ratio, and pore pressure gradient. The graphical representation of the fracture gradient curve is illustrated in the last track, employing the consistent 5-color spectrum as before.

8.6.2 Result & Discussion

The Geomechanical Property Evaluation Workflow utilizes machine learning, drawing on inputs from the previous workflow, to assess vital geomechanical properties, including overburden stress, overburden stress gradient, vertical effective stress, pore pressure, pore pressure gradient, and fracture gradient. These properties are fundamental in assessing the mechanical behavior of subsurface formations and are indispensable for ensuring the safety and stability of drilling operations and reservoir management. While conducting drilling operations, it is essential to establish the appropriate mud weight. Pore pressure gradient determines the lowest weight limitations in mud designs, whereas fracture gradient defines the maximum weight limits. Mud weight at any given depth should be greater than the pore pressure but less than the Fracture pressure/gradient.

Pore pressure gradient determines the lowest weight limitations in mud designs, whereas fracture gradient defines the maximum weight limits. Pressure is exerted on the borehole wall by formation fluids. In order to prevent fluid intrusion and wellbore failure it is imperative that the mud weight is consistently maintained at a level higher than the pore pressure. In contrast, when the mud weight exceeds the fracture gradient of the formation, it results in the fracturing of the wellbore, thereby causing the release of mud into the formation (Khan, 2017).

8.7 Conclusion & Discussion

The findings of Sacrey and Sierra (2020) involve the estimation of potential reservoir quantities using geobodies that have been analyzed through unsupervised machine learning classifications. Another study conducted by Nath and colleagues in 2022 utilized advanced machine learning techniques, including Bi-directional Long Short-Term Memory (Bi-LSTM) and Random Forest (RF) algorithms, to forecast the sonic characteristics of rock. The primary objective was to estimate and assess the geomechanical attributes of the prospective unconventional formation located in the Permian Basin of West Texas. To fill the gap thiis chapter delves into the utilization of supervised machine learning (SML) methodologies to calculate geomechanical characteristics by automating the conditioning of petrophysical logs. It presents three distinct procedural frameworks that uses machine learning algorithms to preprocess and refine well log data, which are subsequently utilized as inputs to assess critical geomechanical attributes.

The first boundary identification workflow focuses on the precise identification and classification of sand and shale boundaries within the logged section, facilitated by SM learning models. This classification is vital for gaining a comprehensive understanding of stratigraphic heterogeneity and provides valuable insights for further geomechanical property evaluations. The second volume of shale computation workflow concentrates on computing block averages for shale volume, a critical parameter in rock formation characterization. By employing artificial neural networks or supervised machine learning techniques, it becomes possible to automatically classify or interpret sand, shale, and intermediate layers. The geomechanical properties evaluation workflow revolves around the computation of essential rock physics parameters, which are

subsequently fed into machine learning models to evaluate reservoir geomechanical properties, including overburden stress, overburden stress gradient, vertical effective stress, pore pressure, pore pressure gradient, and fracture gradient.

A comprehensive understanding of geomechanical characteristics is required to accurately predict the distribution of stress inside a reservoir. The acquisition of these parameters is crucial for the investigation of wellbore stability, the planning of hydraulic fracturing operations, and the modelling of reservoir behavior. It aids in the prevention of problems including subsidence, casing failure, and wellbore collapse.

CONCLUSIONS

The study area was analyzed using geophysical methods and techniques such as seismic interpretation, petrophysical evaluation, seismic attribute assessment, seismic inversion, machine learning-driven Vs prediction, and its subsequent validation, facies examination, and geomechanics. The outcomes from these techniques are as follows:

1. The 3D Seismic Structural Interpretation of the Kadanwari area reveals an extensional regime dominated with horst and graben structures. Time & Depth Contour mapping of the G, F, and E sands of the Lower Goru Formation shows that the G and E sands possess shallower time and depth regions compared to the F sand. This suggests that the G and E sands have a higher potential for hydrocarbon accumulation. Moreover, the central zone between the two major faults has been pinpointed as a promising location for future drilling.

2. Petrophysical studies of wells Kadanwari-10 and Kadanwari-11 show distinct reservoirs in the Lower Goru's G, F, and E sands. Hydrocarbon saturations are highest in E Sand (85-95%), followed by G Sand (60-75%) and F sand (up to 50%). Thus, E and G sands are notably more productive than F sand in the Kadanwari Gas field

3. The Model-Based Inversion technique has been applied to analyze the 3D seismic cube of the Kadanwari area, focusing on the variations in impedance. The P-impedance inverted model indicates that the G and E sand formations exhibit lower impedance values compared to the F sand. These results align with findings from petrophysical analysis and seismic interpretation, verifying their precision. Thus, the G and E sand formations are identified as producing reservoirs.

4. Seismic attributes, especially Spectral Decomposition, aid in detecting thin bed strata of G, F, and E sands, by increasing frequency sub-bands. The pronounced

reflection strength from the broad red areas on the sections signifies amplitude anomalies, which further validates the boundary delineation provided by the Instantaneous Amplitude attribute for the Lower Goru G and E sands. This suggests that these sands could be potential reservoir formations in the Kadanwari region. The Instantaneous Phase attribute effectively identifies disruptions from faults and showcases the lateral continuity of the Lower Goru Sands.

5. A machine learning-driven multi-regression method is utilized for the computation of shear sonic velocity (Vs), significantly enhancing predictive accuracy when contrasted with Vs values derived from the Castagna equation. To evaluate the reliability of this approach, the AVO forward modeling algorithm was applied to Vs values obtained from both methodologies. The outcomes demonstrated that the Vs calculations derived from the machine learning approach consistently outperformed those obtained from the Castagna equation, particularly in detecting gas anomalies at higher angles. In the Lower Indus Basin, thin sand and shale layers are hard to distinguish manually, so machine learning was used for facies modeling to classify them into three distinct groups and compute separate equations for them.

6. Machine learning techniques are used to compute geomechanical properties through automated preconditioning of petrophysical logs by using three specialized workflows. The first workflow focuses on employing machine learning models to accurately identify and classify the boundaries of sand and shale intervals. The second workflow is devoted to the computation of block averages for the volume of shale. The third and final workflow delves into the calculation of essential rock physics & other fundamental parameters, which serve as inputs to evaluate vital reservoir geomechanical properties (including overburden stress, overburden stress gradient, pore pressure, pore pressure gradient, and fracture gradient) distinguished by unique color spectrums.

REFERENCES

Ahmad, N., Spadini, G., Palekar, A. and Subhani, M.A., (2007). Porosity prediction using 3D seismic inversion Kadanwari Gas Field, Pakistan. Pak J Hydrocarb Res, 17, pp.95-102.

Ahmad, N., & Chaudhry, S. (2002). Kadanwari Gas Field, Pakistan: a disappointment turns into an attractive development opportunity. Petroleum Geoscience, 8(4), 307–316. https://doi.org/10.1144/petgeo.8.4.307

Ahmed, N., Khalid, P., Ghazi, S., & Anwar, A. W. (2015). AVO forward modeling and attributes analysis for fluid's identification: a case study. Acta Geodaetica et Geophysica, 50(4), 377-390.

Ahmed, S., Monalisa, M., Hussain, M., & Khan, Z. (2022). Supervised machine learning for predicting shear sonic log (DTS) and volumes of petrophysical and elastic attributes, Kadanwari Gas Field, Pakistan. Frontiers in Earth Science, 10. https://doi.org/10.3389/feart.2022.919130.

Ahmad, M. N., & Rowell, P. (2012). Application of spectral decomposition and seismic attributes to understand the structure and distribution of sand reservoirs within Tertiary rift basins of the Gulf of Thailand. *The Leading Edge*, *31*(6), 630–634. https://doi.org/10.1190/tle31060630.1.

Ali, A., Alves, T. M., & Amin, Y. (2022). Integrated geophysical analysis of the Sembar Formation, Central Indus Basin, as an unconventional resource. Journal of Natural Gas Science and Engineering, 101, 104507. https://doi.org/10.1016/j.jngse.2022.104507

Ali, M.; Khan, M.J.; Ali, M.; Iftikhar, S (2021). Petrophysical analysis of well logs for reservoir evaluation: A case study of "Kadanwari"

Ali, N., Chen, J., Fu, X., Hussain, W., Ali, M., Iqbal, S.M., Anees, A., Hussain, M., Rashid, M. & Thanh, H.V., published, (2023), "Classification of reservoir quality using unsupervised machine learning and cluster analysis: Example from

Kadanwari gas field, SE Pakistan," Geosystems and Geoenvironment, 2(1), 100123.

Ali, N., Chen, J., Fu, X., Hussain, W., Ali, M., Iqbal, S. M., ... & Thanh, H. V. (2023). Cla ssification of reservoir quality using unsupervised machine learning and cluster analysis: Example from Kadanwari gas field, SE Pakistan. Geosystems and Geoenvironment, 2(1), 100123.

Archie, G. E. (1942). The electrical resistivity log as an aid in determining some reservoir characteristics. Transactions of the American Institute of Mining, Metallurigical and Petroleum Engineers 146: 54-62p.

Ashraf, U., Zhu, P., Yasin, Q., Anees, A., Imraz, M., Mangi, H. N., & Shakeel, S. (2019). Classification of reservoir facies using well log and 3D seismic attributes for prospect evaluation and field development: A case study of Sawan gas field, Pakistan. Journal of Petroleum Science and Engineering, 175, 338-351.

Athy, L.F. (1930) Density, Porosity and Compaction of Sedimentary Rocks. Bulletin of the American Association of Petroleum Geologists (AAPG Bulletin), 14, 1-24.

Austin, O. E., Onyekuru Smauel, I., Ebuka, A. O., & Abdulrazzaq, Z. T. (2018). Application of model-based inversion technique in a field in the coastal swamp depobelt, Niger Delta. International Journal of Advanced Geosciences, 6(1), 122-126.

Badely ME. (1985). Practical seismic interpretation. Boston (VI): Publication International human resources development corporation; p. 266.

Busetti, S. (2019, October 1). Guest Editorial: Five Innovation Themes for Integrated Geomechanics Technology. Journal of Petroleum Technology, 71(10), 14–15. https://doi.org/10.2118/1019-0014-jpt

Badely, M.E., 1988. Practical Seismic Interpretation, IHRDC Publishers, Boston. 266p.

Barclay, F., Bruun, A., Rasmussen, K. B., Alfaro, J. C., Cooke, A., Cooke, D., ... & Roberts, R. (2008). Seismic inversion: Reading between the lines. Oilfield Review, 20(1), 42-63.

Bryant, W et al. (1986): Geotechnical properties of Intraslope Basin sediments, Gulf of Mexico, Deep Sea Drilling Project Leg 96, Site 619. In: Bouma, AH; Coleman, JM; Meyer, AW; et al. (eds.), Initial Reports of the Deep Sea Drilling Project, Washington (U.S. Govt. Printing Office), 96, 819-824

Barnes, A. E. (2001). Seismic attributes in your facies. CSEG recorder, 26(7), 41-47.

Bashir, Y., Faisal, M.A., Biswas, A., Ali, S.H., Imran, Q.S., Siddiqui, N.A., Ehsan, M., (2021). Seismic expression of miocene carbonate platform and reservoir characterization through geophysical approach: application in central Luconia, offshore Malaysia. Journal of Petroleum Exploration and Production 11, 1533 - 1544.

Berger, A., Gier, S., and Krois, P. (2009). Porosity-preserving chlorite cements in shallow-marine volcaniclastic sandstones: Evidence from Cretaceous sandstones of the Sawan gas field, Pakistan. Bulletin 93 (5), 595–615. doi:10.

Bowers, G. L. (1995). Pore pressure estimation from velocity data: Accounting for overpressure mechanisms besides under compaction. SPE Drilling & Completion, 10(02), 89-95.

Castagna, J. P., Batzle, M. L., and Eastwood, R. L. (1985). Relationships between compressional-wave and shear-wave velocities in clastic silicate rocks. geophysics 50 (4), 571–581. doi:10.1190/1.1441933.

Castagna, J. P. (1993). Petrophysical imaging using AVO. The Leading Edge, 12(3), 172–178. https://doi.org/10.1190/1.1436939.

Chopra, S., & Marfurt, K. J. (2005). Seismic attributes—A historical perspective. Geophysics, 70(5), 3SO-28SO.

Chopra, S., & Pruden, D. (2003). Multiattribute seismic analysis on AVO-derived parameters—A case study. The Leading Edge, 22(10), 998-1002.

Coffeen, J. A. (1984). Interpreting seismic data.

Cooke, D., & Cant, J. (2010). Model-based Seismic Inversion: Comparing deterministic and probabilistic approaches.

Dalvand, M. J., & Falahat, R. (2021). A new rock physics model to estimate shear velocity log. Journal of Petroleum Science and Engineering, 196, 107697. https://doi.org/10.1016/j.petrol.2020.107697.

Davarpanah, M., & Akhlaghi, J. (2017, June). 3D seismic interpretation and structural analysis of Z Field, eastern Persian Gulf. *The Leading Edge*, *36*(6), 474–479. https://doi.org/10.1190/tle36060474.1

Das, B., Chatterjee, R., Singha, D. K., & Kumar, R. (2017). Post-stack seismic inversion and attribute analysis in shallow offshore of Krishna-Godavari basin, India. Journal of the Geological Society of India, 90(1), 32–40. https://doi.org/10.1007/s12594-017-0661-4

DelMonte, A.A., Luoni, F., Baruffini, L. and Ahmad, N., (2009), September. Evaluating Net Sand Thickness on Seismically Thin Reservoirs–An Integrated Approach Applied to Kadanwari Gas field . In EAGE/SEG Research Workshop-Frequency Attenuation and Resolution of Seismic Data 2009.

Dewett, D. T., Pigott, J. D., & Marfurt, K. J. (2021, August 1). A review of seismic attribute taxonomies, discussion of their historical use, and presentation of a seismic attribute communication framework using data analysis concepts. *Interpretation*, *9*(3), B39–B64. https://doi.org/10.1190/int-2020-0222.1

Djebbar, T., E.C.Donaldson., (2004) "Petrophysics"; Gulf Professional publishing, P.229, 247

Eaton, B. A. (1969). Fracture gradient prediction and its application in oilfield operations. Journal of petroleum technology, 21(10), 1353-1360.

El-Sayed, A. S. (2020). A novel method to improve water saturation in shaly sand reservoirs using wireline logs. Journal of Petroleum Science and Engineering, 185, 106602. https://doi.org/10.1016/j.petrol.2019.106602

Ehsan, M., Gu, H., Akhtar, M. M., Abbasi, S. S., & Ehsan, U. (2018). A geological study of reservoir formations and exploratory good depths statistical analysis in Sindh Province, Southern Lower Indus Basin, Pakistan. Kuwait Journal of Science, 45.

Gas field, middle Indus basin, Pakistan. Arab. J. Geosci. (2019), 12, 1–12.

Gardner, G.H.F., Gardner, L.W., and Gregory, A.R., (1974), Formation velocity and density – the diagnostic basics for stratigraphic traps: Geophysics, 39, 770-780.

GeolOil - How to calculate Shale Volume from Gamma Ray: Larionov, Clavier and Stieber models. (n.d.). https://www.geoloil.com/VshModels.php

Gupta, S., Wang, W., Hayek, S. S., Chan, L., Mathews, K. S., Melamed, M. L., ... & Modersitzki, F. (2021). Association between early treatment with tocilizumab and mortality among critically ill patients with COVID-19. JAMA internal medicine, 181(1), 41-51.

Haq, A. (2019). An Introduction to Geomechanics - GeoExpro. Available at from: https://geoexpro.com/an-introduction-to-geomechanics/.

Hossain, M. I. S., Woobaidullah, A. S. M., & Rahman, M. J. (2021, June). Reservoir characterization and identification of new prospect in Srikail gas field using

wireline and seismic data. Journal of Petroleum Exploration and Production Technology, 11(6), 2481–2495. https://doi.org/10.1007/s13202-021-01217-y

Hampson, D. P., Russell, B. H., & Bankhead, B. (2005). Simultaneous Inversion of Pre-stack Seismic Data SEG Technical Program Expanded Abstracts. Society of Exploration Geophysicists.Return to ref 2005 in article.

Jain, C., (2013), Effect of seismic wavelet phase on post stack inversion: In 10th Biennial Int. Conf. and Exposition, Kochi, pp. 410.

Kadri, I, B., 1995. Petroleum Geology of Pakistan. Pakistan Petroleum Ltd, Karachi.

Karim, S. U., Islam, M. D., Hossain, M. M., & Islam, A. M. (2016). Seismic reservoir characterization using model based post-stack seismic inversion: in case of fenchuganj gas field Bangladesh. Journal of the Japan Petroleum Institute, 59(6), 283–29.

Kazmi, A. H., and Jan, M. Q. (1997). Geology and tectonics of Pakistan. Oregon, USA: Graphic publishers.

Kazmi, A.H. and Abbasi, I.A. (2008) Stratigraphy and Historical Geology of Pakistan. Department and National Centre of Excellence in Geology, University of Peshawar, Pakistan, 524 p.

Kearey, P., Brooks, M. and Hill, I. (2002) An Introduction to Geophysical Exploration. Blackwell Science Ltd., Oxford.

Kemal, A., Balkwill, H.R., Stoakes, F.A., (1991). Indus Basin Hydrocarbons plays, International Petroleum Seminar on new directions and strategies for accelerating Petroleum Exploration and Production in Pakistan, 16-57.

Khan, K. A., Bangash, A. A., & Akhter, G. (2017). Raw seismic velocities aid predictions in mud program designs. Oil & Gas Journal, 115(11), 30-35.

Khan, K. A., & Akhter, G. (2015). Review of instantaneous, wavelet, and weighted seismic attributes along with a computational library. Arabian Journal of Geosciences, 9(1). https://doi.org/10.1007/s12517-015-2044-8.

Khan, U., Du, J., Hussain, S., Jiang, Z., Ali, S., Ali, I., ... & Zhang, B. (2022). Three-dimensional Structural Modeling (3D SM) and Joint Geophysical Characterization (JGC) of Hydrocarbon Reservoir: A Case Study of the Kadanwari Gas field in Middle Indus Basin (MIB), Southeastern Pakistan.

Khan, M., Nawaz, S., Shah, M., & Hasan, M. (2016, June). Interpreting Seismic Profiles in terms of Structure and Stratigraphy, an Example from Lower Indus Basin Pakistan. Universal Journal of Geoscience, 4(3), 62–71. https://doi.org/10.13189/ujg.2016.040302

Koson, S., Chenrai, P., & Choowong, M. (2014). Seismic attributes and their applications in seismic geomorphology. Bulletin of Earth Sciences of Thailand, 6(1), 1-9.

Lee, K., Yoo, D.G., McMechan, G.A., Hwang, N., and Lee, G.H., 2013, A twodimensional post-stack seismic inversion for acoustic impedance of gas and hydrate bearing deep-water sediments within the continental slope of the Ulleung Basin, east sea, Korea. TAO: Terrestrial, Atmospheric and Oceanic Sciences, v. 24, pp. 295.

Liu, S., Zhao, Y., and Wang, Z. (2021). Artificial intelligence method for shear wave travel time prediction considering reservoir geological continuity. Math. Problems Eng. 2021, 5520428–18. doi:10.1155/2021/5520428.

Margrave, G. F., Stewart, R. R., & Larsen, J. A. (2001). Joint PP and PS seismic inversion. The Leading Edge, 20(9), 1048-1052.

Maurya, S. P., & Sarkar, P. (2016). Comparison of post stack seismic inversion methods: a case study from Blackfoot Field, Canada. International Journal of Scientific and Engineering Research, 7(8), 1091-101.

Michelena, R. J., Godbey, K. S., & Angola, O. (2009). Constraining 3D facies modeling by seismic-derived facies probabilities: Example from the tight-gas Jonah Field. The Leading Edge, 28(12), 1470-1476.

Mohamed, A. K., Ghazala, H. H., & Mohamed, L. (2016). Integration between well logging and seismic reflection techniques for structural analysis and reservoir characterizations, Abu El Gharadig basin, Egypt. NRIAG Journal of Astronomy and Geophysics, 5(2), 362-379.

Nath, F., Asish, S. M., Ganta, D., Debi, H. R., Aguirre, G., & Aguirre, E. (2022). Artificial intelligence model in predicting geomechanical properties for shale Formation: A field case in Permian Basin. Energies, 15(22), 8752. https://doi.org/10.3390/en15228752

Nasir, O., Fall, M., Nguyen, T. S., & Evgin, E. (2011). Modelling of the hydro-mechanical response of sedimentary rocks of southern Ontario to past glaciations. Engineering Geology, 123(4), 271–287. https://doi.org/10.1016/j.enggeo.2011.07.008

Radwan, A. E., Wood, D. A., & Radwan, A. A. (2022). Machine learning and data-driven prediction of pore pressure from geophysical logs: A case study for the Mangahewa gas field, New Zealand. Journal of Rock Mechanics and Geotechnical Engineering, 14(6), 1799–1809. https://doi.org/10.1016/j.jrmge.2022.01.012.

Raza HA, Ali SM, RJPJoHR Ahmed (1990) Petroleum geology of Kirthar sub-basin and part of Kutch Basin 2(1):27–73

Rahimi, M., & Riahi, M. A. (2022, June). Reservoir facies classification based on random forest and geostatistics methods in an offshore oilfield. Journal of Applied Geophysics, 201, 104640. https://doi.org/10.1016/j.jappgeo.2022.104640.

Rider, M., (2002) The Geological Interpretation of Well Logs, Second Edition, 280p.

Rider, M. H. (1986). The geological interpretation of well logs. Glasgow [Strathclyde: Blackie].

Richard O. Baker, Harvey W. Yarranton, Jerry L. Jensen, (2015), "7 - Conventional Core Analysis–Rock Properties," Practical Reservoir Engineering and Characterization, pp. 197–237, Gulf Professional Publishing.

Russell, B. & Hampson, D. (1991). A comparison of post-stack seismic inversion methods. 61stAnnual International Meeting, SEG, Expanded Abstracts, 876–878.

Saman (2023), "3D Seismic Interpretation, Petrophysics And Machine Learning Based Quantitative Interpretation Of Gambat Latif Block Middle Indus Basin, Pakistan."

Schlumberger, (1974). Log Interpretation Principles. 1 st Edn., Schlumberger Education Services, Huston, TX., pp:230.

Senosy, A. H., Ewida, H. F., Soliman, H. A., & Ebraheem, M. O. (2020), "Petrophysical analysis of well logs data for identification and characterization of the main reservoir of Al Baraka Oil Field, Komombo Basin, Upper Egypt." SN Applied Sciences, 2(7),, 2020: 1-14.

Saif-Ur-Rehman, K. J., Mehmood, M. F., Shafiq, Z., and Jadoon, I. A. (2016). Structural styles and petroleum potential of Miano block, central Indus Basin, Pakistan. Ijg 7 (10), 1145–1155. doi:10.4236/ijg.2016.710086

Sheriff, R.E. and Geldart, L.P., (1995). Exploration seismology. Cambridge university press.

Shakir, U., Ali, A., Hussain, M., Azeem, T., & Bashir, L. (2021). Selection of sensitive Post-Stack and Pre-Stack seismic inversion attributes for improved

characterization of thin Gas-Bearing sands. Pure and Applied Geophysics, 179(1), 169–196. https://doi.org/10.1007/s00024-021-02900-1.

Seregey, F., (2007). Local Seismic Attributes. Geophysics, 72, A29-A33.

Stewart, S.A., (2012). Interpretation validation on vertically exaggerated reflection seismic sections. Journal of Structural Geology, 41 , pp.38-46

Shi, X., Liu, G., Cheng, Y., Yang, L., Jiang, H., Chen, L., Jiang, S., & Wang, J. (2016, September). Brittleness index prediction in shale gas reservoirs based on efficient network models. Journal of Natural Gas Science and Engineering, 35, 673–685. https://doi.org/10.1016/j.jngse.2016.09.009.

Suleymanov, V., El-Husseiny, A., Glatz, G., & Dvorkin, J. (2023). Rock physics and machine learning comparison: elastic properties prediction and scale dependency. Frontiers in Earth Science, 11, 1095252.

Sacrey, D., & Sierra, C. (2020). Systematic workflow for reservoir characterization in northwestern Colombia using multi-attribute classification. First Break, 38(3), 77–82. https://doi.org/10.3997/1365-2397.fb2020022

Syed, F. I., AlShamsi, A., Dahaghi, A. K., & Neghabhan, S. (2022, June). Application of ML & AI to model petrophysical and geomechanical properties of shale reservoirs – A systematic literature review. *Petroleum*, *8*(2), 158–166. https://doi.org/10.1016/j.petlm.2020.12.001

Taner, M. T., & Images, R. S. (2001). Seismic attributes: CSEG Recorder. Rock Solid Images, Houston, USA.

Tayyab, M. N., & Asim, S. (2017). Application of spectral decomposition for the detection of fluvial sand reservoirs, Indus Basin, SW Pakistan. Geosciences Journal, 21(4), 595-605.

Talib, M., Durrani, M. Z. A., Mathur, A., Bekti, R. P., & Ting, J. (2020, February). Integrated petrophysics and rock physics workflow validated by well to seismic tie and AVO modelling. In Fifth EAGE Workshop on Rock Physics (Vol. 2020, No. 1, pp. 1-5). European Association of Geoscientists & Engineers.

Terzaghi, K., "Theoretical soil mechanics," John Wiley and Sons Inc., 1943.

Tiab, D. and Donaldson (2004). Petrophysics: Theory and Practice of Measuring Reservoir Rock and Fluids Transport Properties. New York: Elsevier. Google Scholar.

Thomas, E., & Stieber, S. (1975). The Distribution Of Shale In Sandstones And Its Effect Upon Porosity. Thomas & Stieber. https://onepetro.org/SPWLAALS/proceedings/SPWLA-1975/All-SPWLA-1975/SPWLA-1975-T/20024

Tosaya, C.A., "Acoustical properties of clay-bearing rocks," PhD Dissertation, Stanford University Department of Geophysics, June 1982.

Veeken, P. C. H., & Da Silva, A. M. (2004). Seismic inversion methods and some of their constraints. First break, 22(6).

Wyllie, M.R.J., Gregory, A.R. and Gardner, L.W. (1958) An Experimental Investigation of Factors Affecting Elastic Wave Velocities in Porous Media. Geophysics, 23, 459-49. http://dx.doi.org/10.1190/1.1438493.

Wrona, T., Pan, I., Bell, R. E., Gawthorpe, R. L., Fossen, H., & Brune, S. (2021). 3D seismic interpretation with deep learning: A brief introduction. The Leading Edge, 40(7), 524-532.

Yilmaz, O., (2001).,Seismic Data Analysis: Processing ,Inversion and Interpretation of Seismic Data Vol. (1 & 2)., Society of Exploration Geophysicists.

Zhang, B., Tong, Y., Du, J., Hussain, S., Jiang, Z., Ali, S., Ali, I., Khan, M., & Khan, U. (2022). Three-Dimensional structural modeling (3D SM) and joint geophysical characterization (JGC) of hydrocarbon reservoir. Minerals, 12(3), 363. https://doi.org/10.3390/min12030363.

Zhang, R., & Deng, Z. (2018, November 1). A depth variant seismic wavelet extraction method for inversion of poststack depth-domain seismic data. GEOPHYSICS, 83(6), R569–R579. https://doi.org/10.1190/geo2017-0816.1

Zaigham, N.A. and Mallick, K.A. (2000) Prospect of Hydrocarbon Associated with Fossil-Rift Structures of the Southern Indus Basin, Pakistan. American Association of Petroleum Geologist AAPG Bulletin, 84, 1833-1848.

ANNEXURE A

picMain.Cls

```
DoEvents
pl.ReadLAS App.Path & "\Kadanwari-19.las"
ds# = pl.GetDepthStart()
de# = pl.GetDepthStop()

ss& = pl.GetSampleIndex(ds)
es& = pl.GetSampleIndex(de)
es& = pl.GetSampleIndex(3400) 'Forced Depth End
de# = pl.GetDepth(es) 'Forced Depth End

Xo% = 80
Xw# = 150
pl.DrawDepthScale picMain, 10, 150, 60, 750, ds, de, 50, 200, QBColor(7), QBColor(8), QBColor(0)
pl.DrawDepthGrid picMain, Xo, 150, 1340, 750, ds, de, 50, 200

gri% = pl.GetLogIndex("GR_EDTC")
pl.PutLogUnit gri, "API"

'--------------------Algo#1: Ave 601
pl.AllocateLogMemory "GRave1"
gra% = pl.GetLogIndex("GRave1")
pl.PutLogMin gra, pl.GetLogMin(gri)
pl.PutLogMax gra, pl.GetLogMax(gri)
pl.MovingAverage gri, gra, ss, es, 101

pl.AllocateLogMemory "GRave2"
gra% = pl.GetLogIndex("GRave2")
pl.PutLogMin gra, pl.GetLogMin(gri)
pl.PutLogMax gra, pl.GetLogMax(gri)
pl.MovingAverage gri, gra, ss, es, 301

pl.AllocateLogMemory "GR_Ave601"
gra% = pl.GetLogIndex("GR_Ave601")
```

```
pl.LogsMinMax
pl.PutLogMin gra, pl.GetLogMin(gra3)
pl.PutLogMax gra, pl.GetLogMax(gra3)
pl.DrawHeader picMain, Xo, 10, Xw, 130, 20, "GR_Ave601", QBColor(9), 3, 0
pl.DrawLog picMain, Xo, 150, Xw, 750, "GR_Ave601", ss, es, QBColor(9), 1, 0
pl.DrawTrackFrame picMain, Xo, 150, Xw, 750, 1

Xo% = Xo + Xw
Xw# = 135
pl.DrawHeader picMain, Xo, 10, Xw, 130, 20, "GR_Ave201x3", QBColor(12), 3, 0
pl.DrawLog picMain, Xo, 150, Xw, 750, "GR_Ave201x3", ss, es, QBColor(12), 1, 0
pl.DrawTrackFrame picMain, Xo, 150, Xw, 750, 1

Xo% = Xo + Xw
Xw# = 135
pl.DrawHeader picMain, Xo, 10, Xw, 130, 20, "GR_Ave601", QBColor(9), 3, 0
pl.DrawLog picMain, Xo, 150, Xw, 750, "GR_Ave601", ss, es, QBColor(9), 1, 0
pl.DrawLog picMain, Xo, 150, Xw, 750, "GR_Ave201x3", ss, es, QBColor(12), 1, 0
pl.DrawTrackFrame picMain, Xo, 150, Xw, 750, 1

'----------Slope Computation
'----1st Derivative
Xo% = Xo + Xw
Xw# = 135
pl.DrawHeader picMain, Xo, 10, Xw, 130, 20, "GR_Ave201x3", QBColor(12), 3, 0
pl.DrawLog picMain, Xo, 150, Xw, 750, "GR_Ave201x3", ss, es, QBColor(12), 1, 0

pl.AllocateLogMemory "DRV1"
pl.Slope gra3, drv1, ss, es
pl.LogsMinMax
'pl.PutLogMin drv1, -4 'Forced Log Min

pl.DrawHeader picMain, Xo, 10, Xw, 130, 50, "DRV1", QBColor(3), 3, 0
pl.DrawLog picMain, Xo, 150, Xw, 750, "DRV1", ss, es, QBColor(3), 1, 0
'----1st Derivative-Average
pl.AllocateLogMemory "DRV1_Ave601"
drv1a% = pl.GetLogIndex("DRV1_Ave601")
pl.MovingAverage drv1, drv1a, ss, es, 601
pl.LogsMinMax
```

```
pl.PutLogMin drv1a, pl.GetLogMin(drv1)
pl.PutLogMax drv1a, pl.GetLogMax(drv1)

pl.DrawHeader picMain, Xo, 10, Xw, 130, 80, "DRV1_Ave601", QBColor(13), 3, 0
pl.DrawLog picMain, Xo, 150, Xw, 750, "DRV1_Ave601", ss, es, QBColor(13), 1, 0
pl.DrawTrackFrame picMain, Xo, 150, Xw, 750, 1

xs! = pl.GetLogMin(drv1)
xe! = pl.GetLogMax(drv1)
PR! = 0.15
pl.SetGraphicsContext picMain, Xo, 150, Xw, 750, xs, xe, CSng(ds), CSng(de)
pl.DrawLine xe * PR, ds, xe * PR, de, QBColor(10), 1
pl.DrawLine xs * PR, ds, xs * PR, de, QBColor(10), 1
DoEvents

'----2nd Derivative
pl.AllocateLogMemory "DRV2"
drv2% = pl.GetLogIndex("DRV2")
pl.Slope drv1, drv2, ss, es
pl.LogsMinMax
pl.PutLogMin drv2, -0.1 'Forced Log Min
pl.PutLogMax drv2, 0.1 'Forced Log Min

Xo% = Xo + Xw
Xw# = 70
pl.DrawHeader picMain, Xo, 10, Xw, 130, 20, "DRV2", QBColor(6), 3, 0, , 1, 2.6
pl.DrawLog picMain, Xo, 150, Xw, 750, "DRV2", ss, es, QBColor(6), 1, 0
pl.DrawTrackFrame picMain, Xo, 150, Xw, 750, 1

'----1st Derivative-Average Difference
pl.AllocateLogMemory "DRV1_Diff"
drv1d% = pl.GetLogIndex("DRV1_Diff")
pl.LogMinMax "DRV1_Diff", ss, es
pl.PutLogMin drv1d, xs
pl.PutLogMax drv1d, xe

Xo% = Xo + Xw
Xw# = 100
pl.DrawHeader picMain, Xo, 10, Xw, 130, 20, "DRV1", QBColor(3), 3, 0
```

```
pl.DrawLog picMain, Xo, 150, Xw, 750, "DRV1", ss, es, QBColor(3), 1, 0
pl.DrawHeader picMain, Xo, 10, Xw, 130, 50, "DRV1_Diff", QBColor(13), 3, 0
pl.DrawLog picMain, Xo, 150, Xw, 750, "DRV1_Diff", ss, es, QBColor(13), 1, 0
pl.DrawTrackFrame picMain, Xo, 150, Xw, 750, 1

'----1st Derivative-Difference Filter
pl.AllocateLogMemory "DRV1_DFlt"
drv1f% = pl.GetLogIndex("DRV1_DFlt")
pl.FilterDifference drv1a, drv1, drv1f, ss, es, xs * 0.12, xe * 0.12
pl.PutLogMin drv1f, xs
pl.PutLogMax drv1f, xe

pl.AllocateLogMemory "SPK_DFlt"
spk1f% = pl.GetLogIndex("SPK_DFlt")
pl.Spike drv1f, spk1f, ss, es
pl.PutLogMin spk1f, xs
pl.PutLogMax spk1f, xe

Xo% = Xo + Xw
Xw# = 110
pl.DrawHeader picMain, Xo, 10, Xw, 130, 20, "GR_Ave201x3", QBColor(9), 3, 0, , , 2.6
pl.DrawLog picMain, Xo, 150, Xw, 750, "GR_Ave201x3", ss, es, QBColor(9), 1, 0
pl.DrawHeader picMain, Xo, 10, Xw, 130, 80, "SPK_DFlt", QBColor(3), 3, 0, , , 2.6
pl.DrawLog picMain, Xo, 150, Xw, 750, "SPK_DFlt", ss, es, QBColor(3), 1, 0
pl.DrawHeader picMain, Xo, 10, Xw, 130, 50, "DRV1_DFlt", QBColor(12), 3, 0, , , 2.6
pl.DrawLog picMain, Xo, 150, Xw, 750, "DRV1_DFlt", ss, es, QBColor(12), 1, 0
pl.DrawTrackFrame picMain, Xo, 150, Xw, 750, 1

'----1st Derivative-Minimum Filter
pl.AllocateLogMemory "DRV1_MFlt"
drv1m% = pl.GetLogIndex("DRV1_MFlt")
pl.FilterMinimum drv1, drv1m, ss, es, xs * 0.12, xe * 0.12
pl.PutLogMin drv1m, xs
pl.PutLogMax drv1m, xe

pl.AllocateLogMemory "SPK_MFlt"
spk1m% = pl.GetLogIndex("SPK_MFlt")
pl.Spike drv1m, spk1m, ss, es
pl.PutLogMin spk1m, xs
```

```
pl.PutLogMax spk1m, xe


pl.AllocateLogMemory "DRV1_MAFlt"
drv1ma% = pl.GetLogIndex("DRV1_MAFlt")
pl.FilterMinimum drv1a, drv1ma, ss, es, xs * 0.12, xe * 0.12
pl.PutLogMin drv1ma, xs
pl.PutLogMax drv1ma, xe


Xo% = Xo + Xw
Xw# = 110
pl.DrawHeader picMain, Xo, 10, Xw, 130, 20, "GR_Ave201x3", QBColor(9), 3, 0, , , 2.6
pl.DrawLog picMain, Xo, 150, Xw, 750, "GR_Ave201x3", ss, es, QBColor(9), 1, 0
pl.DrawHeader picMain, Xo, 10, Xw, 130, 80, "SPK_MFlt", QBColor(3), 3, 0, , , 2.6
pl.DrawLog picMain, Xo, 150, Xw, 750, "SPK_MFlt", ss, es, QBColor(3), 1, 0
pl.DrawHeader picMain, Xo, 10, Xw, 130, 50, "DRV1_MFlt", QBColor(13), 3, 0, , , 2.6
pl.DrawLog picMain, Xo, 150, Xw, 750, "DRV1_MFlt", ss, es, QBColor(13), 1, 0
pl.DrawTrackFrame picMain, Xo, 150, Xw, 750, 1
ReDim GRave!(NI), dp!(NI)
pl.BlockAverage gri, di(), NI, GRave()
pl.DrawFreeHeader picMain, Xo, 10, Xw, 130, 50, "GR_BlkAve", "API", pl.GetLogMin(gra3), pl.GetLogMax(gra3), QBColor(12),
3, , , , 2.6
pl.SetGraphicsContext picMain, Xo, 150, Xw, 750, pl.GetLogMin(gra3), pl.GetLogMax(gra3), CSng(ds), CSng(de)
For i& = 1 To NI
  dp(i) = pl.GetDepth(di(i))
Next
pl.DrawFlatLines pl.GetLogMin(gra3), pl.GetLogMax(gra3), dp(), NI, QBColor(10), 1
pl.DrawBlockGraph GRave(), dp(), NI, QBColor(12), 1 'Block Graph at Depth 3200 shoot out as it have been averaged on original
GR while the scale used is of GRave201x3
pl.DrawTrackFrame picMain, Xo, 150, Xw, 750, 1
pl.DrawTrackFrame picMain, Xo, 150, Xw, 750, 1


'----Selected Spike
Xo% = Xo + Xw
Xw# = 110
pl.DrawHeader picMain, Xo, 10, Xw, 130, 20, "GR_Ave201x3", QBColor(9), 3, 0, , , 2.6
pl.DrawLog picMain, Xo, 150, Xw, 750, "GR_Ave201x3", ss, es, QBColor(9), 1, 0
pl.DrawHeader picMain, Xo, 10, Xw, 130, 80, "SPK_MFlt", QBColor(12), 3, 0, , , 2.6
pl.DrawLog picMain, Xo, 150, Xw, 750, "SPK_MFlt", ss, es, QBColor(12), 1, 0
pl.DrawTrackFrame picMain, Xo, 150, Xw, 750, 1
```

ANNEXURE B

```
picMain.Cls

picMain.CurrentX = 15

picMain.CurrentY = 50

picMain.Print "Depth"

picMain.CurrentX = 15

picMain.CurrentY = 70

picMain.Print "(Meters)"


DoEvents

pl.ReadLAS App.Path & "\Kadanwari-19.las"

ds# = pl.GetDepthStart()

de# = pl.GetDepthStop()


ss& = pl.GetSampleIndex(ds)

es& = pl.GetSampleIndex(de)

es& = pl.GetSampleIndex(3400) 'Forced Depth End

de# = pl.GetDepth(es) 'Forced Depth End


Xo% = 80

Xw# = 150

pl.DrawDepthScale picMain, 10, 150, 60, 750, ds, de, 50, 200, QBColor(7), QBColor(8), QBColor(0)

pl.DrawDepthGrid picMain, Xo, 150, 845, 750, ds, de, 50, 200


gri% = pl.GetLogIndex("GR_EDTC")

pl.PutLogUnit gri, "API"


'--------------------Ave 201x3

pl.AllocateLogMemory "GRave1"

pl.AllocateLogMemory "GRave2"

gra1% = pl.GetLogIndex("GRave1")
```

```
pl.PutLogMin gra1, pl.GetLogMin(gri)
pl.PutLogMax gra1, pl.GetLogMax(gri)
pl.PutLogMin gra2, pl.GetLogMin(gri)
pl.PutLogMax gra3, pl.GetLogMax(gri)
pl.MovingAverage gra2, gra3, ss, es, 201

pl.DrawHeader picMain, Xo, 10, Xw, 130, 20, "GR_EDTC", QBColor(9), 3, 0
pl.DrawLog picMain, Xo, 150, Xw, 750, "GR_Ave201x3", ss, es, QBColor(12), 1, 0
pl.DrawTrackFrame picMain, Xo, 150, Xw, 750, 1
DoEvents

'--------------------Slope Computation
'----1st Derivative
Xo% = Xo + Xw
Xw# = 135
pl.DrawHeader picMain, Xo, 10, Xw, 130, 20, "GR_Ave201x3", QBColor(12), 3, 0
pl.DrawLog picMain, Xo, 150, Xw, 750, "GR_Ave201x3", ss, es, QBColor(12), 1, 0

pl.AllocateLogMemory "DRV1"
drv1% = pl.GetLogIndex("DRV1")
pl.Slope gra3, drv1, ss, es
pl.LogsMinMax
pl.DrawHeader picMain, Xo, 10, Xw, 130, 50, "DRV1", QBColor(3), 3, 0
750, 1
xs! = pl.GetLogMin(drv1)
xe! = pl.GetLogMax(drv1)

'----1st Derivative-Minimum Filter
drv1m% = pl.GetLogIndex("DRV1_MFlt")
pl.FilterMinimum drv1, drv1m, ss, es, xs * 0.12, xe * 0.12
pl.PutLogMin drv1m, xs
pl.PutLogMax drv1m, xe
```

```
'----1st Derivative-Minimum Filter-Spike
pl.PutLogMax spk1m, xe

Xo% = Xo + Xw
Xw# = 140
pl.DrawLog picMain, Xo, 150, Xw, 750, "SPK_MFlt", ss, es, QBColor(3), 1, 0
pl.DrawLog picMain, Xo, 150, Xw, 750, "DRV1_MFlt", ss, es, QBColor(13), 1, 0
pl.DrawTrackFrame picMain, Xo, 150, Xw, 750, 1

'----Selected Spike
Xo% = Xo + Xw
Xw# = 140
pl.DrawLog picMain, Xo, 150, Xw, 750, "GR_Ave201x3", ss, es, QBColor(9), 1, 0
pl.DrawHeader picMain, Xo, 10, Xw, 130, 80, "SPK_MFlt", QBColor(12), 3, 0
pl.DrawLog picMain, Xo, 150, Xw, 750, "SPK_MFlt", ss, es, QBColor(12), 1, 0
pl.DrawTrackFrame picMain, Xo, 150, Xw, 750, 1

'----Depth Intervals
Dim di&(), NI&
pl.DepthIntervals spk1m, ss, es, di(), NI&
Xo% = Xo + Xw
Xw# = 140
pl.DrawHeader picMain, Xo, 10, Xw, 130, 20, "GR_Ave201x3", QBColor(9), 3, 0
pl.DrawLog picMain, Xo, 150, Xw, 750, "GR_Ave201x3", ss, es, QBColor(9), 1, 0

'----Block Average GR
pl.MaxClipFilter gri, ss, es, 220
pl.PutLogMax gri, 220

ReDim GRave!(NI), dp!(NI)
pl.BlockAverage gri, di(), NI, GRave()
```

```
pl.DrawFreeHeader picMain, Xo, 10, Xw, 130, 50, "GR_BlkAve", "API", pl.GetLogMin(gra3), pl.GetLogMax(gra3), QBColor(12), 3

pl.SetGraphicsContext picMain, Xo, 150, Xw, 750, pl.GetLogMin(gra3), pl.GetLogMax(gra3), CSng(ds), CSng(de)

For i& = 1 To NI

  dp(i) = pl.GetDepth(di(i))

Next

pl.DrawFlatLines pl.GetLogMin(gra3), pl.GetLogMax(gra3), dp(), NI, QBColor(10), 1

pl.DrawBlockGraph GRave(), dp(), NI, QBColor(12), 1 'Block Graph at Depth 3200 shoot out as it have been averaged on original GR while the scale used is of GRave201x3

pl.DrawTrackFrame picMain, Xo, 150, Xw, 750, 1

pl.SetGR100 pl.GetLogMax(gri)

pl.GammaRayIndex gri, Vs, ss, es

pl.LogMinMax "Vsh", ss, es


Xo% = Xo + Xw

Xw# = 140

pl.DrawHeader picMain, Xo, 10, Xw, 130, 20, "Vsh", QBColor(12), 3, 0, , 2

pl.DrawLog picMain, Xo, 150, Xw, 750, "Vsh", ss, es, QBColor(12), 1, 0

ReDim VSave!(NI)

pl.BlockAverage Vs, di(), NI, VSave()

pl.DrawFreeHeader picMain, Xo, 10, Xw, 130, 50, "Vsh_BlkAve", "%", pl.GetLogMin(Vs), pl.GetLogMax(Vs), QBColor(14), 3, , , 2

pl.SetGraphicsContext picMain, Xo, 150, Xw, 750, pl.GetLogMin(Vs), pl.GetLogMax(Vs), CSng(ds), CSng(de)

pl.DrawBlockGraph VSave(), dp(), NI, QBColor(14), 1

pl.DrawTrackFrame picMain, Xo, 150, Xw, 750, 1


Xo% = Xo + Xw

Xw# = 140

pl.ReadColorSpectrum "C:\K-tron\Templates\ColorSpectrum\KCS\BlueRed.kcs"

'pl.ReadColorSpectrum "C:\K-tron\Templates\ColorSpectrum\KCS\Color-V-CLR.kcs"

 (Vs), VSave(), dp(), NI

pl.DrawBlockGraph VSave(), dp(), NI, QBColor(14), 1

pl.DrawTrackFrame picMain, Xo, 150, Xw, 750, 1
```